

**Estimation of regional evaporation under different
weather conditions from satellite and
meteorological data:**

A case study in the Naivasha Basin, Kenya

Promotor:

Prof. dr. ir. R.A. Feddes
Professor in Soil Physics, Agrohydrology
and Groundwater Management
Wageningen University, Wageningen

Co-promotor:

Prof. dr. W.G.M. Bastiaanssen
Visiting Professor in Applications of
Remote Sensing in Water
Resources Management
International Institute for Aerospace
Surveys and Earth Sciences (ITC),
Enschede

Members examination committee:

Prof. dr. B. Holtslag (Wageningen
University)
Prof. dr. H. Savenije (Delft University of
Technology and IHE)
Prof. dr. M. Menenti (University de
Strasbourg, France)
dr. A.S.M. Gieske (ITC, Enschede)

NN08201,2927

Estimation of regional evaporation under different weather conditions from satellite and meteorological data:

A case study in the Naivasha Basin, Kenya

Hussein O. Farah

Thesis

To fulfil the requirements for the degree of doctor
on the authority of the rector magnificus
of Wageningen University,
Prof. dr. ir. L. Speelman,
to be publicly defended on Friday 19th January 2001
at three O'clock in the auditorium of ITC, Enschede

im 1603649

ITC Dissertation number 80

The research presented in this thesis was partly conducted at the International Institute for Aerospace Survey and Earth Sciences (ITC), P.O. Box 6, 7500 AA Enschede,
The Netherlands.

CIP-DATA KONINKLIJKE BIBLOTHEEK, DEN HAAG

© 2001 Hussein O. Farah



Printed by FEBODRUK BV, Enschede
Cover design by Taib El Ghazi

Estimation of regional evaporation under different weather conditions from satellite and meteorological data: A case study of the Naivasha basin.

Doctoral Thesis Wageningen University and ITC. - With ref. - With summary in Dutch

ISBN 90-5808-331-4

Abstract

Farah, H.O., 2000. *Estimation of regional evaporation under different weather conditions from satellite and standard weather data: A case study of the Naivasha Basin, Kenya*. Ph.D. thesis, Wageningen University, The Netherlands

The operational use of optical and thermal remote sensing methods for the monitoring of evaporation has been limited because of existing cloud cover problems as well as the need for field data by the remote sensing algorithms. The focus of this thesis is the development of methods to map the spatial patterns and temporal evolution of evaporation on both clear and cloudy days. The Naivasha basin in Kenya is used as a case study.

Existing remote sensing algorithms used to estimate evaporation from remotely sensed data differ in the way they describe the spatial variations of input parameters. An evaluation of the impact of spatially varying input parameters on distributed surface fluxes showed that the vertical near surface air temperature difference and frictional velocity were the most critical parameters. Most remote sensing algorithms treat air temperature as spatially constant indicating that they are less suitable for the calculation of distributed evaporation in heterogeneous catchments.

The temporal variability of the evaporative fraction Λ (Eq. 5.1) at the daily and seasonal time frames was investigated with field data obtained at two experimental sites. For general weather conditions the values of the midday (12.00 to 13.00 hrs) evaporative fraction Λ_{mid} compared well with the averaged day time evaporative fraction Λ_{day} . A good relationship was obtained between daytime evaporation estimated from Λ_{mid} and evaporation measured by the Bowen ratio surface energy balance method. Less satisfactory evaporation results were obtained using morning (9.00 to 10.00 hrs) evaporation fraction Λ_{mor} . The seasonal evolution of Λ_{day} was observed to be gradual. To capture the seasonal evolution of Λ_{day} it would be sufficient to measure Λ_{day} approximately every 10 days. Moreover, it was shown that the inter-annual variability of the 10-day average Λ could be reliably estimated from standard weather data.

To monitor the temporal evolution of daily evaporation over a season, evaporation has to be estimated between consecutive clear days with satellite images being available. Two methods to predict daily evaporation on days without satellite images due to cloud cover are presented. Field data acquired at two sites were used to test these methods. The first method consists of the application of the Penman-Monteith equation and Jarvis-Stewart model with standard weather data and the assumption of gradual soil moisture changes between consecutive clear days. With this method evaporation could be accurately predicted for up-to 5 continuous days with no satellite images. The second method is a simplified approach involving the use of a constant Λ between cloud free days with measured evaporation. This approach did not give satisfactory results in predicting evaporation on individual days. However, the total evaporation of a 7-day time span was equally good for both methods.

Five NOAA AVHRR satellite images were used to produce daily evaporation maps of the Naivasha basin for 15 continuous days with intermittent cloud cover by using the Penman-Monteith equation coupled with the Jarvis-Stewart model as well as the evaporative fraction method. The evaporation maps were validated with field data and overall good agreement was obtained. This demonstrated that remote sensing methods can be extended for practical use under all weather conditions to map both the spatial patterns as well as the temporal evolution of evaporation in catchments and river basins. The methods of predicting evaporation can be applied at different time scales. Users can select the appropriate time scales depending on their needs. The implementation of the Penman-Monteith equation and Jarvis-Stewart model requires a land cover classification of the catchment to assign land cover dependent coefficients in the Jarvis-Stewart model. At each land cover type standard weather data has to be measured.

Key words: evaporation, evaporative fraction, thermal infrared remote sensing, spatio-temporal variations of evaporation, Naivasha basin, Kenya

PROPOSITIONS

1. The application of the hypothesis of quasi-constant evaporative fraction to estimate daily evaporation is valid under general weather conditions provided evaporative fraction from the central hours of the day is used. *(This thesis)*
2. Satellite overpass times in the early morning or late afternoon may be useful for visual interpretation of surface features but not for evaporation estimation. Measurements from Landsat and Terra satellites have therefore to be treated carefully. *(This thesis)*
3. The combination of Surface Energy Balance Algorithm for Land (SEBAL) with the Penman-Monteith and Jarvis-Stewart models can be used to temporally integrate regional evaporation under different weather conditions. *(This thesis)*
4. Remote sensing evaporation algorithms that do not account for the spatial variability of near-surface temperature gradients and surface roughness length for heat transport will give erroneous distributed evaporation values in a heterogeneous area. *(This thesis)*
5. In developing countries, the development of tools to improve water resources management is frequently hampered by lack of information on meteorology, hydrology, soil and land use. *(This thesis; Decurtins, S. 1992. Hydrogeographical investigations into Mount Kenya subcatchments of Ewaso-Ngiro river. African Studies Series No. A10. University of Bern, Switzerland)*
6. Remote sensing applications have focussed too much on land use mapping and little on its water use surveying capabilities. Satellite information on evaporation and biological production can provide rapid appraisal and reliable assessment of water accounts and return on investment. *(Molden, D.J. 1997. Accounting for water use and productivity, SWIM Paper 1. International Water Management Institute, Colombo, Sri Lanka)*
7. Look for Knowledge even if it is as far as China. *(Arabic saying)*
8. Smooth seas do not make a skilful sailor. *(Ethiopian Proverb)*

9. War on nations change maps. War on poverty maps change. (*Muhammad Ali*)
10. It is clear that most children suffer too much mother and too little father. (*Gloria Steinem*)

H.O.Farah

Estimation of regional evaporation under different weather conditions from satellite and meteorological data: A case study in the Naivasha Basin, Kenya.

Ph.D. Thesis Wageningen University (19 January 2001)

Acknowledgements

The work related to this thesis was made possible with the support of many people and institutions to whom I would like to express my gratitude.

I thank Prof. A.M.J. Meijerink for inviting me to the division of Water Resource and Environmental Studies at ITC to undertake my research work. I am grateful for his support and interest in my work.

I am greatly indebted to Prof. W.M.G. Bastiaanssen for his guidance and encouragement throughout my study period. I appreciate his constructive criticisms, advice and all that he has taught me. I also acknowledge his assistance in the field, during the data collection stages of my research and translating Chapter 8 into Dutch.

I would like to thank very much my Promotor, Prof. R.A. Feddes for his guidance and support. I greatly appreciate his critical reading and comments of the different chapters in this thesis. I thank him for imparting to me the invaluable skills of scientific and technical writing.

I gratefully acknowledge the financial support I received from the MHO-Water Resources Engineering cooperation project between Delft University of Technology and Moi University. Special thanks go to Prof. S.M. Shitote, the entire staff of the Department of Civil Engineering, Moi University and Dr. J. van Dijk of CICAT, Delft University of Technology for making all administrative and logistic work both in Kenya and in the Netherlands possible. I also thank Moi University for granting me study leave to enable me pursue this research.

Many thanks go to the staff in the division of Water Resources and Environmental Studies at ITC for the great assistance I received from them. Of special mention are Dr. M.W. Lubczynski, Ir. W.J. Timmermans and Drs. R. Becht for their assistance in the programming and setting up of field instruments. Dr. A.S.M. Gieske and Ir. G.N. Parodi for making available to me remote sensing softwares used in this study. G.J. Polman and J.A. Mulder for always being ready and quick to fix the many computers glitches I encountered. R. Hummel, T.B. Boogaard, J. Walet and H. Al-Malih of the secretarial section for splendid help in administrative matters.

I am indebted to Dr. E. Kusters, the ITC research coordinator and Loes Collenbrander of the Ph.D. helpdesk for their support in coordinating all financial and administrative matters related to my work at ITC. During my stay in the Netherlands, I received considerable support and friendship from my colleagues Mohamed Said, Wilson Khaemba, Dan Arwa, Musyimi Mbathi, Dan Kithinji,

Patrick Ogao, Patrick Kariuki, Julius Nbambuki, Jothanan Ngetich, Boniface Oluoch, Mohamud Bakr and Mobin-udin-Ahmed.

I wish to express my gratitude to my parents, brothers and sisters for their continuous moral support and encouragement during my endeavor to complete this work. Finally, I thank my wife and children for their patience and perseverance during long periods of our separation.

Contents

	Page
Abstract	v
Acknowledgements	vii
List of symbols	xi
1. Introduction	1
1.1 General background	1
1.2 Problem identification	1
1.3 Objectives	7
1.4 Outline of thesis	7
2. Theory and parameterization of evaporation	9
2.1 Soil water balance	9
2.2 Surface radiation and energy balance	10
2.3 Transport processes of water vapour, heat and momentum	11
2.4 Combination equation for evaporation	15
2.5 Remote sensing evaporation algorithms	22
3. Description of the study area	29
3.1 Geographical setting	29
3.2 Field experiments	33
4. The impact of spatial variations of surface parameters on regional evaporation: A case study with remote sensing data	39
4.1 Introduction	39
4.2 Estimation of basic surface radiometric parameters	43
4.3 Hydrological delineation of Kenyan central rift valley	45
4.4 Estimation of SVAT parameters and surface fluxes	49
4.5 Validation of surface fluxes	57
4.6 Aggregation of SVAT parameters and fluxes	63
4.7 Surface parameters variability and impact on surface fluxes	65
4.8 Conclusions	69
5. Evaluation of the temporal variability of the evaporative fraction in a tropical watershed	71
5.1 Introduction	71
5.2 Theoretical background	73
5.3 Seasonal variations of actual evaporation	78
5.4 Diurnal stability of evaporative fraction	81
5.5 Comparison of midday evaporative fraction and average day time evaporative fraction	84
5.6 Seasonal variations of evaporative fraction	85
5.7 Conclusions	90

6. Derivation of daily evaporation under all weather conditions from standard meteorological data and clear sky flux information	91
6.1 Introduction	91
6.2 Materials and methods	93
6.3 Results and discussion	98
6.4 Conclusions	111
7. Evaluation of the temporal evolution of daily evaporation with NOAA AVHRR and ground data in the Naivasha basin	113
7.1 Introduction	113
7.2 Material and Methods	114
7.3 Results and discussion	117
7.4 Conclusions	131
8. Summary and conclusions	133
Samenvatting en conclusies	139
References	145
Apendix A	157
Appendix B	159
Curriculum vitae	165
List of ITC Ph.D. dissertations	167

List of symbols

SYMBOL	DESCRIPTION	DIMENSION	SI UNIT
A	Total area	L^2	m^2
A	Sub area	L^2	m^2
c	Entity	variable	variable
c_p	Air specific heat	$L^2T^{-2}\Theta^{-1}$	$J\ kg^{-1}\ K^{-1}$
c_s	Soil specific heat capacity	$L^2T^{-2}\Theta^{-1}$	$J\ kg^{-1}\ K^{-1}$
d	Zero-plane displacement	L	m
e	Vapour pressure	$L^{-1}MT^{-2}$	Pa
e^*	Saturated vapour pressure	$L^{-1}MT^{-2}$	Pa
E	Actual evaporation rate; mass basis volume basis	$L^{-2}MT^{-1}$ LT^{-1}	$kg\ m^{-2}\ s^{-1}$ $m^3\ m^{-2}\ s^{-1}$
G_0	Soil heat flux density	MT^{-3}	$W\ m^{-2}$
g	Acceleration due to gravity	LT^{-2}	$m\ s^{-2}$
H	Sensible heat flux density	MT^{-3}	$W\ m^{-2}$
I_r	Irrigation input rate	LT^{-1}	$m\ s^{-1}$
$K\downarrow$	Incoming shortwave radiation	MT^{-3}	$W\ m^{-2}$
K_h	Diffusion coefficient for heat	L^2T^{-1}	$m^2\ s^{-1}$
K_m	Diffusion coefficient for momentum	L^2T^{-1}	$m^2\ s^{-1}$
K_v	Diffusion coefficient for vapour	L^2T^{-1}	$m^2\ s^{-1}$
k	Von Karman's constant	-	-
L	Monin-Obukhov length	L	m

SYMBOL	DESCRIPTION	DIMENSION	SI UNIT
<i>LAI</i>	Leaf area index	-	-
<i>NDVI</i>	Normalized difference vegetation index	-	-
<i>P</i>	Precipitation rate	LT^{-1}	$m\ s^{-1}$
<i>Q</i>	Net subsurface flow rate	LT^{-1}	$m\ s^{-1}$
<i>q</i>	Air specific humidity	-	-
<i>R</i>	Lateral surface runoff rate	LT^{-1}	$m\ s^{-1}$
<i>r_p</i>	Planetary reflectance	-	-
<i>r₀</i>	Surface reflectance	-	-
<i>r_{ah}</i>	Aerodynamic resistance to momentum transport	$L^{-1}T$	$s\ m^{-1}$
<i>r_{av}</i>	Aerodynamic resistance to vapour transport	$L^{-1}T$	$s\ m^{-1}$
<i>r_c</i>	Canopy resistance	$L^{-1}T$	$s\ m^{-1}$
<i>r_s</i>	Bulk surface resistance	$L^{-1}T$	$s\ m^{-1}$
<i>r_{sh}</i>	Soil resistance to heat transport	$L^{-1}T$	$s\ m^{-1}$
<i>r_{sl}</i>	Soil resistance to water liquid transport	$L^{-1}T$	$s\ m^{-1}$
<i>r_{sv}</i>	Soil resistance to water vapour transport	$L^{-1}T$	$s\ m^{-1}$
<i>RH</i>	Relative humidity	-	-
<i>R_n</i>	Net radiation flux density	MT^{-3}	$W\ m^{-2}$
<i>s</i>	Slope of saturation vapour pressure curve	$L^{-1}MT^{-2}\Theta^{-1}$	$Pa\ K^{-1}$
<i>t</i>	Time	T	s
<i>T_a</i>	Air temperature	Θ	K

SYMBOL	DESCRIPTION	DIMENSION	SI UNIT
T_s	Soil temperature	Θ	K
T_o	Surface temperature	Θ	K
T_p	Potential temperature	Θ	K
T_{sh}	Heat source temperature	Θ	K
u	Wind velocity	LT^{-1}	$m\ s^{-1}$
u_*	Frictional velocity	LT^{-1}	$m\ s^{-1}$
W	Soil water storage	L	m
z	Height	L	m
z_B	Blending height	L	m
z_{oh}	Aerodynamic roughness length for heat transport	L	m
z_{om}	Aerodynamic roughness length for momentum	L	m
β	Bowen ratio ($H/\lambda E$)	-	-
γ	Psychrometric coefficient	$L^{-1}MT^{-2}\Theta^{-1}$	$Pa\ K^{-1}$
ϵ_0	Surface emissivity	-	-
ϵ'	Atmospheric emissivity	-	-
λE	Latent heat flux density	MT^{-3}	$W\ m^{-2}$
ΔT_a	Vertical air temperature difference	Θ	K
ρ_a	Air density	$L^{-3}M$	$kg\ m^{-3}$
τ	Momentum flux density	$L^{-1}MT^{-2}$	$N\ m^{-2}$
τ_{sw}	Shortwave transmittance	-	-
τ_{sw}''	Two way shortwave transmittance	-	-

SYMBOL	DESCRIPTION	DIMENSION	SI UNIT
h	Soil water pressure head	L	m
ψ_h	Stability correction for heat transport	-	-
ψ_m	Stability correction for momentum transport	-	-
ψ_v	Stability correction for vapour transport	-	-
ϕ_h	Monin Obukhov function for heat transport	-	-
ϕ_m	Monin Obukhov function for momentum transport	-	-
ϕ_v	Monin Obukhov function for vapour transport	-	-
Λ	Evaporative fraction ($\lambda E/(\lambda E + H)$)- Eq.5.1	-	-
θ	Volumetric soil water content	-	$\text{m}^3 \text{ m}^{-3}$

Chapter 1

Introduction

1.1 General background

Kenya is among those countries, that will face economic water scarcity in the next 20 years (Cosgrove and Rijsberman, 2000). With a population growth estimated at an annual rate of 3%, increasing pressure is being exerted on the available land and water resources (Kohler, 1987). Scarcity of water is already being experienced as hereto perennial rivers have now ceased to flow during certain periods of the year due to water diversions in the upper catchments of these rivers (Decurtins, 1992). The focus today is to conserve and better manage the available water resources in a rational and efficient manner. Evaporation E is the loss of water in the form of vapour from the earth's surface to the atmosphere. Evaporation consumes about 60% of precipitation when averaged over all continents (Brutsaert, 1982). In tropical regions, up to 90% of water flowing through a river basin may be used in the E process (Jensen, 1990). Knowledge of the spatio-temporal variations of E is therefore important for the planning and management of water resources.

1.2 Problem identification

Evaporation varies spatially owing to the heterogeneous nature of vegetation cover, soil properties and differences in water availability caused by hydrological processes. In heterogeneous catchments, there is a stratum of surfaces such as bare soils, water bodies and vegetation to which different E rates apply. In hydrological studies, the quantities of water evaporated at the macro-scale such as field, catchment or river basin are of interest. The evaporation from each element at micro scale in the landscape has to be aggregated to the macro-scale in order obtain the required macro scale estimate of E_A at time t . This may be achieved by spatially integrating the micro-scale $E(a_i)$ at time t :

$$E_A(t) = \frac{1}{A} \int_{i=1}^{i=n} E(a_i, t) da \quad (1.1)$$

where $E(a_i, t)$ is the micro-scale evaporation for element i and A is the size of the whole study area. Evaporation also displays large diurnal and seasonal variations. These variations are due to the changes in the amount of precipitation and radiant energy at the surface caused by changes in the solar elevation. Temporally the fluxes may be described in time frames ranging from minutes to years. The determination of the accumulated E at the micro as well as the macro-scale requires the temporal integration of $E(a_i, t)$ and $E_A(t)$

$$E_{ait} = \int_0^t E(a_i, t) dt \quad (1.2)$$

$$E_{At} = \int_0^t E_A(t) dt \quad (1.3)$$

where t is the duration of time for which E is to be determined.

Determining of $E(a_i, t)$ in a heterogeneous landscape is a difficult task. Conventional measurement techniques of E give point values. It is not possible to have an adequate number of point measurements in order to capture all the spatial variations in the landscape and obtain reliable estimates of E_A . This is because of the practical limitations of the economic resources and expert manpower required to implement such a measurement network. Pelgrum and Bastiaanssen (1996) have demonstrated that $E(a_i)$ from 21 different field stations is far from sufficient to predict E_A in a 5000 km² study area.

Satellite remote sensing is a powerful tool to provide measurements at a wide range of spatial scales ranging from an individual pixel to an entire raster image that may cover a whole river basin. Estimation of $E(a_i, t)$ has been investigated since the operation of earth resource satellites in the 1970s. Many remote sensing based E estimation techniques have been developed since then (e.g. Jackson et al., 1977; Moran and Jackson, 1991). In the context of regional hydrology, Sellers et al., (1995) and Kustas et al., (1994) investigated methods to determine E_{At} . Whereas remote sensing techniques have assisted in the solution of Eq.1.1, little attention has been given to the determination of Eq. 1.3 by remote sensing methods. This limits the operational application of these methods considerably.

Fig. 1.1 illustrates schematically the problem of determining E_{at} and E_{Af} . A remote sensing algorithm uses spatially *distributed* input variables $p_i(x,y)$ from satellite data on clear days and spatially *constant* input variables p_{ic} from field data to calculate evaporation. On cloudy days optical satellite data are of no use and one has to rely on field data. As illustrated in Fig. 1.1, the practical use of remote sensing to solve Eq. 1.3 in heterogeneous landscapes is thus hampered by two major limitations:

- cloud cover
- lack of spatially variable field data

In many parts of the world, cloud cover is a prominent phenomenon. In the humid tropics, mean cloud cover per day may exceed 60% (Bussieres and Goita, 1997). Fig.1.2 shows the average monthly cloud cover for a grassland area in the Naivasha basin in Kenya. It can be seen that during 9 months of the year cloud cover is more than 40%. Only satellite data with less than 20% cloud cover of the area of interest are considered usable for E studies (Petehercych et al., 1983). The chances of getting cloud free conditions are therefore limited.

Although microwave remote sensing data could be used to overcome this problem, apart from the difficulties encountered in their algorithm formulation, their temporal frequencies are not suitable for E determination. Moreover, there is a cost issue. Radar images are very expensive to use on an operational basis.

Because of cloud cover problems the use of remote sensing methods has been restricted to short time frames such as a few days. To monitor E over a season an extension of the remote sensing methods is required. Between two consecutive cloud-free days when satellite imagery is available, E has then to be estimated by other means. Little work exists in the literature on methods of dealing with this problem and obtain a solution for Eq. 1.3.

The Penman-Monteith equation is the most widely tested physically based model to predict evaporation under different climatic conditions and has been shown to be suitable for the calculation of actual E (Parlange, 1995; Choudhury, 1997a), reference E (Allen et al., 1998) and potential E (Choudhury, 1997b). The application of the Penman-Monteith model is usually hindered by the difficulty of

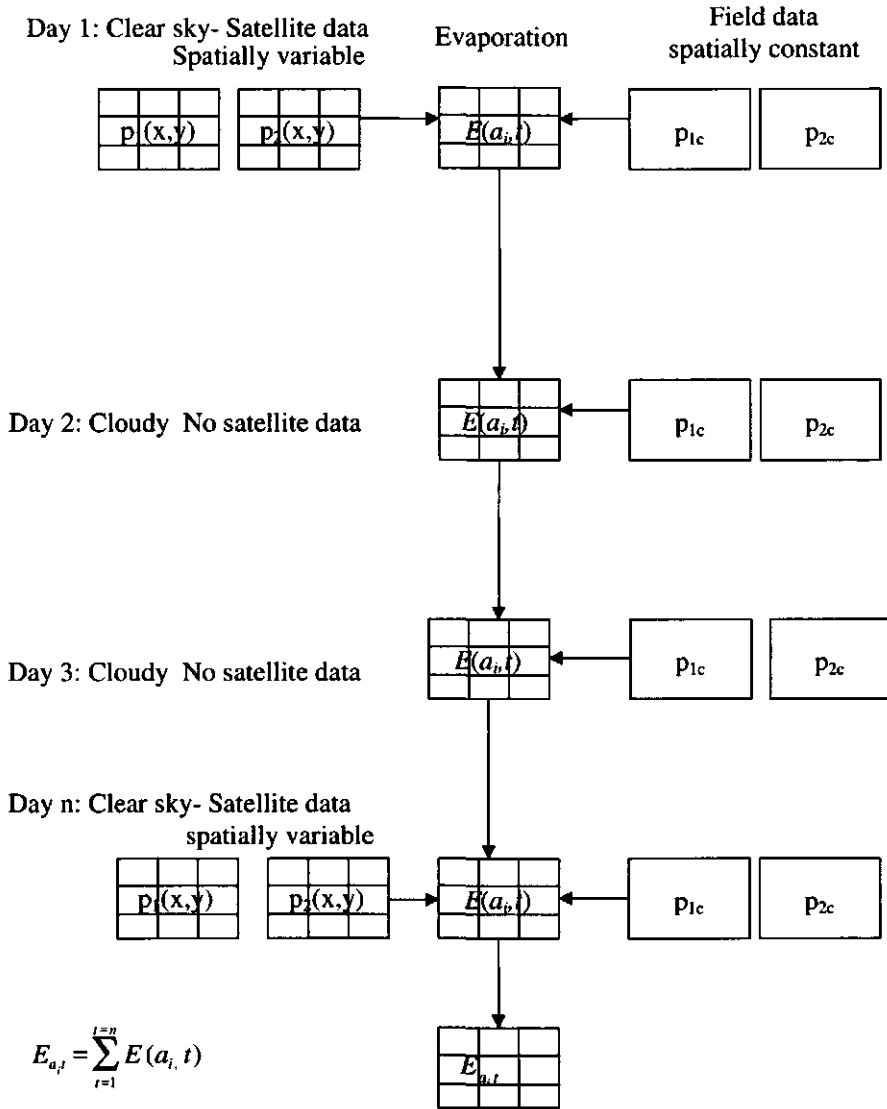


Fig.1.1. Schematic illustration of the problems encountered in determining the time integration of spatially distributed evaporation, with satellite data being available on clear days only.

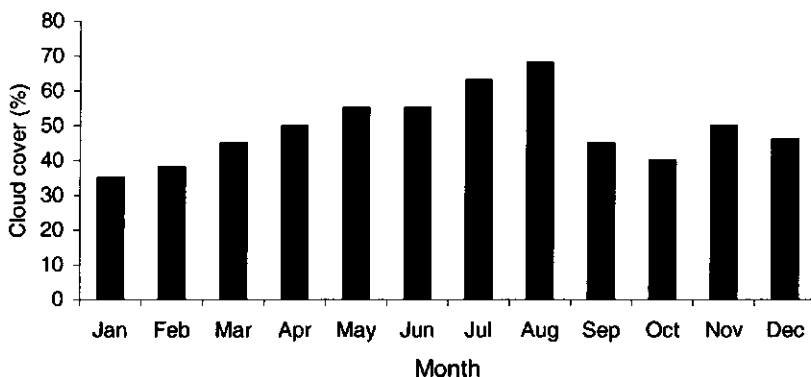


Fig.1.2 Average monthly cloud cover for the period 1961-1968 at the Kedong meteorological station (0°55' S 36°30' E) in the Naivasha basin, Kenya

estimating surface resistance r_s and boundary layer resistance r_{ah} to vapour transport. Surface resistance of partially vegetated surfaces consists of the sum of individual leaf resistances and the resistance to soil evaporation. The description of r_s involves interaction between the physiology of leaves and the environment (Tan and Black, 1976; Shuttleworth and Wallace, 1985). The most common approach to model the effect of r_s on environmental factors is the so-called Jarvis-Stewart type models (Jarvis, 1976; Stewart, 1988). In the present study the potential of linking the Penman-Monteith equation to remote sensing information in order to obtain continuous E data over a season will be investigated.

Even when cloud free images are acquired during clear moments of the day, cloud covers during other parts of the day can affect the accuracy of the estimated daily totals of E . Remote sensing measurements are instantaneous measurements and it is necessary to convert these measurements to daily totals. A number of methods are available for extrapolating the instantaneous values into daily totals. The most widely used technique is based on the similarity of the diurnal courses of E and one of the other terms of the energy balance, such as sensible heat flux (Bastiaanssen et al., 1996), available energy at the surface (Shuttleworth et al., 1989) and solar radiation (Jackson et al., 1983). Zhang and Lemeur (1996) evaluated these techniques and concluded that under clear sky conditions daily E can be estimated accurately from instantaneous values. These authors cautioned however, the use of these techniques under cloudy conditions because the assumptions underlying the

integration methods may not be satisfied under cloudy conditions. An investigation is required on the suitability of the diurnal temporal integration methods for the weather conditions prevailing in the tropics.

To estimate spatially distributed E (see Fig. 1.1) remote sensing algorithms use both spatially variable and spatially constant input variables. Table 1.1 presents the type of field data typically used in remote sensing based E algorithms. Apart from routine weather data, information on vegetation and soil physical properties is needed by some of these algorithms. Because of the absence of complete datasets, the field data are usually obtained from a few points and assumed to be spatially constant across the area of study. The required spatial variability of the input variables needed to obtain reliable E results is therefore often ignored. The consequence of handling the spatial variability of input variables by remote sensing algorithms on surface fluxes has received little attention in the literature.

Table 1.1: Required field information for some selected remote sensing evaporation algorithms

Algorithm	Plant height properties	Wind speed	Air temperature	Air humidity	Solar radiation	Soil
1	✓		✓	✓		
2		✓	✓	✓	✓	✓
3			✓	✓	✓	
4	✓		✓	✓	✓	
5		✓	✓	✓		
6	✓		✓	✓		
7	✓	✓	✓	✓	✓	✓
8	✓		✓	✓		

1. Nieuwenhuis et al., 1985 2. Taconet et al., 1986 3. Abdellaoui et al., 1986 4. Hall et al., 1992 5. Hurdato et al., 1994 6. Kustas et al., 1994 7. Hatfield et al., 1984 8. Granger, 1997

1.3 Objectives

The focus of this research is the monitoring of regional evaporation in the Naivasha basin in Kenya by using remote sensing techniques. The specific objectives are as follows:

1. Investigate the limitations of the handling of spatial variability of input variables in remote sensing algorithms and their impact on the estimation of surface fluxes
2. Investigate methods to temporally integrate the evaporate rate for intermittent cloud conditions found in Kenya
3. Develop an operational method to monitor micro and macro-scale evaporation by remote sensing over a season

1.4 Outline of thesis

The theoretical basis of the E process and the parameterization of remote sensing algorithms are discussed in Chapter 2. First, the water balance approach is presented. Next the energy balance and the aerodynamic transport processes governing water vapour, heat and momentum fluxes are discussed. It is explained how the complex E process equations can be conceptualized in simple resistance schemes and how the Penman-Monteith equation is derived from that. A brief overview of remote sensing flux algorithms is given and some of their limitations are highlighted.

In Chapter 3 the physical setting of the Naivasha basin and the fieldwork performed at two experimental sites are presented. The location, topography and climatic conditions of the basin are described. Details of the micro-meteorological measurements and the Bowen ratio towers set up at two sites are given. These data sets are used in the validation of E calculation procedures developed in the subsequent chapters.

Chapter 4 addresses the importance of considering the spatial variability of input parameters in remote sensing algorithms on the estimation of surface fluxes. The delineation of the study area into 15 homogenous units using Landsat TM derived

surface temperature, surface albedo and *NDVI*, is described. Surface fluxes are estimated for each of the 15 units. The input parameters are aggregated and the impact of using aggregated parameters on calculated distributed surface fluxes is analyzed. The parameters are identified that should be described in spatial detail in order to obtain reliable *E* estimates.

In Chapter 5 the validity of methods to temporally integrate instantaneous fluxes to daily values is tested with field data from the two experimental sites described in Chapter 3. The diurnal stability of the evaporation fraction (Eq. 5.1) is analyzed and related to the variations in air temperature, humidity and the atmospheric transmission of solar radiation. An analysis of the performance of the evaporation fraction, obtained at midday and midmorning, to temporally integrate *E* to daily values is carried out. The implications of the gradual changes in the average daily evaporation fraction, for the estimation of 10-day average and longer *E* estimates are discussed.

The question of scarcity of cloud free images is addressed in Chapter 6. A framework consisting of the use of the Penman-Monteith and Jarvis-Stewart models is proposed for predicting *E* during periods of cloudy conditions. The result of the method is tested with field data. A simpler method to predict *E*, by assuming a constant evaporation fraction over several days, is also used and tested.

Chapter 7 deals with the applications of the methods developed in Chapters 4, 5 and 6 in a practical remote sensing *E* monitoring approach of the Naivasha basin. An operational *E* monitoring procedure is presented. NOAA AVHRR satellite data in conjunction with the extrapolation methods developed are used to derive *E*. The results are compared with field data.

Finally, a summary and conclusions of the study are given in Chapter 8.

Chapter 2

Theory and parameterization of evaporation

2.1 Soil water balance

Evaporation E is the process by which water is evaporated from wet surfaces and transpired by plants. The rate of E depends on the availability of water and amount of energy at the evaporating surface and the ease with which water vapour can diffuse into the atmosphere. The ease of diffusion is controlled by the aerodynamic properties of the surface and by the moisture and turbulence conditions of the atmosphere. The process of E can be described by means of the soil water balance, the energy balance at the earth's surface, turbulent transport mechanisms and the moisture balance of the atmosphere (Menenti, 1993).

The soil water balance is based on the conservation of mass and accounts for the incoming and outgoing moisture fluxes of a soil layer. When soils are sufficiently moist to maintain maximum E rates, the radiation balance controls the E process. However, under conditions of persistent soil moisture deficit the sub-surface soil water transport controls the E process. The soil water balance processes in a flat terrain are mostly vertical moisture movements and may be described in one dimension. Change in water storage (m) of a soil column over a particular soil depth z and time interval t , is defined as:

$$\Delta W = - \int_0^t \int_0^z \frac{\partial \theta}{\partial t} dz dt \quad (2.1)$$

where θ is the volumetric soil water content ($m^3 m^{-3}$). The soil water balance relates E and the change in soil water storage ΔW . Defining the change in soil water storage ΔW as an "in- out" term, the soil water balance can be written as:

$$\Delta W = (P + I_r + Q - E - R)\Delta t \quad (2.2)$$

where P (m s^{-1}) is the precipitation rate, I_r (m s^{-1}) is the irrigation water input rate, Q (m s^{-1}) is the net subsurface flow rate, being positive upwards, and R (m s^{-1}) is the lateral runoff rate over the soil surface. According to the definition given in Eq. 2.1, ΔW and Q relate to a certain soil depth z . It is common practice in hydrology to obtain E as a residual term after determining first the other terms. The magnitude of the soil water balance terms depends on the hydrological and atmospheric conditions. The terms ΔW and Q are however difficult to measure reliably in natural catchments, especially over periods less than a month. Accurate area average estimates of precipitation are also difficult to determine because of the spatial variability of precipitation. The calculation of E as the water balance residual, results in substantial errors especially when E estimates on daily time scales are required. Hence other methods have to be resorted to. Evaporation is the common term between the water balance and the energy balance at the earth's surface. The energy balance may therefore be used in hydrological studies to determine E .

2.2 Surface radiation and energy balance

The surface energy balance is the main boundary condition to be satisfied in the estimation of E . The energy budget is defined for a unit horizontal area:

$$R_n = G_0 + H + \lambda E \quad (2.3)$$

where R_n (W m^{-2}) is the net incoming radiation flux density, H (W m^{-2}) is the sensible heat flux density, G_0 (W m^{-2}) is the ground heat flux density and λE (W m^{-2}) is the latent heat flux density. The parameter λ is the latent heat of vapourization of water (J kg^{-1}) and E is the vapour flux density ($\text{kg m}^{-2} \text{s}^{-1}$). Evaporation E can also be expressed in equivalent of water depth over a period of time. The energy stored in vegetation and the energy used in biochemical processes in plants are often negligible and usually ignored in hydrological studies. The main challenge in the energy balance is to determine the partitioning of the available energy ($R_n - G_0$) into λE and H . If the fraction of available energy used to evaporate water can be isolated from that used in heating the atmosphere, λE can be easily calculated from the available energy. This energy partitioning is classically established through the Bowen ratio β where the Bowen ratio is defined as $H/\lambda E$ (Bowen, 1932). The energy partitioning can also be achieved by means of the evaporative fraction A , defined as $A = \lambda E / (R_n - G_0)$ (Shuttleworth et al., 1989)

The net radiation R_n is the difference between all incoming and outgoing radiative fluxes. Radiation is divided into shortwave and longwave. The amount of incoming shortwave radiation varies with the positions on the earth's surface (i.e. latitude) in relation to the sun. The fraction of reflected shortwave radiation from the earth's surface is a function of the surface type and land wetness condition. Incoming and outgoing longwave radiation are radiation emitted by the atmosphere and earth's surface respectively. Emittance of longwave radiation is described by the Stefan Boltzmann law. The radiation balance at the earth's surface is given by:

$$R_n = (1-r_0)K\downarrow + \epsilon' \sigma T_a^4 - \epsilon_0 \sigma T_0^4 - (1-\epsilon_0) \epsilon' \sigma T_a^4 \quad (2.4)$$

where r_0 (-) is the surface reflectance or albedo, $K\downarrow$ (W m^{-2}) is the incoming shortwave radiation, T_0 (K) is the surface temperature, T_a (K) is the air temperature, ϵ' (-) is the atmospheric emissivity, ϵ_0 is the surface emissivity and σ (-) is the Stefan-Boltzmann constant ($\sigma = 5.67 \times 10^{-8} \text{ W m}^{-2} \text{ K}^{-4}$).

2.3 Transport processes of water vapour, heat and momentum

Diffusion is the process by which the properties of a fluid (e.g. heat, momentum, concentration of its molecules) are transferred from one part of the fluid to another. Diffusion can take place in two physically different ways: molecular or turbulent diffusion. Molecular diffusion is caused by the difference in concentration of the property of the fluid. The molecules making up a fluid are in random motion and exchange of molecules in neighboring positions takes place. This exchange occurs in the thin laminar layer between the evaporating surface and the atmospheric boundary layer.

Turbulence above the land surface occurs when air moving over the earth's surface is retarded by a surface feature, causing irregular vertical movement of pockets of air and with it transferring the atmospheric properties. Turbulence is more effective in the transfer of mass, momentum and heat than molecular diffusion and it is the dominant transport mechanism. Turbulence can also be produced by vertical temperature gradients. This type of turbulence is called free convection, while frictional turbulence is referred to as forced convection. If free convection is present, a combination of free and forced convection arises, leading to mixed

convection. Forced convection is usually determined first and then corrected for the effects of free convection.

The rate of transport by turbulence diffusion is governed by the wind speed and the concentration gradient of the transported entity in the air. The gradient of wind speed u (m s^{-1}) with height z (m) above a surface follows a logarithmic profile relation described by:

$$\frac{du}{dz} = \frac{u_*}{k(z-d)} \quad (2.5)$$

where k (-) is von Karman's constant, d (m) is the zero plane displacement and u_* (m s^{-1}) is the frictional velocity. The zero plane displacement d depends on the characteristics of the surface cover and is negligible at low values of specific leaf area density (Inoue, 1963). Furthermore, if z is much greater than d , the need to describe d may be ignored. The wind velocity can be described by integrating Eq. 2.5 from the roughness length for momentum z_{0m} (m) to the reference height z :

$$u(z) = \frac{u_*}{k} \ln\left(\frac{z-d}{z_{0m}}\right) \quad (2.6)$$

The roughness length z_{0m} is defined physically as the height above the surface where the logarithmic wind speed profile decreases to zero. The roughness length for momentum, z_{0m} , depend on the height and spacing of the surface cover. The frictional velocity, u_* , describes all the turbulence together and is defined in terms of shearing stress and momentum flux:

$$\tau = \rho_a u_*^2 \quad (2.7)$$

where τ (N m^{-2}) is the momentum flux density and ρ_a (kg m^{-3}) is the density of air. The transfer of momentum can also be described according to the K- theory:

$$\tau = \rho_a K_m \frac{\partial u}{\partial z} \quad (2.8)$$

where K_m ($\text{m}^2 \text{s}^{-1}$) is the eddy diffusivity which can be specified as:

$$K_m = ku_*(z-d) \quad (2.9)$$

The transport mechanism for water vapour and sensible heat transfer are similar to momentum transfer:

$$E = -\rho_a K_v \frac{\partial q}{\partial z} \quad (2.10)$$

$$H = -\rho_a c_p K_h \frac{\partial T}{\partial z} \quad (2.11)$$

where c_p ($\text{J kg}^{-1}\text{K}^{-1}$) is the specific heat of air, q (kg kg^{-1}) is the specific humidity and T is the potential temperature. K_v and K_h are eddy diffusion coefficients for water vapour and heat respectively and they are formulated similar to K_m under neutral conditions.

The turbulent transfer of all the three entities can be considered equal provided there is no temperature gradient. However, during daytime air heats up. Warm air is moved upwards by free convection and is more buoyant than the cooler air at the height to which it has been moved to. The upward ascent of air will therefore be enhanced by temperature differences. This atmospheric flow condition is referred to as an unstable atmosphere. When air temperature increases with height, as is prevalent during the night, the opposite happens. The buoyant forces dampen the upward ascent of air from the surface and such a condition is known as stable atmosphere.

Eqs. 2.8, 2.10 and 2.11 are valid only in the case of a neutral atmospheric condition (no buoyancy). The effect of the modification of forced convection by temperature gradient on momentum transfer can be corrected for by dimensionless parameters. One of the widely used dimensional parameter is known as the Monin-Obukhov correction factor. The wind profile under non-neutral flow conditions is modified to:

$$\frac{du}{dz} = \frac{u_*}{k(z-d)} \phi_m(\xi) \quad (2.12)$$

where $\phi_m(-)$ is the correction factor and ξ is the ratio of z and the so-called Monin-Obukhov length, L (m). The Monin-Obukhov length is defined as the ratio of the mechanical production of kinetic energy divided by free convective production of turbulent kinetic energy. Physically, the Monin-Obukhov length represents the height in the boundary layer where frictional forces equal the buoyancy forces:

$$L = - \frac{\rho_a c_p u_*^3 T_a}{kgH} \quad (2.13)$$

where g (m^{-2}) is the acceleration due to gravity and T_a is the mean air temperature of the flow region under consideration. The Monin-Obukhov length is negative under unstable conditions and positive in the case of stable conditions. The most frequently used ϕ -functions for unstable conditions are (Dyer and Hicks, 1970):

$$\phi_m = \left(1 - 16 \frac{z}{L}\right)^{-0.25} \quad (2.14)$$

and for stable conditions:

$$\phi_m = 1 + 5 \frac{z}{L} \quad (2.15)$$

The eddy diffusion coefficient for momentum without the zero-plane displacement can now be described as:

$$K_m = \frac{kzu_*}{\phi_m} \quad (2.16)$$

The application of the similarity hypothesis of wind, temperature and humidity profiles in the surface layer to temperature and water vapour profiles yields the following expressions for the eddy diffusion coefficients for heat and water vapour transport (Brutsaert, 1982):

$$K_h = \frac{kzu_*}{\phi_h} \quad (2.17)$$

$$K_v = \frac{kzu_*}{\phi_v} \quad (2.18)$$

In a stable atmosphere, ϕ_h is considered to be equal to ϕ_m whereas in an unstable atmosphere $\phi_h = \phi_m^2$ applies. The Monin-Obukhov function for water vapour, ϕ_v , is treated as equal to ϕ_h under all conditions (Monin and Yaglom, 1971). Substituting for u^* in Eq. 2.12, the water vapour and heat transfers become:

$$E = -\rho_a k^2 (z-d)^2 \frac{\partial u}{\partial z} \frac{\partial q}{\partial z} (\phi_v \phi_m)^{-1} \quad (2.19)$$

$$H = -\rho_a c_p k^2 (z-d)^2 \frac{\partial u}{\partial z} \frac{\partial T}{\partial z} (\phi_h \phi_m)^{-1} \quad (2.20)$$

2.4 Combination equation for evaporation

The calculation of E and H from equation 2.19 and 2.20 is difficult because measurement of derivatives is problematic in practice. The surface fluxes H and λE are therefore often parameterized. The most common simplification to represent differential diffusion equations for vapour and heat transport is analogous to Ohm's law for electric current:

$$F = \frac{c_1 - c_2}{r_{1,2}} \quad (2.21)$$

The flux density F are analogous to current and the potential difference is analogous to difference in entity c (e.g. water vapour, temperature and wind), between two representative locations. The resistance takes into account the flow obstruction of the flux densities between the reference locations. Thus, for the sensible heat flux density one can write:

$$H = \rho_a c_p \frac{T_1 - T_2}{r_{ah}} \quad (2.22)$$

where r_{ah} (s m^{-1}) is the aerodynamic resistance to heat transfer. The temperatures T_1 and T_2 apply to the reference levels $z = z_1$ and $z = z_{12}$ (see Fig.2.1). The aerodynamic resistance follows from the height integration of K_h :

$$r_{ah} = \int_{z_1}^{z_2} \frac{1}{K_h} dz = \int_{z_1}^{z_2} \frac{\phi_h(z, L)}{ku_* z} dz \quad (2.23)$$

The ϕ_h function is integrated from 0 to ξ to get a stability correction ψ_h :

$$\psi_h(\xi) = \int_0^\xi \left[\frac{1 - \phi_h(\xi)}{\xi} \right] d\xi \quad (2.24)$$

By further using the expression of ϕ_h and neglecting the zero-plane displacement d , the integrated stability function ψ_h can also be described analytically (Paulson, 1970):

$$\text{for unstable conditions:} \quad \psi_h(\xi) = 2 \ln \left[\frac{1 + x^2}{2} \right] \quad (2.25)$$

$$\text{with } x = \left(1 - 16 \frac{z}{L} \right)^{0.25}$$

$$\text{and for stable conditions:} \quad \psi_h(\xi) = -5 \frac{z}{L} \quad (2.26)$$

The integrated resistance to heat transfer, after inserting the stability correction equation, becomes:

$$r_{ah} = \frac{1}{ku_*} \left[\ln \left(\frac{z_2}{z_1} \right) - \psi_h \left(\frac{z_2}{L} \right) + \psi_h \left(\frac{z_1}{L} \right) \right] \quad (2.27)$$

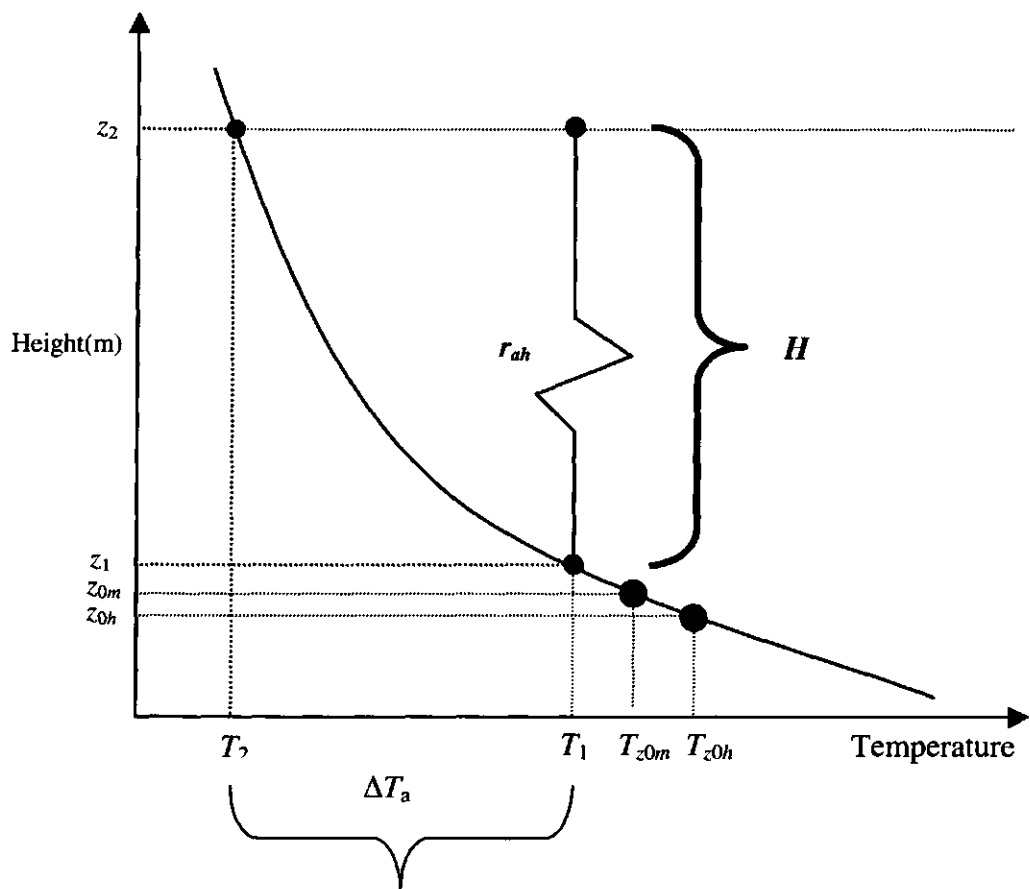


Figure 2.1. The logarithmic profile of air temperature T_a in relation to integration limits z_1 , z_2 , z_{0m} and z_{0h} for the definition of the aerodynamic resistance r_{ah} . The heat source temperature T_{z0h} , aerodynamic temperature T_{z0m} and temperature taken at arbitrary levels z_1 and z_2 as T_1 and T_2 respectively are shown

The soil heat flux depends on the soil thermal properties and the temperature gradient of the top soil. In a similar diffusivity-resistance method applied to H , G_0 can be expressed as (Menenti, 1984; Choudhury and Monteith, 1988):

$$G_0 = \rho_s c_s \frac{T_0 - T_s}{r_{sh}} \quad (2.28)$$

where ρ_s is the density of the soil, c_s is the specific heat of the soil, T_0 is the surface temperature, T_s is the soil temperature at some reference depth near to the surface to minimize storage effects and r_{sh} is the soil resistance. The soil heat resistance is obtained by integrating the soil thermal diffusivity between the reference depth in the soil and the surface.

The transport of latent heat can be similarly expressed as:

$$\lambda E = \frac{\rho_a c_p (e_0^* - e_z)}{\gamma(r_{av} + r_s)} \quad (2.29)$$

where e_0^* (hPa) is the saturated vapour pressure at the evaporating surface, γ (hPa K⁻¹) is the psychrometric constant, e_z is the actual vapour pressure at height z , r_{av} (s m⁻¹) is the resistances to water vapour transfer in the atmosphere and r_s is the surface resistance to vapour transfer. Usually, r_{av} is considered to be equal to r_{ah} because $\psi_v = \psi_h$.

Monteith (1965) used the formulation of the transport equations (Eqs. 2.22 and 2.29) in conjunction with the surface energy balance (Eq. 2.3) and a Taylor expansion of $e_0^* = e^*(T_a) + s(T_0 - T_a)$ to derive a surface energy balance combination equation for canopy evaporation, where e^* is the saturated vapour pressure at air temperature T_a at height z . Earlier, Penman (1948) derived this combination equation for open water surfaces and hence the energy balance combination equation for canopy evaporation is referred to as the Penman-Monteith equation:

$$\lambda E = \frac{s(Rn - G_0) + \rho_a c_p (e_z^* - e_z) / r_{ah}}{s + \gamma(1 + \frac{r_c}{r_{ah}})} \quad (2.30)$$

where r_c is the canopy resistance. In leaves, the rate of vapour transport is controlled by the opening and closing of stomata, referred to as stomatal resistance. The stomatal resistance, at the leaf and canopy scales, has been correlated to environmental conditions and plant factors. However so far no mechanistic model is available to describe the stomatal behavior.

The most common approach to parameterize the effect of environmental conditions on stomatal behaviour is the so-called Jarvis-Stewart type models. Jarvis (1976) related stomatal conductance (reciprocal of stomatal resistance), to incoming solar radiation, leaf water potential, air temperature, vapour pressure deficit and carbon dioxide concentration in the atmosphere. The relationship between these environmental variables and stomatal conductance is reduced by stress functions interacting without synergy. The Jarvis-Stewart model for canopy resistance is given by:

$$r_c = \frac{r_{s \min}}{LAI F_1(K \downarrow) F_2(T_a) F_3(\Delta e) F_4(\Psi)} \quad (2.31)$$

where Δe is the vapour pressure deficit, LAI is the leaf area index and Ψ is the leaf water potential. Each stress function varies from zero to unity. The coefficients of the functions are determined from statistical analysis obtained from dedicated field experiments or under controlled laboratory environments. The functions have been expressed in slightly different ways, depending on vegetation or biome types such as forests (Stewart, 1988), agricultural crops (Dolman, 1993) and grasslands (Stewart and Gay, 1989; Hanan and Prince, 1997). The influence of $K \downarrow$ can be expressed as a hyperbolic function:

$$F_1(K \downarrow) = \frac{c + K \downarrow}{dK \downarrow} \quad (2.32)$$

where $d=1+c/1000$. The value of c is empirically determined. The effect of temperature may be represented as a power function:

$$F_2(T_a) = \frac{(T_a - T_{\min})(T_{\max} - T_a)^b}{(a_3 - T_{\min})(T_{\max} - a_3)^b}, \quad b = \frac{T_{\max} - a_3}{a_3 - T_{\min}} \quad (2.33)$$

where T_{min} is the minimum air temperature, T_{max} is the maximum air temperature for stomatal conductance and a_3 is a coefficient representing the optimum air temperature for stomatal conductance.

The vapour pressure deficit function is given as follows:

$$F_3(D) = \frac{1}{1 + a_4 \Delta e} \quad (2.34)$$

where Δe is the vapour pressure deficit (hPa) and a_4 is an empirical coefficient.

Leaf water potential is usually not available and is replaced by soil water potential (Choudhury and Idso, 1985; Hanan and Prince, 1997) or soil moisture deficit (Dolman et al., 1991). Slightly different functions have been used for the influence of soil water potential but they are in the general form:

$$F_4(\Psi) = \left(1 - \frac{\Psi_L}{\Psi_c}\right)^n \quad (2.35)$$

where Ψ_L is the soil water potential and Ψ_c is the soil water potential at the wilting point.

Many of the Jarvis-Stewart type of models do not take into account all the four functions as the influence of some of environmental factors under given conditions is minimal. For example, when soil moisture deficit is very small throughout the year, F_4 can be omitted as it becomes equal to 1. Dolman et al. (1988) showed in the study of a forest in the United Kingdom, that models without soil moisture or humidity components will give considerable errors if applied over a season where variation in climate and soil conditions occur. Stewart (1988), also emphasized the importance of accounting for the effects of soil moisture in order to get reliable E estimates.

In the case of evaporation from bare soils, an explicit soil resistance has to be parameterized in terms of known soil variables. The evaporation of soil is composed of the transport of water to the soil surface by both liquid and vapour

phases. The transport of liquid water to the surface can be described in terms of a physical resistance to liquid flow:

$$E_L = \rho_w \frac{\theta_{z_1} - \theta_0}{r_{sl}} \quad (2.36)$$

where, θ_{z_1} and θ_0 are soil moisture contents at depths z_1 and at the surface. The resistance to liquid transport r_{sl} is given by:

$$r_{sl} = \int_{-z_1}^0 \frac{dz}{D(\theta)} \quad (2.37)$$

where $D(\theta)$ is the diffusivity for liquid water. Diffusivity is a function of hydraulic conductivity and depends on the soil physical characteristics. Dry soils exhalate vapour through air-filled pores. Transport of vapour flow to the soil surface from the evaporation front at depth $-z_e$ can be represented as:

$$E_v = \frac{\rho_v^{sat}(T_{z_e}) - \rho_{0v}}{r_{sv}} \quad (2.38)$$

where r_{sv} is resistance to vapour transport, $\rho_v^{sat}(T_{z_e})$ is the saturated vapour density (kg m^{-3}) at the soil temperature at the evaporating front, ρ_{0v} is the vapour density at the soil surface. The resistance to vapour transport is determined by integrating the effective vapour diffusivity vertically from the evaporation front to the soil surface:

$$r_{sv} = \int_{-z_e}^0 \frac{1}{D_v^{eff}} dz \quad (2.39)$$

where D_v^{eff} is the effective vapour diffusivity, which is related to the diffusivity of water vapour in the air. In most conditions, E_L is much larger than E_v (except in desert conditions) and evaporation is consequently schematized to occur from the soil surface with temperature T_0 (Bastiaanssen, 1995):

$$E_{soil} = E_L + E_v = \frac{\rho_v^{sat}(T_0) - \rho_{z0v}}{r_{soil}} = \frac{\rho_w(\theta_1 - \theta_0)}{r_{sl}} \quad (2.40)$$

The description of the energy and water diffusion from a combination of plants and soils into the atmosphere requires a network of resistances rather than a single surface resistance in the parameterization scheme. These parameterization schemes calculate available energy at different heights and then use the resistance chain to determine the profiles of temperature, wind speed and humidity (e.g. Shuttleworth and Wallace, 1985; Choudhury, 1989; Dolman, 1993). The flux densities above the vegetation and soils can be combined by weighing coefficients, which may be based on fractional soil coverage or leaf area index.

The resistances networks in the multi layer schemes can be combined by assuming they are in parallel at a single level in the canopy. The single-layer schemes assume either complete vegetation or complete soil cover. The single-layer is simple and is less data demanding. They require for example half the parameters as a two-layer scheme. Previous studies have shown that single-layer schemes can realistically predict the surface fluxes and are therefore suitable for applications in regional studies (e.g. Beljaars and Holtslag, 1991; Bouglet et al., 1991). The Penman-Monteith equation is a single layer scheme. The surface resistance r_s is the overall resistance of water transfer from the roots through the canopy and from the soil into the atmosphere. The surface in these resistance formulations is parameterized as one big leaf. Stewart (1988) extended the Jarvis-Stewart model (Eq. 2.31) to describe surface conductance (reciprocal of surface resistance). Stewart derived the surface conductance from λE measured above a forest by inverting the Penman-Monteith equation. Because measured total evaporation over a canopy is used, the Jarvis-Stewart model implicitly accounts for soil resistance through the optimized coefficients.

2.5 Remote sensing evaporation algorithms

Steps in the retrieval of E from remote sensing data

Remote sensing methods use surface reflectances and radiometric surface temperature from satellite spectral data in combination with ground based meteorological data to solve the energy balance equation and estimate evaporation

from local to regional scales. Extensive reviews of remote sensing flux determination methods have been presented by Choudhury, (1989), Moran and Jackson, (1991), Menenti, (1993) and Kustas and Norman, (1996).

Fig.2.1 shows the steps involved in retrieving evaporation from satellite data. Satellite radiances are related to evaporation in two steps. First, the surface parameters such as surface reflectance or albedo, surface temperature and vegetation indices are derived. These surface parameters together with field data, are then used to solve the energy balance and evaporation is taken as a residual term. The required field data is measured, estimated, modelled or ignored. Since satellite data are obtained at the top of the atmosphere, corrections for atmospheric interference have to be made. The corrections are based on information on the atmospheric properties (e.g. temperature, humidity and wind speed) at the time of satellite overpass and the use of radiative transfer models. However atmospheric information is usually not available and hence simpler correction procedures have to be resorted to. For example surface parameters could be measured at a few locations for calibrating the satellite derived surface parameters.

Type of remote sensing algorithms

Remote sensing methods vary in complexity due to the amount of physics they describe. They can be grouped into three major classes according to their complexity (Kustas and Norman, 1996):

- Statistical/semi-empirical methods
- Physically based analytical approaches
- Numerical simulation models.

The *statistical methods* directly relate the difference between satellite observed surface temperature and air temperature to E (e.g. Jackson et al., 1977; Seguin and Itier, 1983). The statistical methods are simple and require few input data, however, apart from surface temperature all the other input variables are assumed spatially constant. This limits the application of the statistical methods to homogeneous fields or regions only.

In the *physically based methods* R_n , G_0 and H are evaluated separately and λE is determined as a residual in Eq. 2.3 (e.g. Carlson and Buffum, 1989; Diak and

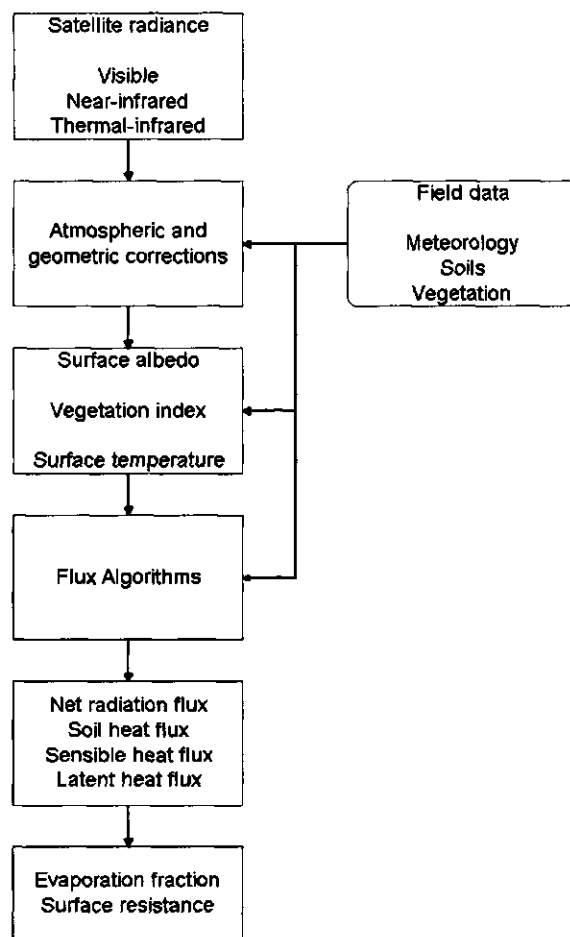


Fig. 2.2. The Steps followed in the retrieval of evaporation from spectrally reflected and emitted satellite radiances

Whipple, 1993). The net radiation, R_n is estimated from remotely sensed surface albedo, surface temperature and solar radiation calculated from standard astronomical formulae (Iqbal, 1983). The ground heat flux, G_0 is determined through semi-empirical relationships with R_n , surface albedo, surface temperature and vegetation index.

The sensible heat flux density as given by Eq. 2.22 is solved and this is the most critical factor in the remote sensing algorithms. The main challenge is to quantify the spatial and temporal variations of T_1 , r_{ah} and T_1 as they are not directly observable from remotely sensed data. In many models, T_1 is taken as equal to remotely sensed T_0 (Kalma and Jupp, 1990; Lhomme et al., 1994). However, although for uniform canopies the difference between T_1 and T_0 is less than 2°C, the differences are larger for partial canopies (Choudhury et al., 1986; Kustas 1990; Troufeau et al., 1997). In order to account for the discrepancy between T_1 and T_0 some investigators have adjusted r_{ah} or used an additional resistance term (e.g. Sugita and Brutsaert, 1990; Stewart et al., 1994). This is achieved by defining the roughness length for heat transport, z_{0h} as equal to the height at which $T_0 = T_{z_{0h}}$, through a factor kB^{-1} which relates z_{0h} to the roughness length for momentum transport, z_{0m} .

$$kB^{-1} = \ln \frac{z_{0m}}{z_{0h}} \quad (2.41)$$

However, different studies have shown that there is a wide range of kB^{-1} from 1 to 12 for different surfaces (Beljaars and Holstlag, 1991; Brutsaert et al., 1993). This indicates that it may not be feasible to determine the spatial variations kB^{-1} in heterogeneous landscapes. In fact, Verhoef et al., (1997) questioned whether the concept of kB^{-1} itself is correct. They argue that the definition of z_{0h} is based on extrapolating a theoretical profile through a region where this theoretical profile does not hold, towards a surface temperature that is difficult to locate, especially in sparse vegetation.

To avoid the problems associated with the concept of kB^{-1} and circumvent its use in the calculation of H , other methods have been proposed. Qualls et al., (1993) in a study of the fore Alps of Switzerland, used a near-surface air temperature (T_1) instead of $T_{z_{0h}}$ to derive H in a procedure developed from the standard Monin-Obukhov flux-profile relationship for the atmospheric surface layer (see Fig. 2.2). Through calibration, they found a surface transport parameter z_{1h} to correspond to

T_1 . Qualls et al., (1993) report obtaining good estimates of H by using this procedure and recommend its use to calculate regional E by means of the energy budget from the profile derived H . Chehbouni et al., (1997) and Troufleau et al., (1997) used a relationship that links T_{z0h} and T_0 . They formulated H as follows:

$$H = \rho_a C_p \eta \frac{T_0 - T_a}{r_{ah}} \quad (2.42)$$

where, η is the ratio of $(T_0 - T_{z0h})$ and $(T_0 - T_a)$. The factor η is a function of the fraction of vegetation cover on the surface. It can be considered to be a constant for a given day but decreases with increasing LAI over a season. A formula was developed to determine η :

$$\eta = \frac{1}{\exp(D/(D - LAI)) - 1} \quad (2.43)$$

where D is an empirical factor that depends on the vegetation type. Equation 2.42 was tested and found valid for the HAPEX-Sahel sites. The simplicity of this method and the possibility to use remote sensing to determine LAI and T_0 , makes it an attractive method to determine surface fluxes from remote sensing in semi-arid regions.

Another approach to overcome the problem of inferring T_{z0h} from T_0 is to directly estimate ΔT_a , the temperature difference between T_1 and T_2 taken at two arbitrary levels z_1 and z_2 without explicitly solving the absolute temperature at a given height (see Fig 2.2). The latter can be achieved from the inversion of the sensible heat transfer equation (Bastiaanssen et al., 1998b):

$$T_1 - T_2 = \Delta T_a = \frac{H r_{ah}}{\rho_a c_p} \quad (2.44)$$

where $H = R_n - G_0$ for dry surfaces. Furthermore, it has been experimentally proven that land surfaces with high ΔT_a are associated with high thermally emitted radiances and those with low ΔT_a are coincide with low thermally emitting surfaces. The temperature difference, ΔT_a , may therefore be obtained across an image by relating it linearly to T_0 :

$$\Delta T_a = c_1 T_0 - c_2 \quad (2.45)$$

where c_1 and c_2 are regression coefficients valid for one particular moment and region. The linearity of Eq. 2.45 has been shown to be correct in field experiments carried out in Egypt and Niger (Bastiaanssen et al., 1998a), China (Wang et al., 1998), USA (Frank and Beven 1997) and Kenya (Farah and Bastiaanssen, 2000).

The sensible heat flux is apart from vertical temperature differences also a function of u_* . Many algorithms therefore take a few field measurements of u_* and treat them as spatially constant (e.g. Hall et al, 1992; Kalman and Jupp, 1990; Rosema, 1990). This assumption is only valid for uniform homogeneous surfaces. One way of overcoming this problem is to consider u_* at 50 or 100m above ground level rather than the usual 2m level (Mason, 1988). The reasoning is that at these heights, called blending height, u_* is not affected by local surface heterogeneity and is therefore spatially constant. Bastiaanssen (2000) made u_* spatially variable by using a spatially constant wind speed at the blending height and spatially variable roughness length for momentum transport $z_{0m}(x,y)$ together with local stability correction functions $\Psi_m(x,y)$.

Finally *Numerical models* simulate continuously the surface energy flux exchanges by solving numerical equations of the energy and mass flow processes in the soil-vegetation-atmosphere system (e.g. Sellers et al., 1992; Carlson et al., 1995). Many input parameters describing soil-vegetation-atmosphere system properties are required which are seldom available in tropical watersheds. Numerical models are therefore less suitable for satellite remote sensing-hydrology studies in data-scarce environments.

Chapter 3

Description of the study area

3.1 Geographical setting

Location and climate

The Naivasha basin is located in the central rift valley of Kenya. It lies approximately between latitudes $0^{\circ} 10'S$ to $1^{\circ} 00'S$ and longitudes $36^{\circ} 10'E$ to $36^{\circ} 45'E$ and covers an area of about 3500 km^2 . The location of the basin is shown in Fig. 3.1. The altitude of the basin varies from about 1900 m at the bottom of the valley to 3200 m in the Nyadarua mountains found on the eastern boundary of the basin. Due to the altitudinal differences, there are diverse climatic conditions found in the basin. The climate varies from semi-arid to humid tropical.

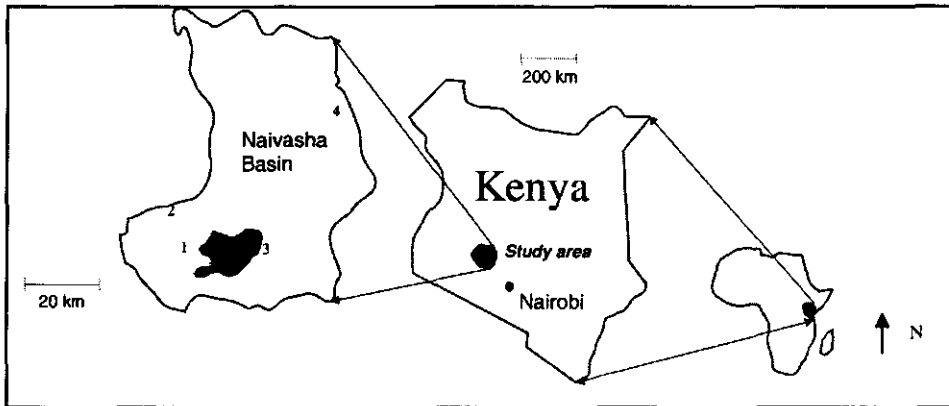


Fig. 3.1. Location of study area showing the Ndabibi (1) and Eburu (2) experimental sites and the meteorological stations Naivasha town (3) and North Kinangop (4)

Rainfall varies from about 600 mm to 1200 mm annually. Despite being located on the equator, the area experiences relatively cool conditions. Average monthly temperature ranges from 15°C to 18°C , with the average maximum and minimum in the ranges 24°C to 29°C and 6°C to 8°C respectively. Fig. 3.2 shows the monthly trend of rainfall and temperature at two points located at 1930 m and 2630

m. There are two rainfall peaks which occur in April to May and September to October. The driest months are January, February and December. The lowest temperatures are experienced in July, while the highest temperatures occur in March. The potential evaporation is about twice the annual rainfall in the semi-arid area, while in the humid zones rainfall exceeds potential evaporation in most parts of the year.

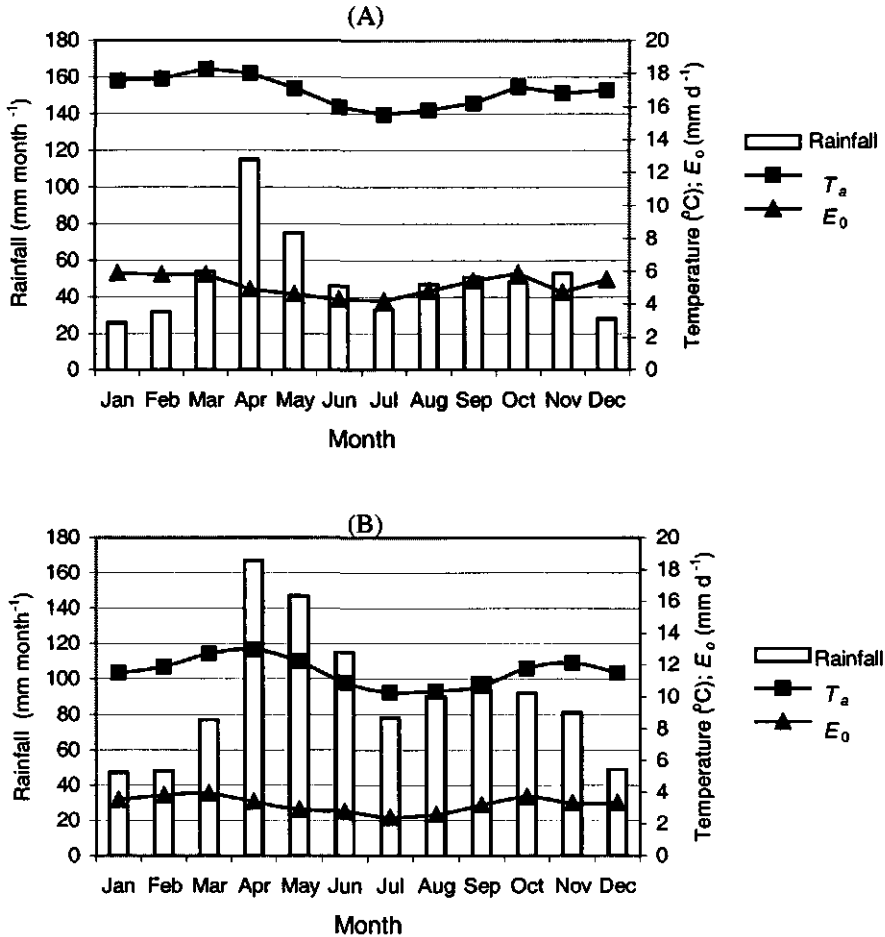


Fig.3.2. Monthly average rainfall, average daily temperature (1931-1983) and average daily reference evaporation (E_0 -Penman-Monteith) (1974-1983) at two stations: (A) Naivasha town at altitude 1906 m and (B) North Kinangop at altitude 2620 m. The location of the stations is shown in Fig. 3.1

Topography and soils

The topography of the plateaus on the eastern side of the basin and the plains inside the rift valley is gently undulating. These areas are found at altitudes between 1900 m and 2400 m. The plateaus and plains, together with Lake Naivasha, cover about 90% of the basin. The rest is mountainous with rough terrain (see Fig. 3.3). The soils in the higher plateaus consist of clay loam to clay. These soils are deep (80 cm to 120 cm) and have good water holding capacity. In the lower plains, the soils are mainly sandy clay loam to sandy clay, and are deep and well drained. On the mountains, the soils are shallow (< 50 cm) to moderately deep and consist of a complex of loam, clay loam and clay.

Land use and land cover

In the humid highland zones, forests, woodlands and croplands are found. Agriculture is also practiced in the semi-humid to sub-humid regions. The main crops are maize, potatoes, coffee and wheat. The semi-arid regions are found inside the rift valley. They have extensive grasslands and bushlands, which are used for livestock grazing. Around Lake Naivasha intensive horticultural farming under irrigation is common. The main products are flowers, vegetables and fruits. About 80% of the national horticultural production in Kenya comes from this area. To the south of Lake Naivasha, there is a geothermal power plant that produces about 18% of the total power in the country. There are two national wildlife reserves that attract numerous tourists. Declared a Ramsar site in 1995, Lake Naivasha is considered a wetland of international importance. There has been an increasing demand for water in the basin in the last 30 years due to settlement of the plateaus by small-scale farmers and the introduction of intensive irrigated horticulture around Lake Naivasha.

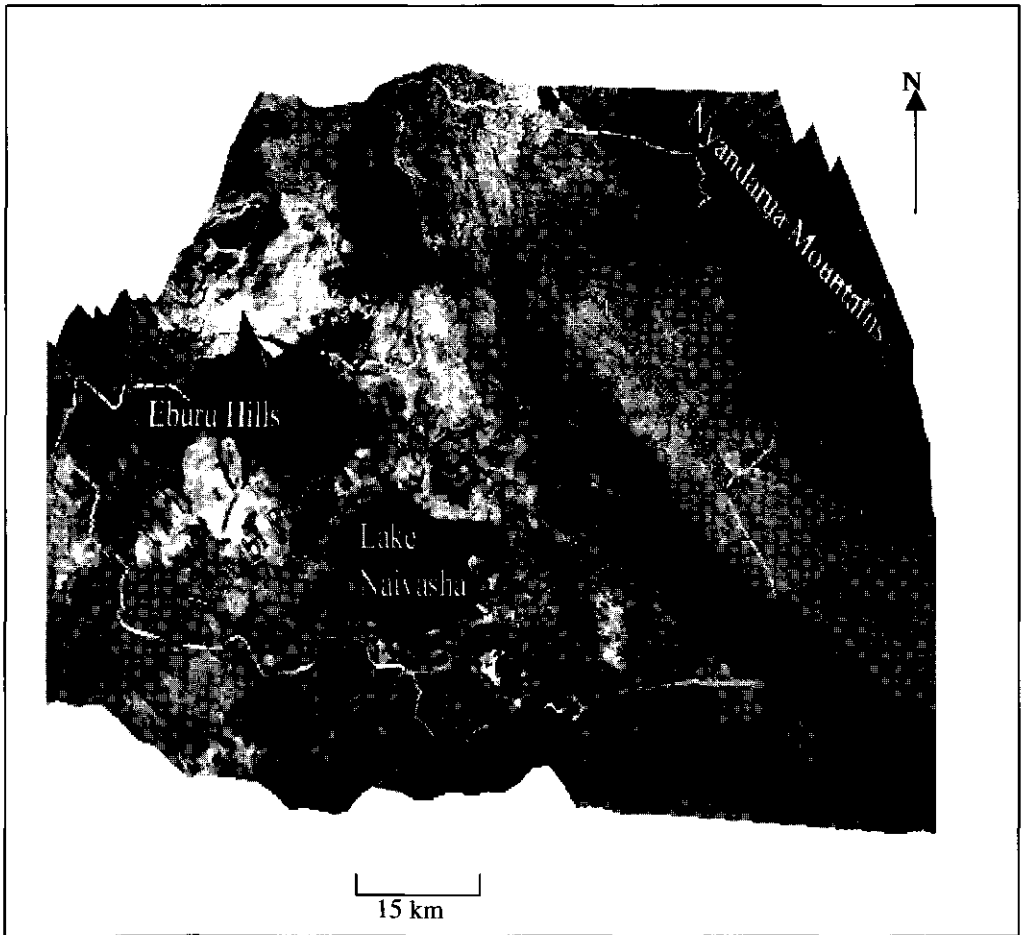


Fig. 3.3. Illustration of the topography and vegetation of the Naivasha catchment prepared from Landsat TM false color composite image overlaid on a digital elevation model of the area. The dark red areas are forests on mountains, light red tones indicate cropland and woodlands on the plateaus. The purple whitish tones represent grassland and bushland in the valley plains (see color version in Appendix B).

3.2 Field experiments

The field experiments consisted of the measurement of actual $E(a, t)$ at two sites by means of the Bowen ratio energy balance method. The two sites are located at Ndabibi and Eburu (see Fig. 3.1). The measurements were performed from 14 May 1998 to 24 April 1999 at Ndabibi and from 27 September 1998 to 24 April 1999 at Eburu. Two field campaigns were also carried out in October 1998 and March 1999 at three other sites with different surface cover conditions from Ndabibi and Eburu. Actual E was measured for two days at each of the other sites during the field campaigns.

Ndabibi site

Ndabibi is situated in the semi-arid plains west of Lake Naivasha at an altitude of 2010 m (see Fig. 3.4). It is a flat area with extensive grassland, surrounded by wheat and maize farms. The soils are sandy clay to clay loam and are classified as deep. This site was selected so that the measurements made would be representative of a larger area and match the pixel size of satellite images used in this study (30 m to 1 km).

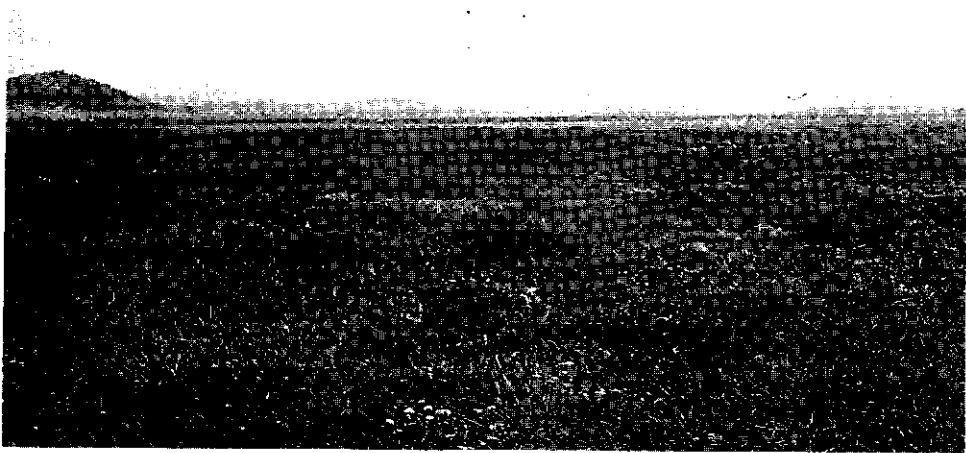


Fig. 3.4 Land surface conditions at the Ndabibi site showing the extensive flat grasslands

A Bowen ratio tower was erected at the site. Air temperature T_a and Relative humidity RH were measured at two levels (0.3m and 2m) with temperature and humidity sensors having an accuracy of $\pm 0.2^\circ \text{C}$ and 1% relative humidity. Incoming solar radiation $K\downarrow$ was measured with a pyranometer with a sensitivity of 1.5%. Rainfall was measured with a tipping bucket rain gauge. These measurements were collected automatically by data loggers and recorded as 20-minute averages. In addition, surface reflectance r_0 and surface temperature T_0 were measured one day per month at one-hour intervals. Table 3.1 shows the details of the measurements. There is a period of 36 days in February and March 1999 with missing data due to malfunctioning of the data logger.

Table 3.1: Measured meteorological parameters at the Ndabibi and Eburu experimental sites

Measured Parameter	Height above surface level (m)	Measurement interval	Instrument	Type	Accuracy
Air Temperature T_a	0.3, 2.0	20 minutes	Thermocouple	Eijkelkamp	0.2°C
Relative humidity RH	0.3, 2.0	20 minutes	Thermocouple	Eijkelkamp	1%
Shortwave radiation incoming $K\downarrow$	4.0	20 minutes	Pyranometer	Kipp and Zonnen	1.5%
Shortwave reflected radiation $K\uparrow$	0.5	1 hour	Pyranometer	Kipp and Zonnen	1.5%
Rainfall	0.3	1 hour	Tipping bucket	Eijkelkamp	1%
Surface temperature T_0	0.3	1 hour	Thermal infrared radiometer	Eijkelkamp	0.1°C

Fig.3.5 shows a typical diurnal course of T_a , RH , $K\downarrow$, net available energy $R_n - G_0$ and latent heat flux λE . It can be seen that the amount of incoming solar radiation is large. However, the air temperature does not rise above 30°C because of the altitude of the site.

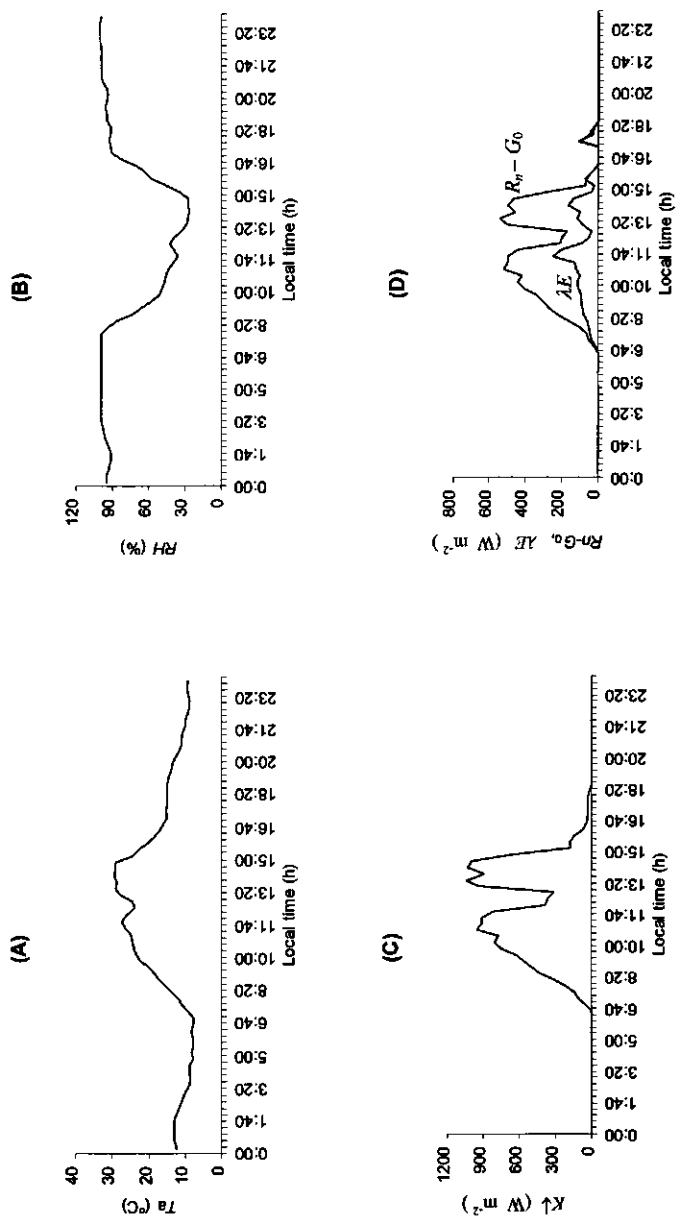


Fig. 3.5. Diurnal evolution of A) air temperature T_a B) relative humidity RH C) incoming solar radiation $K\downarrow$ and D) net available radiation $R_n - G_0$ and latent heat flux λE at Ndabibi site on October, 25 1998

Eburu site

The Eburu site has a sub-humid climate and is located in hilly terrain at an altitude of about 2500 m. The vegetation is composed of woodland with scattered trees and bushes (see Fig. 3.6). The soils here are deep and mainly clay loam. A Bowen ratio tower was put up and data similar to those at Ndabibi were collected (see Table 3.1).



Fig. 3.6. Land surface condition around the Eburu experimental site showing the scattered trees and bushes and hilly terrain

Fig. 3.7 shows the diurnal course of T_a , RH and $K\downarrow$. It can be observed that temperatures are lower than at the Ndabibi site because of the higher elevation of Eburu. The average daily solar radiation is slightly higher than at Ndabibi due to lower atmospheric turbidity on this particular day.

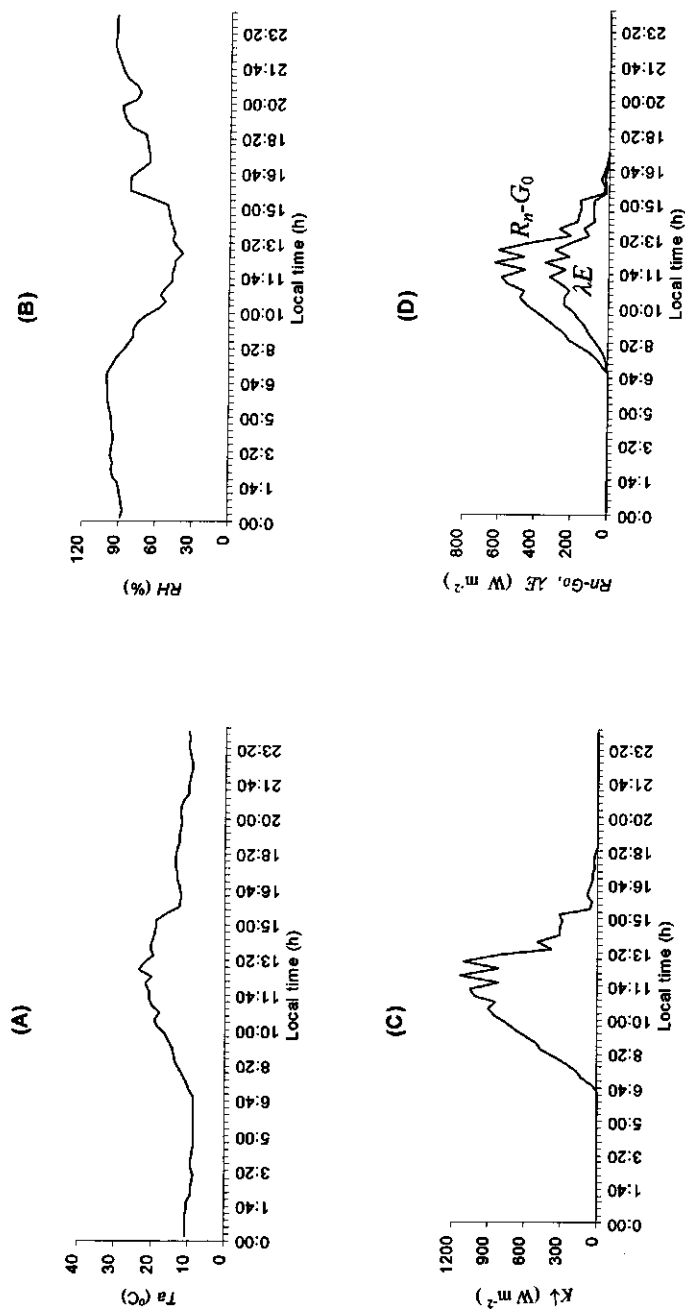


Fig. 3.7. Diurnal evolution of A) air temperature T_a B) relative humidity RH C) incoming solar radiation $K\downarrow$ and D) net available energy $R_n - G_0$ and latent heat flux λE at Eburu site on 25 October 1998

Chapter 4

The impact of spatial variations of surface parameters on regional evaporation: A case study with remote sensing data*

4.1 Introduction

Sensible H and latent heat fluxes λE vary spatially because of the heterogeneity of soil physical properties, terrain slope, land cover, and water influx through precipitation, irrigation and groundwater. The parameters of the Soil-Vegetation-Atmosphere-Transfer continuum exhibit a distinct spatial variation in watersheds. The spatial scale may vary from less than a meter to the size of watersheds. Time variations in terms of hours may be significant. Ground measurements of land surface fluxes are representative of a relatively small area. Land surface fluxes at the regional scale are therefore difficult to deduce from a limited number of *in situ* field stations equipped with advanced measurement devices. Satellite remote sensing methods have been used in the last 20 years to overcome these discrepancies in scale.

Remotely sensed multi-spectral measurements have been used to estimate parameters of Soil-Vegetation-Atmosphere-Transfer models (i.e. SVAT parameters). Surface temperature T_0 , is the most common SVAT parameter used to interpret spatial variation in evaporation E (e.g. Jackson et al., 1977). However, attempts have been made with many other SVAT parameters to explain variability in E : soil moisture (Chen et al., 1997), fractional vegetation cover v_c (Choudhury et al., 1994), leaf area index (Baret and Guyot, 1991), surface albedo r_0 (Jackson, 1984; Menenti et al., 1989b), surface thermal infrared emissivity ε_0 , (Valor and Caselles, 1996), air temperature T_a (Prihodko and Goward, 1997), crop height

* To be published in *Hydrological processes*, vol. 15, No. 3 as Farah, H. O. and W.G.M. Bastiaanssen, 2000. The impact of spatial variations of surface parameters on regional evaporation: A case study with remote sensing data.

(Moran et al., 1995) and surface roughness length for momentum transport z_{0m} (Moran and Jackson, 1991).

The sensible heat and latent heat fluxes can be parameterized as a simple linear function of T_0 , or the difference between T_0 and T_a . For instance, Seguin and Itier (1983) explained variation in E to variation in T_0 . This concept may correctly describe the fluxes emerging from homogeneous landscapes, e.g. agricultural systems with uniform crop stands and other biophysical properties. However, for heterogeneous watersheds with distinct variation in SVAT parameters and fluxes, the assumption of linearity between T_0 and fluxes does not hold, and the involvement of other SVAT parameters becomes essential. The relationship between fluxes and T_0 portrayed in Figure 4.1A for simultaneously measured T_0 and λE fluxes at 12 stations in the catchment of the Guadiana River (central Spain) indicates that the variance of fluxes cannot be explained by variations in T_0 alone. The scatter can only be explained by other scale variant SVAT parameters. Figure 4.1B shows the achievements of an integrated SVAT-Boundary Layer model study executed by Blyth (1994) which reveals, on the basis of general physics, that λE variations are not ascribed to variations in T_0 only.

Furthermore, surface energy balance models using remote sensing are mostly based on a one dimensional representation of the momentum and heat exchanges between the land and atmosphere (see Fig. 2.2). The selection of vertical length scale z_2 has impacts for the quantification and spatial variability of, for example, T_a and aerodynamic resistance, r_{ah} (and hence roughness length for heat transport z_{0h} , frictional velocity u_* , and stability correction factor Ψ_h). If z_2 is taken to be at some height, usually referred to as blending height, in the planetary boundary layer where fluxes are independent of surface features, then T_a and r_{ah} become spatially constant. However, since the spatial variation of T_a at the blending height for heat is eliminated by advection, the sensible heat flux between the land surface and the blending height is not strictly one-dimensional. If the purpose of study is to determine near-surface spatial variations of fluxes, z_2 has to be kept small and advection may be ignored (Bastiaanssen et al., 1996). At near-surface level (2 to 10m), there are differences in T_a and r_{ah} in the horizontal domain. These horizontal gradients are caused by the underlying local hydro-meteorological processes and have consequences for the way the spatial variations of SVAT parameters are schematized in the remote sensing algorithms, if correct fluxes have to be obtained.

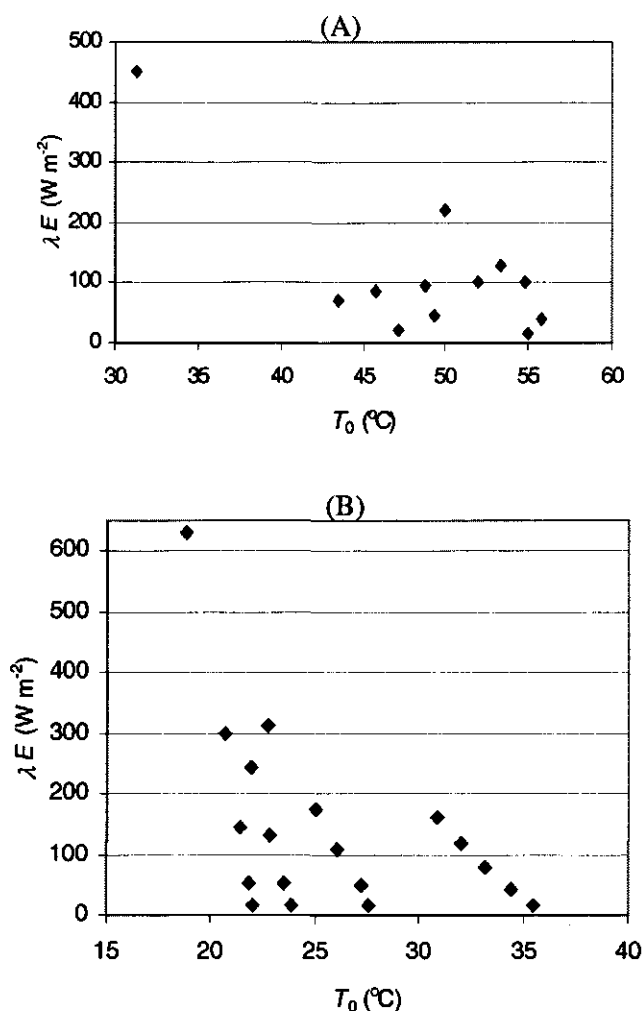


Fig. 4.1: Latent heat flux λE as a function of surface temperature T_0 . (A): field measurements in central Spain (Pelgrum and Bastiaanssen, 1997); (B): model simulation (Blyth, 1994)

Table 4.1 shows how different categories of remote sensing algorithms treat spatial variations of T_a and r_{ah} (z_{0h} , u_* and Ψ_h). It is evident that most algorithms take T_a , either at $z_2 \sim 2\text{m}$ or at greater height $z_2 \sim 100\text{m}$, as spatially constant. Table 4.1 also shows that u_* (i.e. momentum flux) is considered spatially constant by all algorithms

except Class 5. It is therefore prudent to investigate the influence of the spatial variability of SVAT parameters on surface fluxes for heterogeneous landscapes, so as to identify the parameters that should be treated minimally as spatially variable and those that can be taken as spatially constant.

Table 4.1: Application studies using conceptually different solutions for T_a and r_{ah} (c = spatially constant, v = spatially variable, n = not considered) (Modified from Bastiaanssen et al, 1996)

Classes of H- schematization	T_a $z_1 \sim 2m$	T_a $z_2 \sim 100m$	z_{0h}	u^*	ψ_h	References
Class 1	c	n	c	c	n	Jackson et al.,1977; Seguin and Itier,1983
Class 2	c	n	v	c	c	Kustas et. al.,1994; Kalma and Jupp, 1990
Class 3	n	c	c	c	c	Rosema, 1990; Brutsaert et al.,1993
Class 4	n	c	v	c	c	Meneti and Choudhury, 1994; Diake and Whipple 1993
Class 5	v	c	v	v	v	Carlson and Buffum, 1989; Bastiaanssen et al.,1998a

The modeling of spatial heterogeneity is usually achieved by delineating the surface into units of homogeneous hydrological characteristics and deriving SVAT parameters for each unit from which fluxes can be determined. The first objective of this Chapter is to demonstrate how, with the help of satellite remote sensing, a complex watershed can be delineated into hydrological units or partial areas. Watersheds with little data availability are the norm in both developing and developed countries and remotely sensed information is very useful for describing heterogeneous landscapes and related land surface processes. The second objective is the assessment of SVAT parameters and the accompanying surface fluxes of each hydrological unit discerned from the remote sensing measurements. The third objective is to study the consequences of using spatially constant SVAT parameters or watershed-distributed SVAT parameters on E .

4.2 Estimation of basic surface radiometric parameters

Landsat Thematic Mapper (TM) measures the spectral radiances in the visible, near, middle and thermal infrared spectrum at the top of the atmosphere. A TM scene of 21 January 1995, covering the Lake Naivasha watershed in Kenya, has been used in the current analysis. TM has 3 bands in the visible, 3 bands in the near- and middle-infrared and 1 band in the thermal infrared spectral region (see Appendix A). The digital values of each pixel are converted first to spectral radiance at the top of the atmosphere by using a radiometric calibration procedure (Markham and Barker, 1987). The broad band planetary albedo at the top of the atmosphere r_p is calculated with a weighing scheme of the six visible and near-infrared bands (TM 1,2,3,4,5 and 7) and spectral radiation incident at the top of the atmosphere. The broad band planetary albedo r_p is related to the broad band surface albedo r_0 through a simple linear relationship (e.g. Zhong and Li, 1988):

$$r_0 = \frac{r_p - r_a}{\tau_{sw}''} \quad (4.1)$$

where r_a (-) is the lowest planetary albedo of all pixels (i.e. r_p^{min}), being usually an area with a small negligible surface albedo and τ_{sw}'' (-) is the two-way transmittance for broad band solar radiation (0.3 to 3.0 μm). This simple atmospheric correction for broad band short wave radiation takes into account the atmospheric transmittance and the path radiance (see also Koepke et al., 1985). Choudhury (1991) and Pinty and Ramond (1987) report a relative error of 10% using simple corrections like Eq. 4.1. The correction is valid for an albedo range from 0.05 to 0.43, as reported by Menenti et al. (1989a). In this case study, the two-way-transmittance was estimated by taking the surface albedo of Lake Naivasha to be $r_0 = 0.06$. This is the generally accepted value for albedo for shallow water bodies (de Bruin and Keijman, 1979) and is also confirmed by our own field measurements conducted over Lake Naivasha (see Fig. 4.6b). This yields a calibration of $\tau_{sw}'' = 0.35$ at $r_a = 0.01$.

The thermal channel, TM_6 , measures the spectrally emitted radiance between 10.6 to 12.4 μm at the top of the atmosphere, L_6^{TOA} , which can be interpreted from the raw digital numbers (DN_6) in band 6 (Clark, 1986):

$$L_6^{TOA} = \{0.1238 + (1.560 - 0.1238) * DN_6/255\} * \pi * B * 10 \quad (4.2)$$

where B (μm) is the band width of the thermal channel ($12.4-10.6 = 1.8 \mu\text{m}$) and DN_6 is the digital number of TM band 6. The spectral radiances at the top of the atmosphere measured by the satellite are related to the spectrally emitted radiances at the land surface L_6^{surf} (e.g. Schmugge et al., 1998):

$$L_6^{TOA} = L_6^{surf} \tau_6 + L_6^{atm} \quad (4.3)$$

where L_6^{atm} is the long wave radiation emitted from the atmosphere upwards (i.e. thermal path radiance) and τ_6 (-) is the atmospheric transmittance in the region $\lambda = 10.6$ to $12.4 \mu\text{m}$. Usually, L_6^{atm} and τ_6 are determined by atmospheric radiation transfer models (e.g. Tanre et al., 1990) or from a limited number of T_0 field measurements acquired at the same moment of the satellite overpass. Since these instantaneous field measurements were not available for the Lake Naivasha area, a trial and error procedure has been applied (Ashfaq, personal communication). The spectral radiances at surface level were after atmospheric correction converted into radiometric surface temperature through the inversion of Planck's law:

$$T_0 = \frac{14388}{11.5 \ln \left[\left(\frac{\epsilon_0 B * 3.7427 * 10^8}{L_6^{surf} * 11.5^5} \right) + 1 \right]} \quad (4.4)$$

where ϵ_0 (-) is the thermal infrared surface emissivity in the spectral range of TM band 6 and T_0 (K) is the radiometric surface temperature corrected for gray body effects. Results indicate that T_0 ranges at pixel scale from 22.2°C to 44.0°C . For Lake Naivasha, an average value of 24.8°C was obtained. The day time water temperature of Lake Naivasha in the month of January is known to vary between 22 and 26°C (Donia, 1998) and the T_0 values seem to therefore to be reasonable.

The thermal infrared surface emissivity ϵ_0 is estimated on the basis of NDVI (van de Griend and Owe, 1993):

$$\varepsilon_0 = 1.009 + 0.047 \ln (\text{NDVI}) \quad (4.5)$$

A theoretical justification of the relationship between ε_0 and NDVI is given by Valor and Caselles, (1996). They report an error of 0.6% in estimating ε_0 from Eq.4.5 for mid-latitudes and tropical regions. The relationship between ε_0 and NDVI is valid for the NDVI values in the range 0.16 to 0.74. This equation is hence not valid for water bodies with a negative NDVI. Therefore, the water bodies were masked and forced with $\varepsilon_0 = 1.0$. The NDVI can give information on vegetation density, color of the surface and cultivation practices. This is due to the property of chlorophyll, which strongly absorbs radiation in the red parts of the electromagnetic spectrum and reflects it in the near-infrared part (Tucker, 1979). It is determined as follows;

$$\text{NDVI} = \frac{r_p(4) - r_p(3)}{r_p(4) + r_p(3)} \quad (4.6)$$

where $r_p(4)$ and $r_p(3)$ are the spectral planetary reflectances for TM bands 4 and 3 respectively.

4.3 Hydrological delineation of the Kenyan central rift valley

Segmentation of landscapes is traditionally done by using land use/land cover maps, topographic maps, soil maps etc. The purpose of partial area hydrology is to handle the large amount of hydrological variability in watersheds with a few units. Hydrological units simplify the characterization of a watershed into a small finite number of sub-areas having less internal variability, but together describe the overall hydrological response to rainfall and irrigation. Through mass conservation, E is indirectly related to rainfall, runoff, irrigation and groundwater movement. Past studies have shown that a scatter plot of T_0 versus NDVI reflects spatial variations in fractional vegetation cover v_c , soil water content θ and surface resistance to evaporation r_s (e.g. Nemani and Running, 1989). The T_0 (r_0) relationship has also been proven to be valuable for determining dry and wet land surface types (Menenti et al., 1989b).

Figure 4.2 shows the relationships between T_0 , NDVI and r_0 , reflecting different land wetness conditions and vegetation cover. The NDVI, r_0 and T_0 values of all the pixels in the image are plotted in a three-dimensional space given by the X-Y-Z axis. First, a regularly spaced array of Z (T_0) values from the irregularly spaced X-Y-Z data is produced by interpolation methods. Next, a surface is fitted to the regularly spaced T_0 values by a least squares fit approach. Qualitative interpretation of the hydrological and vegetation status of sub-areas can be made: low T_0 , low NDVI and low r_0 indicate bare wet soils, whereas high T_0 , low NDVI and high r_0 represent the warm dry bare soil pockets. Low T_0 , high NDVI and low r_0 indicate healthy vegetation in good condition with unstressed transpiration, whereas high T_0 , high NDVI and high r_0 point to vegetation under water stress. As T_0 , NDVI and r_0 can, according to Eqs. 4.1 to 4.6, be retrieved from Landsat TM, and they reveal hydrological conditions, the watershed can be delineated from T_0 , r_0 and NDVI.

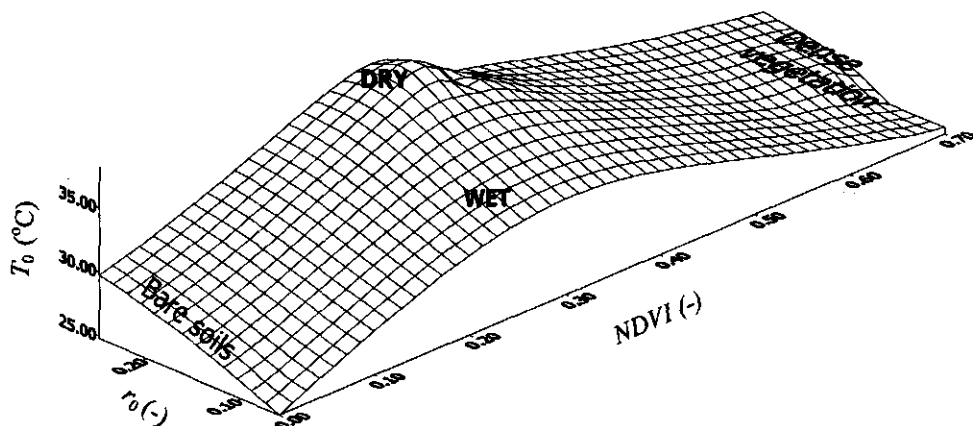


Figure 4.2: The relationship between surface temperature T_0 , NDVI and surface albedo r_0 reflecting the different land wetness conditions and vegetation cover

A cluster analysis based on T_0 , NDVI and r_0 was therefore performed which divided the study area into 15 clusters (Fig. 4.3). There are about 50,000 pixels in the 19km x 25km study area. Clustering was done to reduce this large number of pixels and group them into 15 units. This number of units was chosen from prior knowledge of the area

in which 15 different land use and land cover types were identified from ground survey and aerial photography (Hamududu, 1998). The clustering algorithm groups the pixels on basis of their statistical properties. A generalized form of the Heckbert quantization algorithm (Heckbert, 1982) is used. First, a multidimensional histogram of T_0 , r_0 and NDVI pixel values is created. This multidimensional space of “cloud of points” is divided into the 15 clusters. The algorithm starts with the whole space as one cluster and finds the axis with the largest variations in pixel values. The cluster is divided into two along the calculated axis. Similarly, the new clusters are further divided until the desired 15 clusters are achieved.

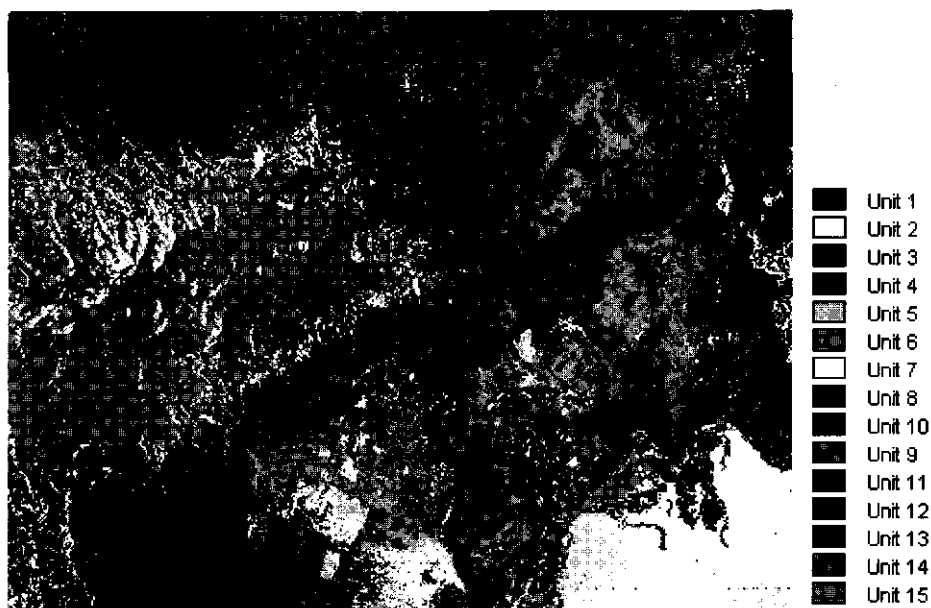


Fig.4.3: Hydrological delineation of a 19 km by 25 km area of Lake Naivasha watershed into 15 hydrological units (see color version in Appendix B).

The T_0 , NDVI and r_0 values for the clusters discerned are presented in Table 4.2. The 15 units represent areas with different wetness conditions, not variations in land use/land cover per se. The wettest and driest units are units 2 and 14 respectively. Unit 2 represents open water ($T_0 = 24.8^\circ\text{C}$; NDVI = -0.3; $r_0 = 0.06$), while unit 14 consists of sparse vegetation and bare land, and has a high radiometric surface temperature, implying that E is minimum ($T_0 = 36.7^\circ\text{C}$; NDVI = 0.37; $r_0 =$

0.25). These areas correspond to rock out-crops and bare lava flows identified on topographic maps of the area. Between these two hydrological extremes are the forested Eburu hills in the western part of the watershed and also swamp and river embankment vegetation (units 6, 9 and 15). Hydrological unit 9 must transpire more than units 6 and 15 due to the lower T_0 and higher NDVI value. This can be concluded even without having access to ground data. The irrigated areas are found in the direct vicinity of Lake Navaisha (unit 3) and they may comprise several horticultural activities. The drier areas with low vegetation cover are represented by rangelands with high T_0 , low NDVI and high r_0 . These units 4, 5 and 7 are found in the central parts of the study area, being part of the natural ecosystems.

Table 4.2: Values of radiometric surface temperature T_0 , Normalized Difference Vegetation Index $NDVI$ and surface albedo r_0 for the 15 hydrological units

Hydrological unit	% area	T_0 (°C)	$NDVI$ (-)	r_0 (-)
1	7.81	33.9	0.40	0.19
2	22.20	24.8	-0.30	0.06
3	1.40	26.6	0.66	0.12
4	1.05	38.1	0.30	0.20
5	12.85	38.4	0.29	0.22
6	2.36	28.0	0.59	0.14
7	9.75	37.3	0.32	0.21
8	3.84	35.8	0.35	0.21
9	1.34	25.3	0.70	0.12
10	6.20	35.5	0.33	0.20
11	11.45	34.1	0.37	0.25
12	4.06	36.7	0.30	0.18
13	6.17	36.4	0.34	0.19
14	8.84	36.7	0.37	0.25
15	0.68	28.0	0.67	0.15
Total	100.0			

4.4 Estimation of SVAT parameters and surface fluxes

Net available energy (R_n , G_0)

Under non-advective conditions and neglecting heat storage in canopies, surface fluxes have to satisfy the preservation of energy:

$$R_n + G_0 + H + \lambda E = 0 \quad (4.7)$$

where R_n is the net radiation, G_0 the soil heat flux, H the sensible heat flux and λE the latent heat flux required for evaporation. The energy balance equation can be further decomposed into its constituent parameters. Net radiation is calculated as the sum of incoming and outgoing short wave and long wave radiation components:

$$R_n = (1 - r_0) K^\downarrow + \varepsilon' \sigma T_a^4 - \varepsilon_0 \sigma T_0^4 - (1 - \varepsilon_0) \varepsilon' \sigma T_a^4 \quad (4.8)$$

where K^\downarrow (W m^{-2}) is the incoming short wave solar radiation, $\varepsilon' \sigma T_a^4$ (W m^{-2}) is the incoming long wave radiation emitted by the atmosphere, with ε' (-) being the apparent emissivity of the atmosphere, σ ($\text{W m}^{-2} \text{K}^{-4}$) is the Stefan Boltzmann constant, and $\varepsilon_0 \sigma T_0^4$ (W m^{-2}) is the outgoing long wave radiation emitted by the surface. K^\downarrow is determined on the basis of standard astronomical equations (e.g. Iqbal, 1983) which leads to an instantaneous value of 1180 W m^{-2} incident to the top of the atmosphere at the center of the watershed during Landsat overpass at 9.45 hrs. From Eq. 4.1, a value for the two-way transmittance of $\tau_{sw}'' = 0.35$ was obtained, which implies that the single-way transmittance is $\tau_{sw} = 0.59$. Hence, a portion of $1180 \times 0.59 = 696 \text{ W m}^{-2}$, after atmospheric absorption, scatter and transfer, will reach the land surface. A small, relatively flat area of $19\text{km} \times 25\text{km}$ was studied, hence the effect of topography on the radiation balance was not considered. The apparent emissivity of the atmosphere, $\varepsilon' = 0.91$, is obtained from empirical relationship between ε' and T_a (Brutsaert, 1975). Incoming long wave radiation is estimated by using T_a and the apparent emissivity of the atmosphere yielding a value of $\varepsilon' \sigma T_a^4 = L^\downarrow = 407 \text{ W m}^{-2}$. The screen height T_a during satellite overpass was $T_a = 24.8^\circ\text{C}$ being tentatively estimated from T_0 of Lake Naivasha ($T_0 = 24.8^\circ\text{C}$, unit 2 see Table 4.2) assuming that $T_a \approx T_0$ above water. A similar condition for wet surface E was observed by Prihodko and Goward (1997), who concluded that the surface temperature of an infinitely thick vegetation canopy is

close to ambient T_a . The outgoing long wave radiation is derived from T_0 and ϵ_0 and varies for each hydrological unit.

The soil heat flux G_0 cannot be determined from satellite spectral measurements. However, previous studies have shown that the G_0/R_n fraction can be estimated from NDVI (Daughtry et al., 1990), T_0 (Menenti, 1984) or a combination of NDVI, T_0 and r_0 (Bastiaanssen and Roebeling, 1993). Daughtry et al. (1990) obtained an absolute relative error of 13% between measured G_0 and estimated G_0 using the NDVI relationship. They observe that this is better than estimating G_0 simply as 10 or 20% of R_n in which case absolute relative errors of 58 and 25% respectively occurred. The following expression was used for the relationship between G_0 and R_n , validated for the HAPEX experiments in Spain and Niger (Bastiaanssen et al, 1998a):

$$\frac{G_0}{R_n} = \frac{T_0^c}{r_0} (0.0032 r_{0,avg} + 0.0062 r_{0,avg}^2) (1 - 0.978 NDVI^4) \quad (4.9)$$

where T_0^c ($^{\circ}\text{C}$) is the instantaneous radiometric surface temperature expressed in degrees centigrade and $r_{0,avg}$ (-) is the average value of r_0 during daylight hours when heat is stored in the top soil. For Landsat overpass in mid-morning, $r_{0,avg}$ can be estimated as $1.1r_0$ (Menenti et al, 1989a).

Table 4.3 shows the resulting R_n and G_0 values for the 15 hydrological units discerned. Unit 2 (open water) seems to have 608 W m^{-2} available energy ($R_n - G_0$) for sensible and latent heat fluxes whereas unit 5 with 355 W m^{-2} absorbs significantly less energy due to high reflected ($K\uparrow = 153 \text{ W m}^{-2}$) and emitted radiation ($L\uparrow = 508 \text{ W m}^{-2}$). These distinct spatial variations in $R_n - G_0$ will affect the SVAT parameters, surface energy balance and related hydrological processes.

Table 4.3: Estimation of instantaneous radiation balance and net available energy
 $R_n - G_0$

Hydrological unit	$K\downarrow$ W m^{-2}	$K\uparrow$ W m^{-2}	$L\downarrow$ W m^{-2}	$L\uparrow$ W m^{-2}	R_n W m^{-2}	ϵ_0 -	G_0 W m^{-2}	$R_n - G_0$ W m^{-2}
1	696	132	407	487	484	0.966	79	405
2	696	42	407	448	614	1.000	6	608
3	696	84	407	453	566	0.989	55	511
4	696	139	407	507	457	0.952	87	370
5	696	153	407	508	442	0.951	87	355
6	696	97	407	460	546	0.984	62	484
7	696	146	407	504	453	0.955	85	368
8	696	146	407	495	462	0.960	82	380
9	696	84	407	446	573	0.992	50	523
10	696	139	407	493	471	0.957	83	388
11	696	174	407	487	442	0.962	80	362
12	696	125	407	498	480	0.952	85	395
13	696	132	407	500	471	0.958	84	387
14	696	174	407	503	426	0.962	82	344
15	696	104	407	463	536	0.990	57	479

Partitioning of available energy into sensible and latent heat fluxes (H , λE)

The sensible heat flux, H , is classically expressed as:

$$H = \frac{\rho_a c_p}{r_{ah}} \Delta T_a \quad (4.10)$$

where ρ_a (kg m^{-3}) is the moist air density, c_p ($\text{J kg}^{-1} \text{K}^{-1}$) is the air specific heat at constant pressure, r_{ah} (s m^{-1}) is the aerodynamic resistance to heat transport and ΔT_a is the temperature difference between layers z_1 and z_2 (see Eq. 2.44). Figure 2.2 depicts the logarithmic temperature profile between a particular land surface type and the lower part of the atmospheric boundary layer. The sensible heat flux H of

Eq. 4.10 applies to the region between the lower (z_1) and upper (z_2) integration limits for the eddy diffusivity for heat transport, K_h :

$$r_{ah} = \int_{z_1}^{z_2} \frac{1}{K_h} dz = \left(\frac{1}{ku_*} \ln\left(\frac{z_2}{z_1}\right) - \psi_h\left(\frac{z_2}{L}\right) \right) \quad (4.11)$$

where u_* (m s^{-1}) is the friction velocity, k (-) is von Karman's constant and ψ_h (-) is the stability correction of the temperature profile due to buoyancy (Brutsaert, 1982). Most often, the surface roughness for heat transport, z_{0h} , is taken as the lower integration limit to comply with the aerodynamic surface temperature, $T_{z_{0h}}$. The major obstacle in practically using thermal infrared images for the estimation of sensible heat flux from radiometric surface temperatures T_0 , is that $T_0 \neq T_{z_{0h}}$ (Carlson et al., 1995). Figure 2.1 shows that the quantification of z_1 modifies r_{ah} , ΔT_a and, following Eq. 4.10, also H . Most thermal infrared studies are based on the hypothesis that $T_0 = T_{z_{0h}}$ and z_{0h} is adjusted to match H (Kalma and Jupp, 1990; Lhomme et al., 1994). This can only be done if *in situ* measurements of H are available, which is not a straightforward situation. Although this solution gives satisfactory results for specific land cover classes for which z_{0h} can be calibrated, it does not permit applications of the calibrated z_{0h} values to other hydrological units with varying vegetation heights and bio-physical conditions. Hence, an alternative solution has been worked out to apply Eqs. 4.10 and 4.11 in composite terrain. Bastiaanssen et al. (1998b) suggested to basically assume $T_{z_{0h}} \neq T_0$ and take an arbitrary value of z_1 . The temperature difference ΔT_a between z_2 and z_1 can then be established from r_{ah} and H without the involvement of T_0 or T_a :

$$\Delta T_a = \frac{Hr_{ah}}{\rho_a c_p} \quad (4.12)$$

Eq. 4.12 is more a matching of H by calibrating ΔT_a rather than by adjusting z_{0h} . This, at the same time, evades the necessity to have accurate and instantaneous T_a data from all over the watershed. It also eliminates problems induced by improper quantification of T_0 from remote sensing data by using Eq. 4.3. Figure 2.1 shows that ΔT_a can be theoretically calculated for any height z_1 , however, a small value for z_1 ($z_1 \approx z_{0h}$) is preferred in order to comply better with the theory of thermodynamics. As *in situ* H fluxes for the Navaisha catchment were not available,

H is estimated from the spatial variation of energy partitioning in the watershed. The solution of the sensible heat flux can be made by approximating water bodies to have a negligible sensible heat flux ($H \approx 0$; $R_n \approx G_0 + \lambda E$). Experimental evidence that $H \approx 0 \text{ W m}^{-2}$ for water bodies was obtained, for instance, by de Bruin and Keijman (1979) for a 460 km^2 inland lake of 3 m depth and by Ashfaq, (1999) for Lake Naivasha. On the other hand, extremely dry areas can be approximated to have a zero latent heat flux ($\lambda E \approx 0$; $H \approx R_n - G_0$). The T_0 (r_0) relationship (see Fig. 4.4) is used to correctly identify the wettest and driest units. The wettest areas have the lowest T_0 and r_0 whereas the driest have the highest r_0 and high T_0 . Units 2 and 14 were identified as the wettest and driest units respectively. The above described arguments can be used to estimate the energy balance of unit 2 as $R_n = 614 \text{ W m}^{-2}$, $G_0 = 6 \text{ W m}^{-2}$, $H = 0$, $\lambda E = 608 \text{ W m}^{-2}$ and $\Delta T_a = 0 \text{ K}$. Unit 14 is characterized by a surface energy balance of $R_n = 426 \text{ W m}^{-2}$, $G_0 = 82 \text{ W m}^{-2}$, $H = 344 \text{ W m}^{-2}$ and $\lambda E = 0 \text{ W m}^{-2}$. These two extremes in sensible heat flux are used to solve ΔT_a in Eq. 4.12 if r_{ah} is known. This means that thermal infra red data are not used for estimating the thermal gradient.

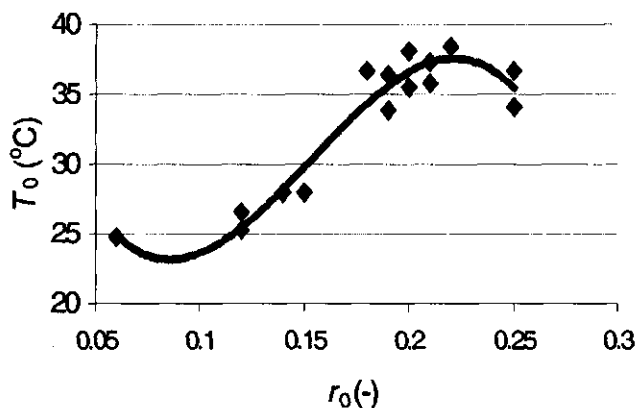


Fig.4.4. The relationship between surface temperature T_0 and surface albedo r_0 which is used to select the wet and dry units

Two turbulent structure parameters are essential for the computation of r_{ah} ; friction velocity u_* and the Monin Obukhov length, L . Menenti et al. (1989b) published first indications that r_{ah} can be obtained from the slope between remotely sensed r_0 and T_0 . Bastiaanssen et al. (1998b), describe an iterative procedure to determine u_* and

L , together with an estimate of z_{0h} , from the negative slope between T_0 and r_0 . Following Moran and Jackson (1991), the surface roughness for momentum transport z_{0m} , can be estimated from NDVI. In this study, estimates of z_{0m} were made on the basis of experimental findings in Niger (Taylor et al., 1997). The values of z_{0h} were taken as a factor 10 lower ($kB^{-1} = 2.3$), which opened the opportunity to estimate z_{0h} for each hydrological unit (see Table 4.4). The results of the iterative procedure indicate an area-effective friction velocity, u_*^{eff} , of 0.341 m s^{-1} . This value was converted into area-effective wind speed at 100 m height by considering an area-effective roughness length z_{0m}^{eff} and u_*^{eff} and using the flux-profile relationship for momentum transfer (Brutsaert, 1982). This gave a value of $u_{100} = 3.9 \text{ m s}^{-1}$. Local u_* values could thereafter be derived using hydrological unit-wise z_{0h} and stability conditions ψ_h .

The near-surface vertical T_a can be solved for unit 14 as $\Delta T_a = 12.1 \text{ K}$ after having determined $r_{ah} = 40.2 \text{ s m}^{-1}$ and $H = 344 \text{ W m}^{-2}$. Note that ΔT_a is obtained from Eq. 4.12 and not deduced from $T_0 - T_a$. It is further known that low ΔT_a values coincide with low thermal emission ($T_0 = 24.8 \text{ }^\circ\text{C}$) and that a high value of ΔT_a coincides with high thermal emission ($T_0 = 36.7 \text{ }^\circ\text{C}$). A function between radiometric surface temperature T_0 and ΔT_a was therefore established. Experimental work in HEIFE-China (Wang et al., 1995), FIFE-USA (Franks and Beven, 1997), HAPEX-Niger (Troufleau et al., 1997) and Egypt (Bastiaanssen et al., 1998b) has indicated that the radiometric surface temperature is a linear function of ΔT_a . This relationship is the same for both land and water surfaces and applies to the space domain only and not to time. The relationship is therefore valid only for the time of satellite image acquisition and for a given region with a specific solar radiation and wind speed. For this study, ΔT_a has been computed for each hydrological unit using the self-calibration of units 2 ($T_0 = 24.8$; $\Delta T_a = 0 \text{ }^\circ\text{C}$) and 14 ($T_0 = 36.7$; $\Delta T_a = 12.1 \text{ }^\circ\text{C}$):

$$\Delta T_a = 1.02 T_0 - 25.3 \quad (4.13)$$

where T_0 ($^\circ\text{C}$) is expressed in degrees centigrade. The iterative procedure for u_* , L , ψ_h , r_{ah} and H was applied to each hydrological unit separately, leading to the r_{ah} and H values presented in Table 4.4.

The transport equation for latent heat flux is given generally by:

$$\lambda E = \frac{\rho_a c_p (e_0^* - e_2)}{\gamma(r_{av} + r_s)} \quad (4.14)$$

where e_0^* (hPa) is the saturated vapor pressure at surface temperature T_0 (inside stomata or soil cavities or at water-air interface for open water bodies), e_2 (hPa) is the actual vapor pressure at screen height, γ (hPa K⁻¹) is the psychrometric constant, r_{av} (s m⁻¹) is the aerodynamic resistance to water vapour transport and r_s (s m⁻¹) is the bulk surface resistance to E . The surface resistance r_s , controls λE and hence the partitioning between H and λE . Unfortunately, r_s is difficult to quantify and varies besides soil moisture with solar radiation, vapour pressure deficit and T_a (Jarvis, 1976; Stewart 1988). Since r_s is difficult to model, it is easier to express λE as a residual of the surface energy balance residual than to calculate it according to Eq. 4.14:

$$\lambda E = R_n - G_0 - H \quad (4.15)$$

From Table 4.4, it can be seen that unit 9 (forest) consumes more water ($\lambda E = 482$ W m⁻²) than unit 3 ($\lambda E = 389$ W m⁻²) due to the difference in the available energy $R_n - G_0$. Unit 15 evaporates 50% less than open water E from Lake Navaisha ($\lambda E = 237$ W m⁻²). Unit 5 indicates a strongly reduced E ($\lambda E = 36$ W m⁻²). To verify the physical consistency of the generally accepted micro-meteorological Eq. 4.15, the surface resistance was obtained by the inversion of Eq. 4.14 after having determined λE from Eq. 4.15 and assuming that $r_{ah} = r_{av}$. The saturated vapour pressure was computed as:

$$e_0^*(T_0) = 6.11 \exp \left(\frac{17.17 T_0}{T_0 + 273.3} \right) \quad (4.16)$$

The actual vapour pressure was set at $e_2 = 10$ hPa and obtained from unit 2, taking $\lambda E = 554$ W m⁻², $r_{av} = 65.5$ s m⁻¹, $e_0^* = 31.3$ hPa and $r_s = 0$ s m⁻¹. The lowest surface resistance next to open water with $r_s = 0$ s m⁻¹, is unit 9 with $r_s = 64$ s m⁻¹ followed

by unit 3 with $r_s = 91 \text{ s m}^{-1}$ (see Table 4.4). Resistances of this magnitude reveal that forest and irrigated crops are transpiring at potential level. The Food and Agricultural Organization (FAO) has defined $r_s = 70 \text{ s m}^{-1}$ as the resistance for an unstressed grass field (Allen et al., 1998) which is in agreement with the values obtained. Dolman (1993) gave values for tropical forests in the range of minimally $r_s = 50 \text{ s m}^{-1}$. Taylor et al. (1997) gave a minimum resistance for dense bush land of 80 s m^{-1} . This shows that the estimations of the heat fluxes are in agreement with expectations.

The evaporative fraction Λ was calculated from λE , R_n and G_0 :

$$\Lambda = \frac{\lambda E}{R_n - G_0} \quad (4.17)$$

Table 4.4: Estimation of instantaneous SVAT parameters and heat fluxes for the 15 Hydrological units

unit	z_{0h} m	u^* m s^{-1}	L m	ψ_h -	ΔT_a K	r_{ah} s m^{-1}	r_s s m^{-1}	H W m^{-2}	LE W m^{-2}	Λ -
1	0.0055	0.36	-14.8	1.1	9.3	38.4	518	274	131	0.32
2	0.0031	0.27	∞	0.0	0.0	65.8	0	0	608	1.00
3	0.0500	0.63	-176.7	0.2	1.8	17.0	91	122	389	0.76
4	0.0024	0.31	-8.3	1.5	13.6	48.2	1840	319	51	0.14
5	0.0021	0.31	-7.9	1.5	13.9	49.4	2646	318	36	0.10
6	0.0276	0.52	-73	0.4	3.3	22.5	125	164	320	0.66
7	0.0028	0.32	-9.2	1.4	12.8	46.1	1637	314	54	0.15
8	0.0036	0.33	-11.2	1.3	11.0	43.4	848	288	91	0.24
9	0.0705	0.72	-784.5	0.0	0.5	14.2	64	40	482	0.92
10	0.0030	0.32	-10.8	1.3	10.9	46.1	631	268	120	0.31
11	0.0043	0.34	-13.5	1.2	9.5	42.0	652	256	106	0.29
12	0.0024	0.31	-9.2	1.4	12.1	49.2	714	280	115	0.29
13	0.0033	0.33	-10.3	1.4	11.8	44.2	985	304	84	0.22
14	0.0043	0.35	-10.8	1.3	12.1	40.2	∞	343	0	0.00
15	0.0546	0.68	-108.7	0.3	3.3	15.2	184	243	237	0.49

The evaporative fraction Λ is a fairly constant indicator of the energy partitioning during day light hours and can be used to temporally integrate the energy balance from instantaneous values to 24-hour values. Studies by Sugita and Brutsaert (1990) and Crago (1996b), among others, have extensively indicated that the fraction as defined in Eq. 4.17 is temporally constant. Because of forcing unit 2 with $H = 0$ and unit 14 with $\lambda E = 0$, the evaporative fraction varies between 0 and 1 (see Table 4.4). The 24-hour actual λE is computed according to the net radiation in 24 hours R_{n24} and Λ using:

$$\lambda E_{24} = \Lambda R_{n24} \quad (4.18)$$

R_{n24} is obtained as follows:

$$R_{n24} = (1 - r_0^{avg}) K\downarrow_{24} + L^*_{24} \quad (4.19)$$

where $K\downarrow_{24}$ is the solar radiation integrated over 24 hours, calculated from the solar hour angle and the sun zenith angle at the time of over pass of the satellite (Iqbal, 1983). L^*_{24} is the net longwave radiation for 24 hours and is calculated by the semi-empirical function presented by Allen et al., (1998). The results of Eq.4.18 are presented in Table 4.5 and displayed in Fig. 4.5. The estimated lake E on January 21 is 6.5 mm d^{-1} . Unit 9(forest) has 5.5 mm d^{-1} , while units 3 (cropland) and 4 and 7 (grasslands/rangelands) have an E of 4.5 mm d^{-1} and 0.7 mm d^{-1} respectively. The reference E for grass computed with the Penman-Monteith equation as precisely described in Allen et al. (1998), gives 5.8 mm d^{-1} . This reference E of unstressed grass compares with the actual E of unit 9 (5.5 mm d^{-1}) and is more than unit 3 (4.5 mm d^{-1}).

4.5 Validation

The validation of remote sensing determined surface parameters and fluxes is a difficult task. In the ideal situation, fluxes should be measured simultaneously in all the hydrological units at the time of overpass of the satellite. However, this is usually not possible due to the limited the technical and financial resources available for obtaining field data from a heterogeneous landscape. Furthermore, the fluxes obtained from ground measurements are limited in areal extent and are

Table 4.5: The estimated 24-hour time integrated estimated evaporation E_{24} for the 15 hydrological units

Hydrological unit	λ	R_{n24} W m^{-2}	E_{24} mm d^{-1}
1	0.32	149	1.7
2	1.00	184	6.5
3	0.76	168	4.5
4	0.14	146	0.7
5	0.10	141	0.5
6	0.66	163	3.8
7	0.15	144	0.7
8	0.24	144	1.2
9	0.92	168	5.5
10	0.31	147	1.6
11	0.29	133	1.4
12	0.29	152	1.6
13	0.22	149	1.2
14	0.00	133	0.0
15	0.49	160	2.8

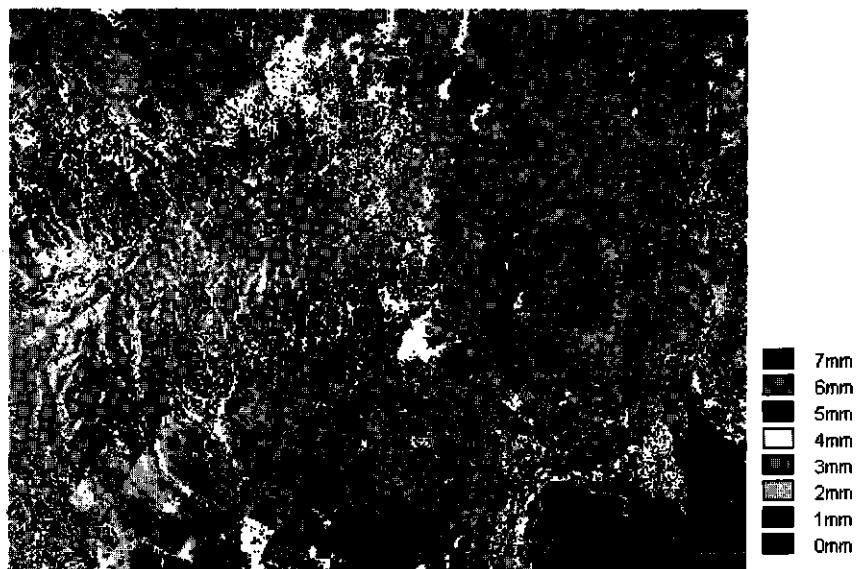


Fig. 4.5: Spatial patterns of actual evaporation of a 19 km by 25 km area of Lake Naivasha watershed on 21 January 1995 (see color version in Appendix B)

representative of a relatively small area, compared with those obtained from remote sensing algorithms. Hence validation of regional scale E is not straightforward.

Field data obtained from two field campaigns conducted in October, 1998 and January, 1999 were used for validation. Data from a meteorological station were also available for the period 1961-1968. During October 1998, T_a , air humidity RH and wind velocity u were measured at two levels. Incoming and outgoing radiation were measured separately. In January, 1999, T_a and RH at 3 levels (0.1 m, 2 m and 3 m), rainfall and incoming solar radiation were measured at 20-minute intervals by an automatic weather station placed in a dry grassland area 5 km west of Lake Naivasha.

Table 4.6 shows T_a at 2 m height, shortwave atmospheric transmittance and evaporative fraction at 9.40 hrs local time from 18 to 31 January 1999 determined from the field measurements. Daily E from the grassland site and from open water (Lake Naivasha) was also computed from the field data. The Bowen ratio energy balance method was used to calculate E from the two sites. Table 4.6 also shows the results from remote sensing for comparison. The automatic weather station in the grassland site was located in unit 7. The average field measured A and E were 0.23 and 0.61 mm d⁻¹ respectively. This compares well with the values of 0.21 and 0.70 mm d⁻¹ obtained from remote sensing. For open water E , an average value of 6.3 mm d⁻¹ was obtained from field measurement as opposed to 6.5 mm d⁻¹ from remote sensing. The two sites selected for validation represent the two extremes of wetness conditions. It is therefore expected that the results from the other hydrological units are also in the correct range. At 9.40 hrs, when Landsat satellite passes over, there was little variation of τ during the fourteen days of observations. The highest was 0.62 and the lowest 0.58, with an average of 0.60. It is evident that the value of 0.59 obtained from the simple expression used to estimate τ (Eq. 4.1) is valid. The T_a is between 22.6 and 24.7 °C, with an average of 23.4 °C. A value of 24.8 °C was used in this remote sensing study, being determined from the average surface temperature of Lake Naivasha assuming zero heat flux and this also seems reasonable.

Table 4.7 shows daily solar radiation, daily atmospheric transmissivity and E (open water) extracted for the month of January of records(1961-1968) from the Kedong meteorological station situated in the study area. The mean value of lake E from the long term data is 6.4 mm d^{-1} . This reveals that lake E depicted in Table 4.5 is reliable. Figures 4.6a, b, and c show graphs of T_0 and T_a , r_0 and surface fluxes against time measured over Lake Naivasha on 8 October 1998. Figure 4.6a, supports the assumptions that T_a over moist surfaces such as water is approximately equal to the surface temperature. The average difference is 1°C , with the minimum and maximum differences being 0°C and 2.1°C respectively. Figure 4.6b indicates that r_0 is about 0.06 between 10.00 and 11.00 hrs. However, r_0 varies during the day with the lowest, 0.03, observed between 13.00 and 14.00hrs. The surface fluxes in Fig. 4.6c indicate that R_n is very close and almost equal to λE , showing that Λ is approximately equal to 1(Ashfaque,1999). Both H and G_0 over water are close to zero. This agrees with the estimations presented in Table 4.4.

Table 4.7 : Long term data of solar radiation, atmospheric transmissivity and open-water evaporation for the month of January (1961-1968)

Meteorological parameter	Minimum	Mean	Maximum
Daily solar radiation $K\downarrow (\text{Wm}^{-2})$	244	266	282
Daily transmissivity $\tau(-)$	0.58	0.64	0.67
Evaporation (open-water) $E_o (\text{mm d}^{-1})$	5.8	6.4	6.8

The validation of results from similar studies in Egypt, Spain, China and Niger (Bastiaanssen et al., 1998a; Wang et al., 1998; Kustas et al., 1994), which had extensive data from large scale field experiments, indicate that reliable estimates of E can be obtained from remotely sensed data. Root mean square error (RMSE) of between 0.05 to 0.14 are reported for Λ , while differences between ground based measurements and estimated E from remote sensing are between 5% and 20%. Sensitivity analysis indicated that a 25% change in the parameters caused less than 20% change in the fluxes and Λ . $K\downarrow$, r_0 and T_0 were the most sensitive parameters in estimating the fluxes.

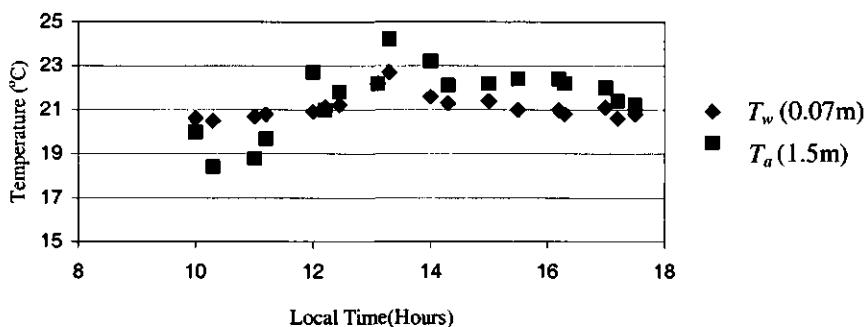


Fig.4.6a: Diurnal variations of surface temperature T_w (diamonds) and air temperature T_a (squares) above lake Naivasha on 9 October 98

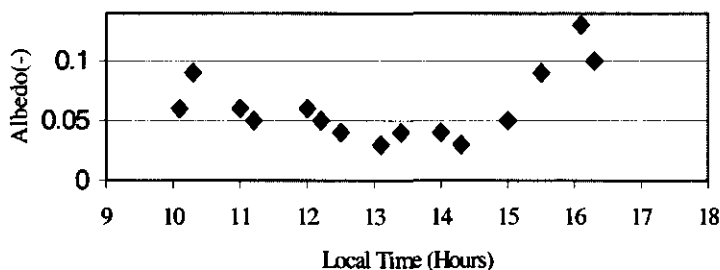


Fig.4.6b: Diurnal course of surface albedo r_0 over Lake Naivasha on 9 October 98

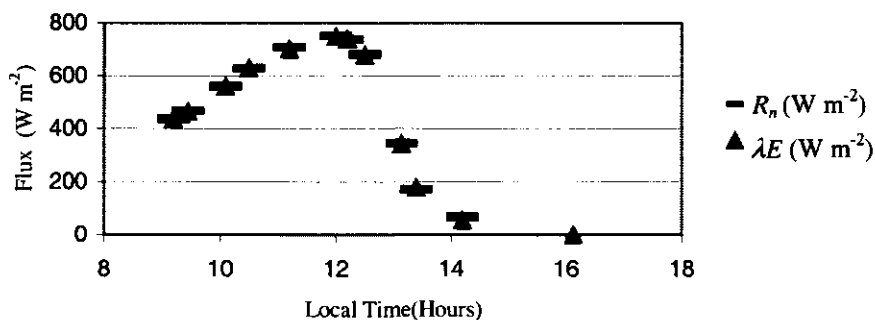


Fig. 4.6c: Latent heat flux λE (triangles) and net radiation R_n (lines) over Lake Naivasha on 9 October 98

4.6 Aggregation of SVAT parameter and fluxes

Aggregation rules of SVAT parameters have been used to calculate the area-representative SVAT parameters for the Navaisha watershed. Aggregated parameters are usually applied as input in land surface parameterization schemes for the simulation of large-scale energy balances and exchange processes between land and atmosphere (e.g. Noilhan et al., 1997). In this study, however, area-representative parameters will be employed to analyze the effect of spatial variations of the SVAT parameters on E . A comparison will be made between fluxes of each hydrological unit calculated from local SVAT parameters vis-a-vis fluxes obtained using area-aggregated SVAT parameters.

Many different aggregation rules have been published in recent years (e.g. McNaughton, 1994; Shuttleworth et al., 1998). In the current study, r_0 , ε_0 , z_{0m} , u^* , ψ_h and ΔT_a SVAT parameters have been areally aggregated. The regionally representative surface albedo is calculated as the weighted mean of the values of the individual hydrological units, because variations in cloud cover did not exist on the cloud free image of 21 January and the area is sufficiently small and flat to allow extra-terrestrial radiation to be constant:

$$r_0^{eff} = \sum a_i r_{0i} \quad (4.20)$$

where, r_0^{eff} is the area-effective albedo and a_i and r_{0i} are the fractional area coverage and surface albedo respectively for a particular class i . Data on fractional area a_i are presented in Table 4.2. The results show $r_0^{eff} = 0.177$. The aggregated surface thermal infrared emissivity was determined from a weighing scheme, using both the fractional area a_i as well as the emitted black body radiation:

$$\varepsilon_0^{eff} = \frac{\sum a_i \varepsilon_{0i} \sigma T_{0i}^4}{\sum a_i \sigma T_{0i}^4} \quad (4.21)$$

Following Wang et al. (1998), Eq. 4.21 assigns more weight to the areas having a higher thermal radiation. The results show $\varepsilon_0^{eff} = 0.968$. Regional surface temperature is determined by using area-effective emissivity obtained from Eq. 4.21 and up-welling radiation:

$$T_0^{eff} = \left[\frac{\sum a_i \varepsilon_{0i} \sigma T_{0i}^4}{\varepsilon_0^{eff} \sigma} \right]^{0.25} \quad (4.22)$$

The results show $T_0^{eff} = 33.2^\circ\text{C}$. The surface roughness length for heat transport was aggregated according to the procedure Mason (1988) developed for the aggregation of the surface roughness length for momentum transport:

$$\frac{1}{\left[\ln \left(\frac{z_B}{z_{0h}^{eff}} \right) \right]^2} = \sum \frac{a_i}{\left[\ln \left(\frac{z_B}{z_{0hi}} \right) \right]^2} \quad (4.23)$$

The above expression is based on the idea that the factor $[\ln (z_B / z_{0h})]^2$ is linearly related to friction velocity and that the area-representative sensible heat flux appears at some height above the land surface where all fluxes from individual surface elements are blended out due to turbulent mixing. This blending height, z_B , was taken as 100 m elevation. The results show $z_{0h}^{eff} = 0.0041$ m. The friction velocity u_* was aggregated according to the momentum flux weighted for fractional area a_i :

$$u_*^{eff} = \left[\frac{\sum a_i \rho_a u_{*i}^2}{\rho_a} \right]^{0.25} \quad (4.24)$$

The result shows $u_*^{eff} = 0.341 \text{ m s}^{-1}$, which agrees with u_*^{eff} obtained from the iterative procedure. This implies that the dis-aggregation/aggregation procedure for u_* is consistent. The stability correction factor ψ_h is an integral part of the aerodynamic resistance r_{ah} (see Eq. 4.11). Values for ψ_h were aggregated by using the standard expression of the Monin-Obukhov length, using u_*^{eff} , T_0^{eff} and H^{eff} :

$$L^{eff} = - \frac{\rho_a c_p (u_*^{eff})^3 T_0^{eff}}{kg H^{eff}} \quad (4.25)$$

where g (m s^{-2}) is the acceleration due to gravity and H^{eff} is the weighted average of all H_i -fluxes ($\sum a_i H_i$). The results show $\psi_h = 1.11$. The area-effective value for $\Delta T_a^{\text{eff}} = 8.5$ K was obtained from a weighted average:

$$\Delta T_a^{\text{eff}} = \sum a_i \Delta T_{a-i} \quad (4.26)$$

4.7 Parameter variability and impact on surface fluxes

Watershed average surface fluxes

A parameter variability study was performed to provide an indication of the importance of schematizing the spatial variability of SVAT parameters. First the effect on total watershed H and λE fluxes will be discussed, followed in section 7.2 by the effect on spatially distributed H and λE fluxes.

The Lake Naivasha watershed surface energy balance is calculated from the aggregated SVAT parameters using Eq. 4.8 for R_n^{eff} , Eq. 4.9 for G_0^{eff} (taking $\text{NDVI}^{\text{eff}} = 0.28$) and Eq. 4.10 for H^{eff} . The results are presented in Table 4.8. It appears that H^{eff} has a 2.3% deviation from $\sum a_i H_i$ and λE^{eff} a 4.0% deviation from $\sum a_i \lambda E_i$. These differences are within the error of estimation of the fluxes. It can therefore be concluded that the aggregation rules yield satisfactory results to assess area-effective surface fluxes. Hence, total watershed E can be satisfactorily obtained from area-aggregated SVAT parameters and there is no need to solve the E from sub-catchments explicitly. It is, however necessary to accurately describe the spatial variation of SVAT parameters and sound aggregation rules should be applied rather than arithmetic mean values of SVAT parameters. As parameter values in Table 4.4 differ considerably from the values of the aggregated SVAT parameters, it may be concluded that the incorporation of a locally measured SVAT parameters for calculating watershed fluxes can lead to erroneous results.

Table 4.8: Total watershed energy balance as a weighted average of energy balances from the 15 hydrological units and from area-aggregated SVAT parameters

Flux (W m^{-2})	Weighted average of hydrological units	Area-aggregated SVAT parameters
Net radiation R_n	497	496
Soil heat flux G_0	77	79
Sensible heat flux H	221	226
Latent heat flux λE	199	191

Watershed distributed surface fluxes

Two different treatments of the parameter domains on watershed distributed surface fluxes were tested: locally estimated SVAT parameters of Table 4.4 versus spatially constant SVAT parameters. The watershed-aggregated values of SVAT parameters were used as spatially constant over the whole watershed. The fluxes of each unit were calculated by taking each of the parameters (shown in Tables 4.9 and 4.10) alternatively as equal to the watershed aggregated parameter. The deviation of these fluxes from the fluxes calculated using distributed parameters (Table 4.4) is represented as % fractional difference:

$$\frac{Y_i(x_1, \dots, x_n) - Y_i(x^{eff}, x_1, \dots, x_{n-1})}{Y_i(x_1, \dots, x_n)} * 100 \quad (4.27)$$

where Y_i represents the sensible or latent heat flux of unit number i and x are the SVAT parameters. Tables 4.9 and 4.10 summarize how fluxes of the hydrological units vary when spatially constant SVAT parameters are considered instead of local distributed values. Generally, the units can be divided into three groups on the basis of their sensitivity. The wet units 2 and 9 are relatively less sensitive to λE but most sensitive to H . The wet units have large values for λE for example 554 W m^{-2} for unit 2. Absolute λE deviations due to changes in the SVAT parameters yield small fractional differences. The dry units 13 and 14 are very sensitive to λE but less sensitive for H estimations. The third group (e.g. units 1 and 8) are insensitive in the

Table 4.9: Percent fractional difference of the latent heat flux λE of the hydrological units due to variations of SVAT parameters

Hydrological unit	ΔT_a K	z_{oh} m	u^* $m\ s^{-1}$	ψ_h -	r_o -	ε_o -	Root-mean-square percent fractional difference
1	+19.8	+6.3	+18.1	+7.8	+5.4	+0.1	11.9
2	-26.2	0.0	0.0	0.0	-15.7	+1.4	12.5
3	-112.9	+11.1	+15.1	-6.2	-10.7	-0.7	47.0
4	-239.2	-77.3	-36.4	+55.6	+27.4	-2.3	106.7
5	+345.9	-122.2	-66.0	+80.4	+77.0	-3.6	158.8
6	-81.1	+14.0	+18.9	-6.2	-8.9	-3.6	34.8
7	+197.7	-52.6	-16.3	+46.6	+38.4	-0.3	87.3
8	+74.7	-13.8	+3.8	+19.6	+22.9	-1.5	33.4
9	-130.3	+3.3	+4.5	-2.2	-8.8	-0.6	53.4
10	+51.6	-16.6	-5.6	+14.5	+11.3	-0.9	23.5
11	+27.5	-3.3	+8.5	+10.9	+45.6	-0.6	22.5
12	+74.9	-29.6	-16.6	+19.1	0	-1.5	34.5
13	+105.5	-21.6	0.0	+25.7	+8.4	-0.9	43.3
14	+11479	-5160	+2036	+2541	+8106	-0.5	5892
15	-161.7	+37.9	+52.6	-17.7	+9.0	+221.8	115.4
Root-mean- square percent fractional difference	147.7	43.8	26.8	31.5	28.8	1.7	

Table 4.10: Percent fractional difference of the sensible heat flux H of the hydrological units due to variations of SVAT parameters

Hydrological unit	ΔT_a K	z_{0h} m	u^* m s^{-1}	ψ_h -	r_0 -	ϵ_0 -	Root-mean-square percent fractional difference
1	-9.4	-3.0	-8.6	-3.7	0.0	-0.2	5.5
2	-210100	+5.7	+20.1	+14.2	0.0	-5255	85799.8
3	+358.5	-35.1	-48.0	+19.6	0.0	+9.6	148.6
4	-38.1	+12.3	+5.8	-8.8	0.0	-1.3	16.9
5	-39.4	+13.9	+7.5	-9.2	0.0	-1.5	17.7
6	+157.7	-27.2	-36.7	+12.0	0.0	+4.1	67.2
7	-34.1	+9.1	+2.8	-8.0	0.0	-1.6	14.8
8	-23.7	+4.4	-1.2	-6.2	0.0	-0.8	10.2
9	+1560.1	-39.3	-54.4	+25.9	0.0	+32.6	637.7
10	-23.0	+7.4	+2.5	-6.5	0.0	-1.1	10.3
11	-11.4	+1.3	-3.5	-4.5	0.0	-0.6	5.2
12	-30.8	+12.1	+6.8	-7.8	0.0	-1.5	14.2
13	-29.0	+5.9	0.0	-7.1	0.0	-0.9	12.4
14	-30.8	+1.4	+5.5	-6.8	0.0	-0.5	13.1
15	+157.7	-36.9	+51.3	+17.3	0.0	+5.6	69.7
Root-mean-square fractional difference	234.2	19.3	25.7	12.1	0.0	9.3	

estimations of both H and λE because local parameter values are similar to the spatially constant values selected i.e the aggregated values. The aggregated regional values of the parameters are $u_*^{eff} = 0.341 \text{ m s}^{-1}$, $z_{0h}^{eff} = 0.0041 \text{ m}$, $\psi_h^{eff} = 1.11$ and $\Delta T_a^{eff} = 8.5 \text{ K}$ while the values at unit 1 are $u_* = 0.36 \text{ m s}^{-1}$, $z_{0h} = 0.0056 \text{ m}$, $\psi_h = 1.14$ and $\Delta T_a = 9.3 \text{ K}$.

The estimation of E from individual hydrological units is most sensitive to ΔT_a (mean root square fractional difference 147.7%). The surface roughness length for heat transport is the second most sensitive parameter in the estimation of λE (root mean square fractional difference 43.8%). Unit 14 is the most sensitive to z_{0h} in the estimation of λE , with a % fractional difference of -5160% while unit 2 is the least sensitive with a value of 0.0%. It is important to note that use of u_*^{eff} , ψ_h^{eff} and r_0^{eff} also considerably affects the calculation of local E with root mean square fractional differences varying between 26.8% and 31.5%. Only usage of ϵ_0^{eff} seems to be acceptable. More caution is thus required when using areal constant SVAT parameters for the calculation of distributed fluxes in watersheds. This issue has so far not been properly addressed in the scientific community of remote sensing based surface energy balances.

4.8 Conclusions

A new method has been presented to quickly delineate a heterogeneous watershed into hydrological units, without having access to ground data, by using remotely sensed data. The difference in hydrology is based on only the remote sensing determined surface temperature, NDVI and r_0 . This remote sensing method does not describe land use or land cover and can therefore be applied even without identifying training areas. A watershed delineation is necessary to describe variations in Soil-Vegetation-Atmosphere-Transfer parameters and the related fluxes. The schematization into a limited number of hydrological units allows the computation of the energy balance in a spread-sheet. The spatial variation of SVAT parameters is difficult to measure in the field. Therefore, literature has been cited and used to estimate the areal patterns of SVAT parameters from spectral Landsat TM data. Field data obtained in two field campaigns held in October, 1998 and January, 1999 and long-term meteorological data were used to verify the results. The actual E of water and dry grassland agreed with those calculated from data

collected in January 1999. The E of water obtained was also within the range of those calculated from long-term data (1961-1968) for the month of January. The resulting surface resistance for wet surfaces varied from 0 to 91 s m^{-1} , which is very likely and agrees with published figures. The method proposed can be applied, under cloud-free conditions, at any watershed, river basin or irrigation scheme having heterogeneity in land surface.

The results of the parameter variability analysis and the effect on fluxes show that ΔT_a is the most sensitive parameter followed in importance by z_{0h} , u^* , ψ_h and r_0 . This implies that T_a variability needs to be described properly. The total E from a catchment can be accurately estimated from area-aggregated SVAT parameters, provided that these area-representative values are obtained through the aggregation rules given in Eq. 4.19 to 4.25 and are based on distributed SVAT parameters over the entire watershed. The consequence of this finding is that the spatial variation of SVAT parameters has to be described under all circumstances, even for calculating area-averaged watershed surface fluxes. Existing energy balance models using remotely sensed input data for distributed watershed E should therefore be re-examined on their suitability of parameterizing spatial variability in SVAT parameters. Most published algorithms in the literature appear not to be suitable for calculating watershed distributed E (e.g. algorithms in classes 1, 2, 3 and 4 in Table 4.1).

Chapter 5

Evaluation of the temporal variability of the evaporative fraction in a tropical watershed*

5.1 Introduction

Evaporation E is required on a daily basis as well as longer time scales for applications in hydrology, agriculture, forestry and environmental studies in general. However, in practice, continuous daily E measurements are rarely available at the regional scale. Traditionally daily reference E was estimated from mean daily values of available meteorological variables such as air temperature, solar radiation, humidity and wind speed. More recently, one or more instantaneous measurements of E have been used to estimate daily total E (e.g. Brutsaert and Sugita, 1992). There has been a growing interest in this approach because of its attractiveness for remote sensing applications. Remote sensing offers a means of estimating actual E at a large spatial scale, which is not possible with the traditional point methods. Many techniques have been proposed to solve the surface energy balance from remotely sensed surface temperature, surface reflectance and vegetation indices (Moran and Jackson, 1991; Kustas and Norman, 1996). Remote sensing data are, however, instantaneous measurements and a method is required to temporally integrate instantaneous estimates of E .

Latent heat flux λE and other components of the energy balance display considerable diurnal variation over land surfaces. However, several ratios of the fluxes have been shown to be relatively constant during daylight hours (Jackson et al., 1983, Shuttleworth et al., 1989 Bastiaanssen et al., 1996). The classical energy partitioning indicator is the Bowen ratio β , which is the ratio of the sensible heat flux H and λE . The pitfall in applying β for time integration is that it shows distinct diurnal variation features. More recently, the evaporative fraction Λ has been found

* Based on H.O. Farah, W.G.M. Bastiaanssen and R.A. Feddes. 2000. Evaluation of temporal variability of the evaporative fraction in a tropical watershed. *Hydrology and Earths System Sciences* (submitted)

to have little variations during daytime, although it is directly related to β (Crago and Brutsaert, 1996). The evaporative fraction is defined as:

$$\Lambda = \frac{\lambda E}{R_n - G_o} = \frac{\lambda E}{\lambda E + H} = \frac{1}{1 + \beta} \quad (5.1)$$

where R_n (W m^{-2}) is the net radiation and G_o (W m^{-2}) is the soil heat flux density. Shuttleworth et al., (1989) were the first to notice the constancy of Λ during daylight hours. They analyzed 4 clear sky days' data from the First ISLSCP Field Experiment (FIFE) over relatively homogeneous grasslands and found that midday Λ is nearly equal to the average daylight value of Λ . Nichols and Cuenca (1993), used 72 days data from the Hydrologic Atmospheric Pilot Experiment-Modelisation du Bilan Hydrique (HAPEX-MOBILHY) experiment and showed that the midday Λ is highly correlated with average daytime, Λ but that these quantities are not statistically equal. Crago (1996a), evaluated 77 days data from the FIFE. He used the data irrespective of weather conditions on a particular day and concluded that midday Λ is significantly different from the average daytime value. The difference was ascribed to the concave-up shape of the diurnal progression of Λ .

The central question is whether an instantaneous value of Λ can be used to estimate actual daily evaporation E , here expressed as latent heat flux:

$$\lambda E_d = \Lambda_{ins} (R_n - G_o)_d \quad (5.2)$$

where the subscript d indicates total daytime and ins instantaneous values respectively. This way of expressing E is a simple approach to integrate E on a daily basis and across a season, if at least the temporal variations of Λ are known. However, Eq.5.2 may not be valid under non-clear sky conditions because the diurnal constancy of Λ may not be satisfied under cloudy conditions (Zhang and Lemeur, 1995). For areas with persistent cloud cover, such as in the humid tropics, it is important to test the validity of Eq. 5.2. In order to assess the performance of the Λ approach, a long-term data series of measurements are required so that a wide range of different conditions are encountered. Most of the previously published studies have used data from relatively short time periods as reported above. In this study, field data collected over a period of about one year in the Lake Naivasha basin in Kenya are used to investigate the applicability of the Λ method to estimate

E on a daily scale and for a season. Continuous daily E measurements at two sites were compared with daily E estimates from using Eq. 5.2.

The objective of this Chapter is to demonstrate the capability of instantaneous measurements of Λ to estimate the average day Λ and E throughout a season in tropical watersheds with *data scarcity problems*. Although only field data were used in this study, the results are expected to establish a sound basis for the estimation of E from instantaneous remote sensing data and routine daily weather data. The theoretical background of Λ and reasons for its stable diurnal behavior are discussed in section 5.2. The results of estimating time integrated E is presented in section 5.3. In section 5.4, the diurnal stability of Λ is discussed and in section 5.6 the results of the comparison between instantaneous and average day Λ are presented. Finally the seasonal variations of Λ are described in section 5.6.

5.2. Theoretical background

Theoretical relationships describing the diurnal stability of Λ

The diurnal behavior of Λ can be understood from its relationship with atmospheric conditions and surface characteristics. The Penman-Monteith equation of λE combines these conditions and is expressed as:

$$\lambda E = \frac{s(R_n - G_0) + \rho c_p [e^*(z) - e(z)] / r_{ah}}{s + \gamma(1 + r_s / r_{ah})} \quad (5.3)$$

where s (Pa K) is the slope of the saturation vapor pressure curve, e^* (hPa) and e (hPa) are respectively the saturation vapor pressure and actual vapor pressure at height z (m), c_p ($\text{J kg}^{-1} \text{K}^{-1}$) is the specific heat of air at constant pressure, ρ (kg m^{-3}) is the air density, γ (hPa K^{-1}) is the psychrometric coefficient, r_s is the surface resistance to water vapor transport and r_{ah} is the aerodynamic resistance to vapor transport. In Eq.5.3, λE represents the total evaporation from surface and hence the use of r_s in the equation. This compares to Eq.2.30 in which λE reflects evaporation from a canopy only and r_c is used. Evaporative fraction Λ can be obtained by dividing both sides of Eq.5.3 by $R_n - G_0$, giving the following expression:

$$A = \frac{1}{s + \gamma(1 + r_s / r_{ah})} \left[s + \frac{\rho c_p (e^*(z) - e(z)) / r_{ah}}{R_n - G_0} \right] \quad (5.4)$$

Eq. 5.4 shows that, besides available energy $R_n - G_0$, A is a function of vapor pressure deficit ($\Delta e = e^*(z) - e(z)$), r_{ah} and r_s .

The transfer equations for heat and water vapor between the surface and the atmosphere can also be used to express A without the explicit involvement of $R_n - G_0$:

$$H = \frac{\rho_a c_p (T_0 - T_a)}{r_{ah}} \quad (5.5)$$

$$\lambda E = \frac{\rho_a c_p (e^*(T_0) - e(T_a))}{\gamma(r_s + r_{ah})} \quad (5.6)$$

where T_0 is the surface temperature. By further expressing A as $\lambda E / (\lambda E + H)$ (Eq. 5.1), an alternative expression for A becomes:

$$A = \frac{\lambda E}{\lambda E + H} = 1 - \left[\frac{1}{\left(1 + \frac{r_{ah} [e^*(T_0) - e(T_a)]}{\gamma (r_{ah} + r_s) (T_0 - T_a)} \right)} \right] \quad (5.7)$$

For ideal conditions, with no cloud obstructions and no heat or moisture advection, $R_n - G_0$, r_s , and Δe follow a regular diurnal cycle. Rowntree (1991), showed that A is more sensitive to $R_n - G_0$ when $R_n - G_0$ is small. Fig. 5.1a shows A as a function of $R_n - G_0$. It can be seen that up to a value of 200 W m^{-2} , A decreases rapidly with increasing $R_n - G_0$. Evaporative fraction A then remains almost constant with further increase in $R_n - G_0$. Available energy greater than 200 W m^{-2} , usually occurs between 9.00 and 16.00 hours. This means that variations in A are largest in the mornings and the evenings when $R_n - G_0$ is small ($< 200 \text{ W m}^{-2}$). Rowntree (1991)

also demonstrated that variations of Λ due to r_s are larger for small values of r_s (wet conditions) than for larger r_s values (dry conditions). Fig.5.1b illustrates Λ as a function of r_s . Evaporative fraction Λ decreases rapidly when r_s increases from 20 s m⁻¹ to approximately 150 s m⁻¹, but decreases at a much smaller rate at higher resistances. Because $R_n - G_0$ often exceeds 200 W m⁻² during midday conditions, Λ can be expected to behave temporally stable especially for moderately wet to dry surface conditions with r_s larger than 150 s m⁻¹.

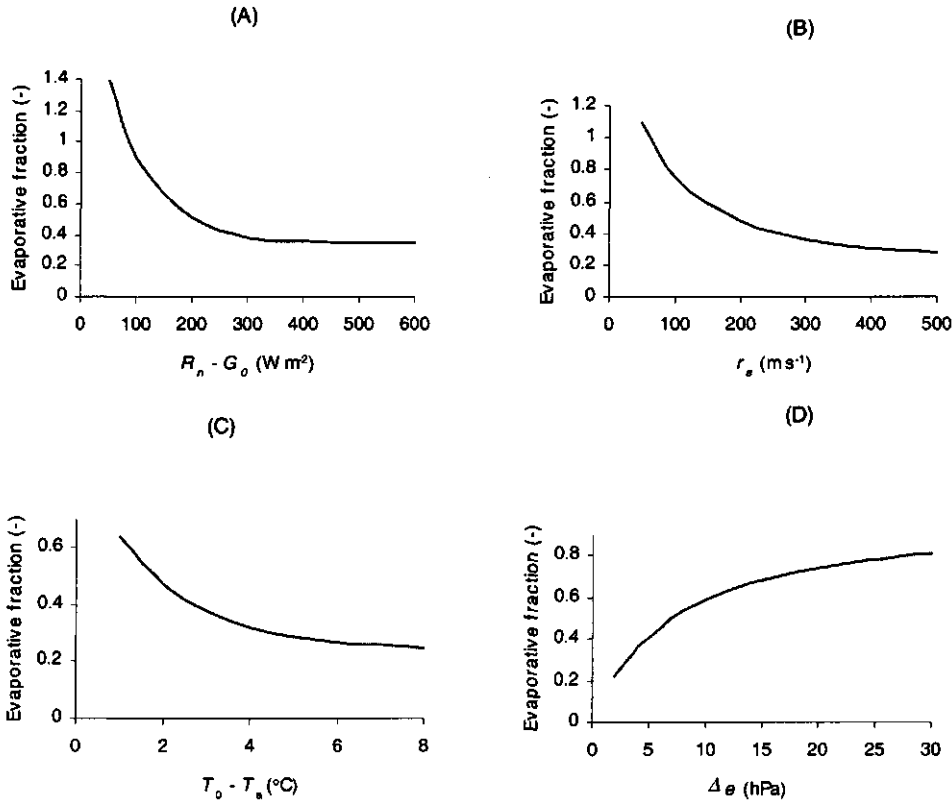


Fig. 5.1 Evaporation fraction as a function of available energy, $R_n - G_0$, surface resistance, r_s from Eq 5.4 and surface and air temperature difference, $T_0 - T_a$ and vapour pressure deficit Δe from Eq. 5.7 with the following midday conditions prevailing on 28 October 1998 at a grassland site. (a) $r_s = 300$ s m⁻¹, $r_{ah} = 70$ s m⁻¹, $\Delta e = 15$ hPa (b) $R_n - G_0 = 300$ W m⁻², $r_{ah} = 70$ s m⁻¹, $\Delta e = 15$ hPa (c) $r_s = 300$ s m⁻¹, $r_{ah} = 70$ s m⁻¹, $\Delta e = 15$ hPa (d) $r_s = 300$ s m⁻¹, $r_{ah} = 70$ s m⁻¹, $T_0 - T_a = 2$ °C

Eq. 5.7 introduces $(T_0 - T_a)$ as an important variable in the determination of λ . The diurnal trend of $T_0 - T_a$ follows closely that of $K\downarrow$. Crago (1996b) illustrated the dependence of λ on $T_0 - T_a$ for different surface conditions when $R_n - G_0$ is greater than 200 W m^{-2} . He used the formulation of Eq. 5.7 for λ to show that λ is most sensitive to $T_0 - T_a$ when $T_0 - T_a$ is small ($< 2^\circ\text{C}$). Fig. 5.1c shows the variation of λ with $T_0 - T_a$. Evaporative fraction λ remains fairly stable for $T_0 - T_a$ larger than 3°C . Such values of $T_0 - T_a$ occur in the middle of the day under clear sky conditions. Fig. 5.1d presents the relationship between λ and Δe using Eq. 5.7. Evaporative fraction λ increases with increasing Δe , however, λ increases at a lower rate for Δe values larger than 10 hPa. Values of Δe larger than 10 hPa only prevail during daylight hours when the air mass above the land surface is warm.

Computation of λ and E

In this study λ is derived from β measurements. The Bowen ratio β is determined from the difference in vapor pressure and temperature between the two observational levels:

$$\beta = \frac{H}{\lambda E} = \gamma \frac{dT}{de} = \gamma \frac{T_{a1} - T_{a2}}{e_1 - e_2} \quad (5.8)$$

where the subscripts 1 and 2 indicate the lower and upper levels respectively. The evaporative fraction λ under field conditions is then computed:

$$\lambda = \frac{1}{1 + \beta} \quad (5.9)$$

Daytime λE is calculated as:

$$\lambda E = \int_{t_1}^{t_2} \lambda (R_n - G_0) dt \quad (5.10)$$

where the time difference $t_2 - t_1$ represents the time from 8.00 to 17.00 hrs in the present study. Daytime λE can in a simplified manner, be estimated from midday λ (λ_{mid}) or morning λ (λ_{mor}). The equation when λ_{mid} is used as follows:

$$\lambda E = A_{mid} \int_{t_1}^{t_2} (R_n - G_o) dt \quad (5.11)$$

For A_{mid} and A_{mor} , measurements conducted between 12.00 to 13.00 hrs and 9.00 to 10.00 hrs respectively have been used. The daily net radiation is given by:

$$R_n = (1 - r_0) K \downarrow + L_n \quad (5.12)$$

where r_0 is the surface reflectance, $K \downarrow$ is the solar radiation reaching the earth's surface obtained from direct measurements of solar radiation and L_n is the net longwave radiation. L_n was evaluated from T_a and RH by using empirical functions (e.g. Holstlag and van Ulden, 1983). G_o is estimated as 10% of R_n during daytime hours (e.g. de Bruin and Holtslag, 1982) and ignored on a daily basis.

The degree of cloudiness is more accurately expressed as a shortwave transmittance:

$$\tau = \frac{K \downarrow}{K \downarrow_{TOA}} \quad (5.13)$$

where $K \downarrow_{TOA}$ is the solar radiation flux density incident on the top of the atmosphere, which can be calculated on the basis of standard astronomical equations (e.g. Iqbal, 1983).

The study area comprises the Lake Naivasha basin located in central Kenya (see Fig. 3.2). Two sites, namely Ndabibi and Eburu, with different canopy cover and at different altitudes were selected for in situ measurements. Two Bowen ratio towers were erected at the experimental sites. Table 3.1 shows the details of the measurements. Malfunctioning instruments caused a period of 36 days in February and March 1999 with missing data for the grassland site. Fig.5.2 shows the long term annual rainfall and potential evaporation at the Ndabibi site.

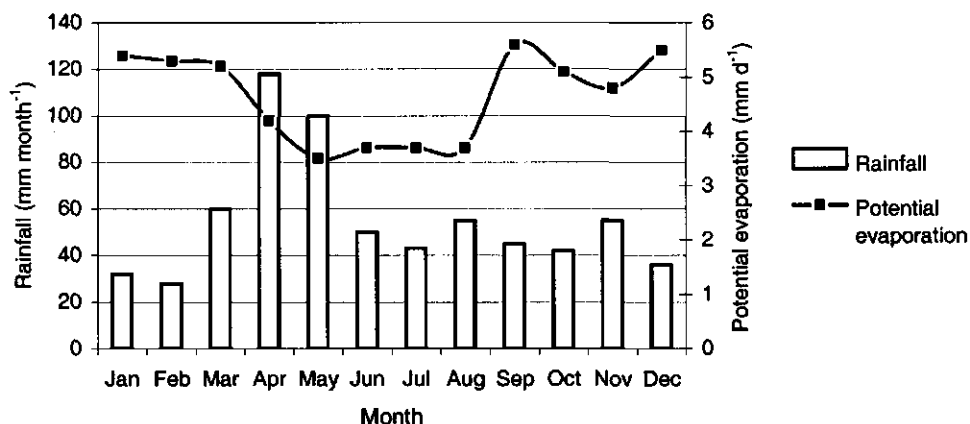


Fig.5.2. Long term average monthly rainfall and potential evaporation computed according to the Penman equation at the grassland site

5.3 Seasonal variations of actual evaporation

The progression of accumulated E , as calculated from Eq. 5.10 and measured rainfall are presented in Fig. 5.3. During the dry season, the two sites show marked differences. At the *grassland site*, E stops almost immediately after rainfall. At the *woodland site*, E continues during the two-month dry period and stops only for a few days at the end of the dry season. These differences are caused by differences in the rooting depth of the vegetation at the two sites, besides that the forest receives more rainfall annually. At the grassland site, vegetation can only get moisture from the top soil surface and as soon as the soil surface dries, vegetation stress emerges. Furthermore, the grasses at this site begin to senesce just before the dry season. Evaporation from soils is the dominant component of E at this time. Evaporation therefore stops a day or two after a certain rainfall event. The *woodland site* has vegetation with deeper roots, which can extract moisture from deeper soil layers. The vegetation continues to transpire even after the surface soils have dried up two months after the last rainfall event. March is the first month of rainfall and the difference between cumulative rainfall and cumulative E is approximately 80 mm at both sites. The hydrological implication of this, is that soil moisture storage, groundwater recharge and surface runoff must be significant processes at the woodland site.

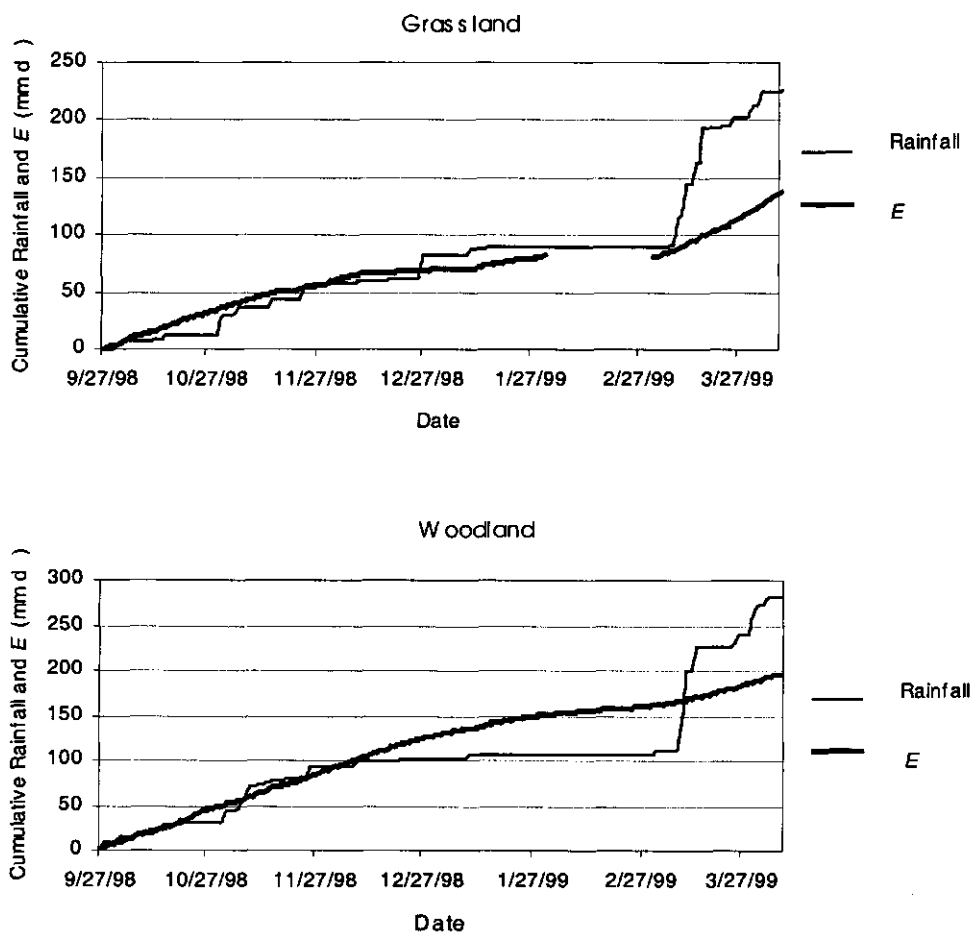


Fig. 5.3. Comparison of cumulative evaporation and rainfall measured at the grassland and woodland sites for the period 27 September 1998 to 14 April 1999

Daytime E estimated from A_{mid} and A_{mor} simulates the results of E obtainable from the satellite data with morning (e.g. Landsat) or afternoon (e.g. NOAA AVHRR) over passes at the equator. Fig. 5.4 shows the comparison of measured E and estimated E from A_{mid} for the two sites. The coefficient of determination r^2 and the root mean square error RMSE are also presented in Fig. 5.4 and Table 5.1 respectively. The values of measured and estimated E compare very well at both sites. The RMSE for daily values are 0.17 mm at the grassland and 0.14 mm at the woodland site. These results apply to the entire study period, however, on an

individual monthly basis the largest RMSE for daily values obtained are 0.21 mm and 0.18 mm for the month of April for the grassland and woodland site respectively. With respect to r^2 , the lowest values are 0.77 for the month of January at the grassland site and 0.66 for the month of February at the woodland site. The months of January and February are the driest months in the year and therefore E is very small during this period. Although the comparison between measured and estimated E may appear poorer for the drier months, the RMSE are comparable to the other months. Table 5.1 shows the RMSE of estimated E on daily, 10 day and monthly scales. It can be seen that the RMSE reduces with longer time scales. This indicates that accumulated E is more accurate than daily E if estimated from instantaneous E .

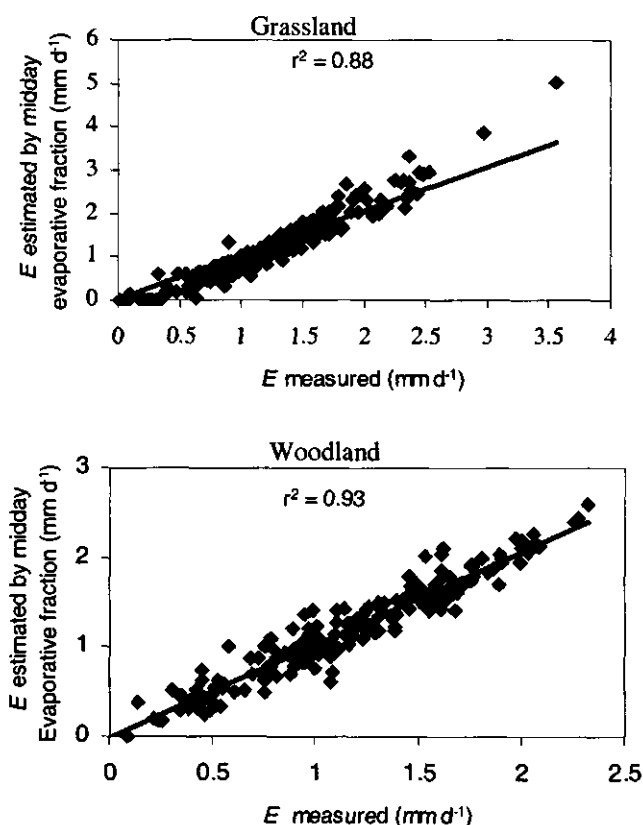


Fig. 5.4. Comparison of measured evaporation E and estimated E by midday evaporative fraction at the grassland site for the period May 1998 to April 1999 and the woodland site for the period October 1998 to April 1999

Table 5.1. Root mean square error RMSE of estimated evaporation E from midday evaporative fraction on daily, 10-day and 20-day time scales for the period May 1998 to April 1999 at the grassland site and October 1998 to April 1999 at the woodland site

Time scale	Grassland	Woodland
	RMSE E (mm)	RMSE E (mm)
Daily	0.17	0.14
10-day	0.12	0.06
20-day	0.05	0.04

The daytime E estimated by Λ_{mor} gave poorer results than when estimated by Λ_{mid} . The RMSE values are 0.37 mm and 0.29 mm at the woodland and grassland sites respectively. These values are about twice as large as those obtained when Λ_{mid} was used. The r^2 obtained are 0.33 and 0.65 for the grassland and woodland sites respectively. This implies that in remote sensing studies, data from satellites with afternoon overpass will give a better estimate of E compared with those with morning overpass.

5.4 Diurnal stability of the evaporative fraction

The standard deviation of measured Λ ($SD\Lambda$) between 8.00 and 17.00 hrs was calculated and used as an indicator of the diurnal stability of Λ . The mean $SD\Lambda$ for the grassland site is 0.071 at an average Λ of 0.40 yielding a coefficient of variation of 0.18. $SD\Lambda$ varies considerably during the study period. The months of March, April, May and June, have the largest diurnal variations with a mean standard deviation of 0.082 and with minimum 0.02 and maximum 0.17 values occurring on individual days. The remaining period has a mean standard deviation of 0.060, with a minimum of 0.01 and a maximum of 0.15. For the woodland site, the mean $SD\Lambda$ is 0.045 at an average Λ of 0.33, hence a coefficient of variation of 0.14 arises. The months of March and April have the highest $SD\Lambda$ of 0.060. At both sites, the periods of largest $SD\Lambda$ coincide with the rainy season. During the rainy days, $R_n - G_0$, $T_{a1} - T_{a2}$ and Δe are small. Fig. 5.1 demonstrated on a theoretical basis that Λ is most sensitive to variations in $R_n - G_0$, $T_{a1} - T_{a2}$ and Δe when these variables are small values. These affect the diurnal cycle of the surface energy fluxes and the

numerical stability of Λ . In comparison, the $SD\Lambda$ of the woodland site is much lower than that of the grassland site. This indicates that the diurnal stability is site-dependent.

An analysis of the relationship between $SD\Lambda$ and T_a , RH and τ was undertaken to see if routinely collected weather data could be used to understand the diurnal stability of Λ . Table 5.2 shows the r^2 of the relationships. The relationships were modeled by polynomial curves having an order 2. The daily $SD\Lambda$ has a very weak relationship with T_a , RH and τ . The relationship between 10-day average $SD\Lambda$ and 10-day average T_a , RH and τ is also weak (Table 5.2). To examine the effect of cloudiness on the stability of Λ , the days were stratified according to the daily average τ values and put into three groups. The groups were defined as cloudy ($\tau < 0.5$), partly cloudy ($0.5 > \tau > 0.65$) and clear ($\tau > 0.65$). Table 5.3 shows that the average $SD\Lambda$ for the three groups is almost the same, thus indicating that cloudiness is not related to the stability of Λ . Hence, the stability of the diurnal cycle of Λ can not be adequately explained by micrometeorological state variables only.

Table 5.2. Relationship between daily and 10-day average standard deviation of the evaporative fraction $SD\Lambda$ and meteorological variables used to explain the diurnal stability of Λ .

Meteorological Variables	r^2 -1day		r^2 -10 day average	
	Grassland	Woodland	Grassland	Woodland
τ	0.05	0.07	0.27	0.33
RH	0.11	0.10	0.31	0.21
T_a	0.10	0.09	0.34	0.18

Table 5.3. Average daytime standard deviation of evaporative fraction $SD\Lambda$ grouped according to the atmospheric transmission τ to solar radiation, in order to understand the relationship between cloudiness and diurnal stability of Λ

No. of days		τ	Mean standard deviation of evaporative fraction, Λ	
Grassland	Woodland		Grassland	Woodland
114	40	<0.5	0.075	0.049
91	61	≥ 0.5 and ≤ 0.65	0.078	0.045
99	103	>0.65	0.068	0.041

There is no consensus in the literature on the effects of clouds on the diurnal cycle of Λ . While Hall et al., (1992) conclude that variations in R_n due to cloudiness should not affect Λ significantly, Sugita and Brutseart (1991) attribute daytime changes in Λ to changes in cloudiness. They attribute increase in Λ to decrease in R_n as clouds pass over. Crago (1996b) observes that cloud fields tend to change $R_n - G_0$ and surface temperature erratically and thereby cause changes in Λ . He concludes however, that the effect on Λ may not be observed in practice as it may be masked by coincident changes in RH and wind speeds. This implies that diurnal variability of Λ is a complex phenomenon and other factors influencing the variations of Λ in Eqs. 5.3 and 5.7 need to be considered more carefully. The other variables that control Λ , are r_s and r_{ah} (see Eq. 5.4), of which r_s is the dominant surface variable, that regulates Λ . Surface resistance r_s depends on micrometeorological variables, soil moisture and plant physiology (Jarvis, 1976; Stewart, 1988). Surface resistance r_s has a diurnal trend. *Modeling of surface resistance is therefore required in order to understand better the diurnal dynamics of Λ .*

5.5 Comparison of midday and morning evaporative fraction and average daytime evaporative fraction

The relationships between Λ_{mid} and average daytime Λ for the grassland and woodland sites are presented in Fig. 5.5. All days were used irrespective of weather conditions. *There is a strong relationship between Λ_{mid} and daily Λ .* The r^2 for the regression lines through the origin are 0.71 and 0.75 while the RMSE are 0.095 mm and 0.070 mm for the grassland and woodland site respectively. The 1:1 line (Fig. 5.5 grassland) shows that Λ_{mid} values larger than 0.65 are higher than corresponding daytime values while Λ_{mid} values smaller than 0.30 are less than the daytime values, which reveals a slightly concave type of relationship. Evaporative fraction Λ values larger than 0.65 occur in the rainy months of May, June and April. During these wet periods, when there is no moisture deficit, E is highest at midday. Evaporative fraction Λ is expected to be higher at midday as compared with the rest of the day. In contrast, Λ values less than 0.3 occur mostly in the dry months of January, February and December. Evaporation is significantly reduced for the whole day however available energy, $(R_n - G_0)$ is highest at midday. Evaporative fraction Λ values will therefore tend to be lower at midday, as compared with the rest of the day and under estimate the daytime Λ . It can also be seen from Fig. 5.4 that *the relationship between measured and estimated E is better than the relationship between average day Λ and Λ_{mid} .* This is because more weight is given to the midday period in the calculation of daytime E , when $R_n - G_0$ is large and Λ is more stable.

The relationships between average Λ_{mor} between 9.00 and 10.00 hrs and average daytime Λ were determined to study the potential of using satellite remote sensing based data acquired during the morning hours. Compared with midday conditions, the r^2 for the period 9.00 to 10.00 hrs is lower, with 0.64 and 0.65 for the grassland and woodland sites respectively. Poorer RMSE of 0.112 mm and 0.106 mm were also obtained at the grassland and woodland site respectively. The implication of the results for remote sensing studies is that *midday satellite passes* (e.g. NOAA AVHRR) *will give better average daily Λ than the morning passes* (e.g. Landsat).

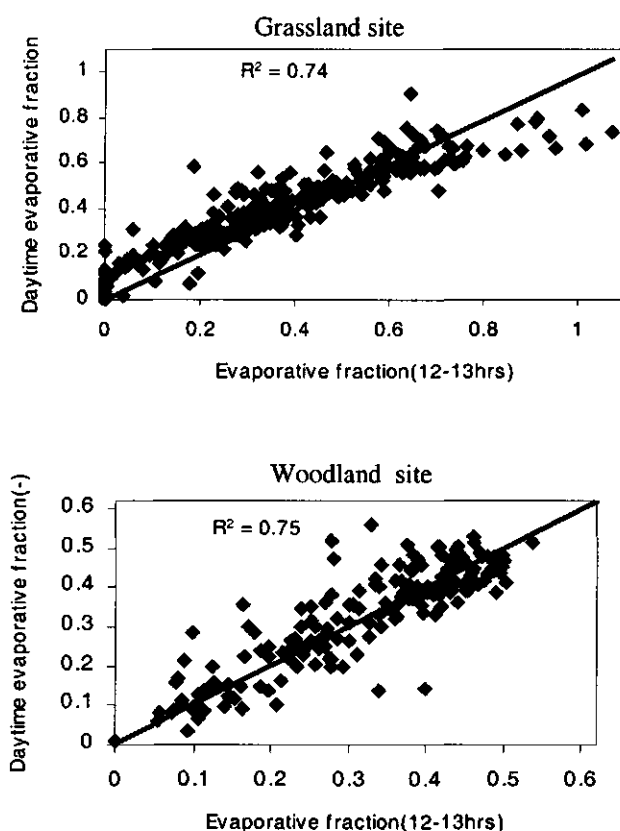


Fig. 5.5. Relationship between midday and daytime evaporative fraction Λ fraction at the grassland site for the period May 1998 to April 1999 and the woodland site for the period October 1998 to April 1999

5.6 Seasonal variations of evaporative fraction

The pattern of the seasonal variation of Λ is presented in Fig. 5.6. Each of the points represents the average Λ between 8.00 and 17.00 hrs. The seasonal variation of Λ is a reflection of the climate of the area, in particular of rainfall and soil moisture behaviour. Superimposed on this trend are fluctuations of Λ from day to day caused

by variations in the micrometeorological conditions as elucidated in the previous section.

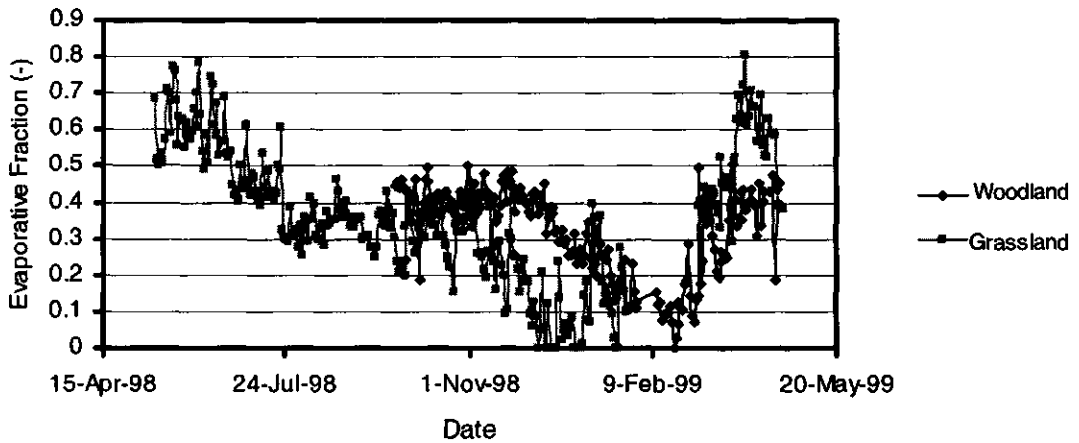


Fig. 5.6. Seasonal progression of the daytime (8 – 17.00 hrs) evaporative fraction at the grassland site for the period May 1998 to April 1999 and the at the woodland site for the period October 1998 to April 1999

For the *grassland site*, A drops quickly from 0.7 at the end of May to 0.3 in approximately 60 days. The reduction in A may be attributed to the reduction of soil moisture availability in the root zone due to sharply reduced rainfall rates. Evaporative fraction A fluctuates around 0.3 for about 100 days between the end of July and the beginning of November. This is followed by a sharp decline in A , reaching virtually zero within 45 days. This indicates that A responds to soil moisture conditions when a certain critical level of moisture and soil water potential is reached and plant stress is triggered. Periods when $A = 0$ imply that all of the available energy is partitioned into sensible heat flux. There is an increase in A in the month of January from zero to 0.4 in response to a rainfall event (see Fig. 5.6). However A declines to zero in a few days. Evaporative fraction A finally increases from zero at the end of January to 0.8 by April in response to the rainy period starting at the end of March. Although no A data are available in the month of February and the beginning of March, rainfall data were available. During this

period only 0.5 mm of rainfall was recorded. It is therefore expected that Λ remains in the range from 0 to 0.1 between February and March.

For the *woodland site*, Λ remains fairly constant at about 0.4 from the end of September for about 80 days. Evaporative fraction Λ then begins to decline steadily to reach zero in about 70 days. Compared with the grassland site, here the decline in Λ takes a longer period. This is related to the differences in total water storage in the root zone and vegetation at the two sites. The value of Λ finally increases in response to rainfall and soil moisture replenishment in early March. However, Λ increases to a maximum of 0.5 by the end of April as compared with 0.8 in the grassland site. This could be ascribed to the lower Δe prevailing in the woodland site, which causes lower degrees of partitioning $R_n - G_0$ into λE and hence limits E . Other reasons could be the more hilly terrain at the woodland site resulting in more runoff and less infiltration. The woodland has relatively higher interception losses as well. These factors culminate in lower soil water content and hence lower Λ , as compared with the grassland site.

The seasonal progression of Λ is gradual at both sites. The implication of this for the monitoring of Λ is that it *would be sufficient to measure Λ , say, every 10 to 20 days to capture the seasonal evolution of Λ* . Interpolation between the measurements can be done to estimate Λ on days when no Λ measurements are available. This means that for remote sensing programs, the processing of daily images is not necessary to estimate the seasonal variations of Λ for large watersheds, albeit daily acquisition might be required to select the best cloud-free image for a given period.

Estimation of Λ by standard weather data

Soil moisture dynamics and thus indirectly the rainfall events, control the long-term seasonal variations of Λ . The seasonal trends of micro-meteorological variables such as T_a , RH and τ follow the annual rainfall regime. Rather than the daily processing of satellite images, these variables obtained from standard weather stations could be used to estimate the seasonal variations of Λ . A regression analysis between Λ and T_a , RH and τ was performed on the basis of 1-day and 10-day average values. Multiple linear regression between Λ and all the three micro-meteorological variables was performed as well. The relationships between Λ and

the variables at the grassland site at the seasonal scale are presented in Fig. 5.7, while Table 5.4 shows the coefficient of determination r^2 of the relationships at the two sites.

Table 5.4: The relationship between daily and 10-day average evaporative fraction Λ and meteorological variables for the period May 1998 to April 1999 at grassland site and October 1998 to April 1999 at the woodland site

Meteorological variables	r^2 1-day		r^2 10-day averages	
	Grassland	Woodland	Grassland	Woodland
τ	0.25	0.23	0.45	0.31
RH	0.62	0.63	0.74	0.83
T_a	0.57	0.49	0.74	0.81
$RH \text{ \& } T_a$	0.64	0.62	0.82	0.83
$\tau, RH \text{ \& } T_a$	0.67	0.64	0.87	0.86

The maximum value of Λ coincides with T_a of 25 °C (see Fig. 5.7). The optimum RH for both sites is 50%. These agree with the optimum meteorological conditions for E for vegetated surfaces found by Stewart, (1988). RH best explains the average day Λ with an r^2 of 0.69. As expected, there is an improvement in the relationships if 10-day average values are considered, due to smoothing effects (see Table 5.4). In the multiple linear regression an r^2 of 0.67 for daily averages and 0.87 for the 10-day average values were obtained for the grassland site. It is worthwhile to note that in the 10-day average values *standard weather data can explain 87% of the variations of Λ* . This has important implications for hydrological applications requiring 10-day average Λ . Once the site-specific relationships have been established, routine weather data could be used to estimate Λ empirically.

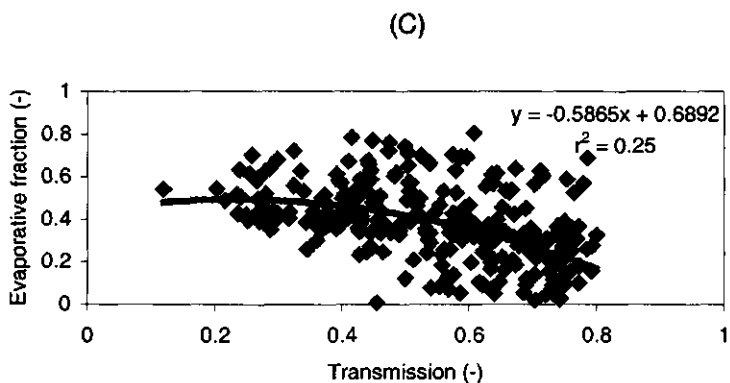
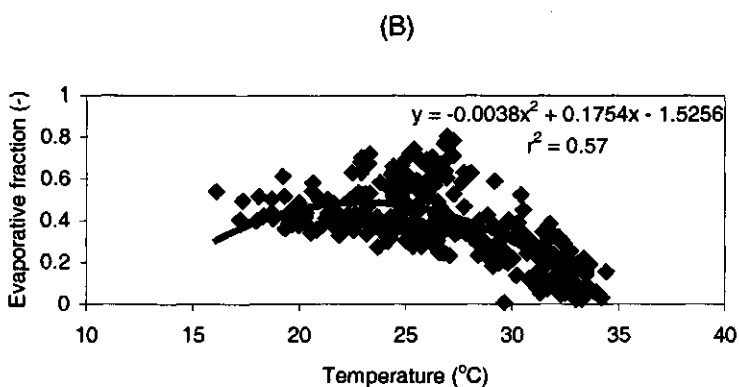
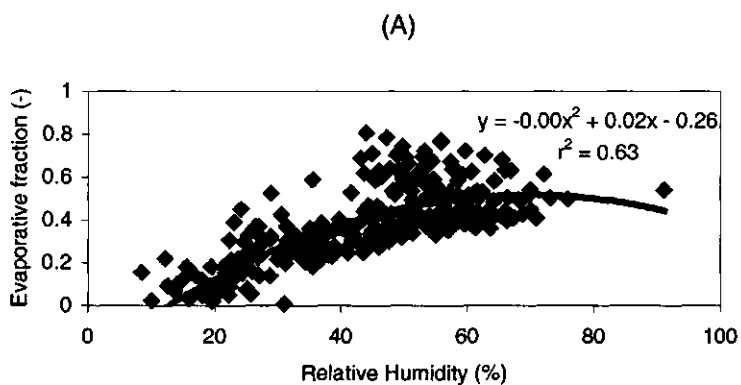


Fig.5.7. Evaporative fraction as a function of : (A) air temperature T_a (B) relative humidity RH (C) atmospheric transmission τ at the grassland site for the period May 1998 to April 1999

5. 8 Conclusions

The objective of this study was to investigate the use of the diurnal constant behavior of Λ to estimate daytime average Λ and daytime total of E throughout a complete season. The results presented show that the diurnal stability of Λ varies significantly during the study period. The daily standard deviation of Λ varies from as low as 0.01 to as high as 0.16. The results also show that on the daily time scale, the variations of Λ cannot be well explained by meteorological variables and cloudiness alone. The variations could be due to other causes, such as the diurnal variation of surface resistance and energy and moisture advection. The evaporative fraction is more unstable during the cloudy and rainy period (April, May and June) than in the other months due to low $R_n - G_0$, Δe and $T_{a1} - T_{a2}$ values. The evaporative fraction is more temporally stable at the woodland site than at the grassland site.

The data presented showed that there is a strong relationship between Λ_{mid} and daytime Λ with the average r^2 of the regression lines through the origin at both sites being 0.74. The changes in Λ over an annual period are gradual. It can be concluded that for remote sensing programs, an acquisition of images, say, *every 10 to 20 days may be able to capture the seasonal evolution of Λ for large watersheds.* Furthermore, *the interpolation of Λ , between remote sensing days, can be accomplished by routinely collected weather data.*

The estimated daytime E from Λ_{mid} compare very well with the measured daytime E (RMSE = 0.17 mm, $r^2 = 0.88$ for the grassland). For the whole study period the average daily difference between the estimated E and the observed E was within 10%. The differences reduced even further if 10-day and monthly integrated E values were considered. Poor E results were obtained from Λ_{mor} (RMSE = 0.37 mm, $r^2 = 0.33$ for the grassland). This indicates that *the use of data from satellites with morning overpass will give less accurate daily E values* in the environmental conditions of Kenya. NOAA AVHRR satellite images with afternoon overpass are preferred although a loss of spatial scale accuracy should be accepted. The important conclusion from this study is that *the hypothesis of quasi-constant Λ to estimate seasonal variations of E is valid for tropical watersheds under general weather conditions.* This provides a basis for the use of remote sensing methods in applied regional hydrology in tropical watersheds with data scarcity problems.

Chapter 6

Derivation of daily evaporation under all weather conditions from standard meteorological data and clear sky flux information^{*}

6.1 Introduction

Bussieres and Goita (1997) presented a general discussion of the problems of cloudiness encountered in the determination of evaporation E from remote sensing studies in their study of the Mackenzie basin in western Canada. They defined a clear sky situation as when not more than 20% of the basin is covered by clouds. They observed that the chance of a clear sky is about 9% in the mountainous areas and about 30% in the low lying areas. They suggested the use of microwave data and compositing techniques as two possible ways to overcome this problem. Microwave data are difficult to use on a routine basis because of difficulties in their algorithm formulation and the high costs of data acquisition. In the compositing technique, 10 images, taken over consecutive days, were overlaid and the brightness temperature of the corresponding pixels compared. The pixels with the highest temperature from the 10 images were considered cloud-free and selected to form one image. Evaporation was then calculated for this resulting image. This compositing technique is simple to implement but has the disadvantage of not representing E on a single day but the highest E within a 10-day period.

Rosema (1993) used Meteosat satellite data to calculate 10-day average evaporation for Burkina Faso in West Africa. For cloud-covered pixels in an image, he used a soil moisture model to determine E so as to produce a continuous evaporation map. Evaporation was estimated from the relationship between soil moisture status parameterized in terms of the depth of the drying front in the soils and E . The depth

^{*} Based on: H.O. Farah and W.G.M. Bastiaanssen. 2000. Derivation of daily evaporation under all weather conditions from standard weather data and clear sky flux information. *Agriculture and Forest Meteorology* (submitted)

of the drying front was determined for a clear day from remotely sensed E . If the next day a pixel was cloud-covered, this depth and the estimated diffusion resistance of the soils (from average surface temperature) were used to calculate E . The net radiation for cloud-covered pixels could not be calculated and was crudely estimated. Therefore the resulting estimated E might not be reliable. Moreover, the objective of Rosema (1993) was only to estimate E for the few pixels with cloud cover in an image. In the case of complete cloud cover or non-availability of images on a particular day, the values of E from the last available image were used.

Sandholt and Anderson (1993) suggested using the relationship between E and root water potential to model the drying of the land surface and to estimate E during periods of missing satellite data. Since data on root water potential are usually not available, they used instead the difference between accumulated E and rainfall. However, this will give only approximate E because other soil water balance terms are neglected. Furthermore they determined E for only four pixels in the image.

Courault et al. (1996) reported on the use of an agro-meteorological model to simulate continuously the energy and water balances to derive E . Airborne infra red data obtained on cloud free days were used to update the model. The method was implemented at the field scale. Extending it to the regional scale on an operational basis may be difficult because of the detailed soil and vegetation information required to run the simulation model, which are often not available.

In this chapter, a framework is presented in which a combination of optical remote sensing and standard weather data are used to obtain continuous daily evaporation over a season is presented. This approach avoids the need for a soil moisture simulation model. The present study is based on in-situ data but can be executed by means of satellite estimates of E . Soil water pressure head h_{rw} is derived from E measurements on cloud free days by means of:

- inversion of the Penman-Monteith equation to obtain surface resistance, r_s , and
- using r_s and standard weather data to invert the Jarvis-Stewart type of model to obtain h_{rw} .

Soil moisture fluctuations from day to day are in general gradual and an h_{rw} value on a certain day can be used, together with the standard weather data on neighboring days, to calculate r_s on these neighboring days by using the Jarvis-Stewart model in a forward manner. Evaporation can then be calculated for these

days from the estimated r_s and standard weather data using the Penman-Monteith equation.

Evaporative fraction Λ , can alternatively be used to fill gaps of missing E data in remote sensing E monitoring studies. Evaporative fraction is defined as the ratio of evaporation and net available energy. It is a good indicator of the partitioning of the net available energy into sensible heat and latent heat energy (Shuttleworth et al., 1989; Crago, 1996a) and has been shown to be a suitable soil moisture indicator with a gradual seasonal evolution (Gash et al., 1991; Farah et al., 2000). These characteristics of Λ could be fruitfully utilised to estimate E on cloudy days when satellite data are not available and should be considered as a simplified alternative to the approach which uses the Penman-Monteith and Jarvis-Stewart models.

6.2 Material and Methods

Use of Penman-Monteith and Jarvis-Stewart models

A Jarvis-Stewart (*JS*) type of model used by Hanan and Prince (1997) in the HAPEX-Sahel study area was adapted for this study for reasons of similarities in land surface characteristics. Despite their empirical nature, the *JS* models work quite well in predicting E in diverse climate conditions. Stewart (1988) and Dolman et al. (1991) demonstrated the robustness of these types of models. They calibrated a *JS* type model with 90 days data of E and weather data at a forest site in the United Kingdom. Evaporation E was measured by both the energy budget and Bowen ratio method. The *JS* model and weather data were used to predict daily E for a three-year period. To assess the potential of using the *JS* model for different forests they changed the model coefficients by 20% and calculated E over a 3-year period. They showed that none of the changes in the model coefficients produced a change greater than 5% in the model output and concluded that the *JS* model could be easily adapted for other forests.

Stewart and Gay (1989) tested whether the *JS* type models established at one area could be used with the *PM* equation to successfully estimate E at other areas with some what different environmental conditions. They fitted the *JS* type model to 60 days data obtained at a valley bottom site during the First International satellite land surface climatology project Field Experiment (FIFE) to estimate E at another site located on a plateau. They reported a 5% difference between estimated and

measured E at the plateau site. De Rooy and Holtslag (1999) also found good estimates of E by using a simplified JS type of model to model r_s with only one function that relates to vapour pressure deficit. Their work was based on a grassland area in the Netherlands with no soil moisture deficit.

Hanan and Prince (1997) determined the empirical coefficients for the four main vegetation types present in the Sahelian landscape of Niger during the international HAPEX-Sahel experiment: forbs, shrubs, grass and millet. A similar type of vegetation is predominant in the Kenyan study area. Their model estimates r_s as:

$$r_s = \frac{r_{s \min}}{LAI F_2(T_a) F_3(\Delta e) F_4(h_{rw})} \quad (6.1)$$

The function $F_2(T_a)$ represents the effect of air temperature T_a on r_s and is described as:

$$F_2(T_a) = \frac{(T_a - T_{\min})(T_{\max} - T_a)^b}{(a_3 - T_{\min})(T_{\max} - a_3)^b}, \quad b = \frac{T_{\max} - a_3}{a_3 - T_{\min}} \quad (6.2)$$

where T_{\min} is the minimum air temperature, T_{\max} the maximum air temperature for stomatal conductance and a_3 is a coefficient representing the optimum air temperature for stomatal conductance. The temperatures T_{\min} and T_{\max} take the values of 5 °C and 55 °C respectively. The vapour pressure deficit function, $F_3(\Delta e)$ is given as:

$$F_3(\Delta e) = \frac{1}{1 + a_4 \Delta e} \quad (6.3)$$

where Δe is the vapour pressure deficit (hPa) and a_4 is an empirical coefficient. The function $F_4(h_{rw})$ is described as:

$$F_4(h_{rw}) = 1 - \frac{h_{\max} - h_{rw}}{h_{\max} - a_5} \quad (6.4)$$

where h_{rw} (cm) is the average root-weighted soil water pressure head, h_{max} is the soil water pressure head at field capacity and a_5 is an empirical coefficient representing soil water pressure head at wilting point. The minimum surface resistance r_{smin} is modeled as a function of incident photosynthetically active radiation (PAR):

$$r_{smin} = \left[\frac{a_1 PAR}{a_2 + PAR} \right]^{-1} \quad (6.5)$$

The photosynthetically active radiation is estimated from measured incoming solar radiation. The values of the coefficients used at the two sites are shown in Table 6.1. The coefficients obtained for grasses and shrubs were used at the Ndabibi and Eburu sites respectively.

Table 6.1: Values of the coefficients used in the Jarvis-Stewart type resistance model (Eqs. 6.1 to 6.4) to predict surface resistance r_s at the Ndabibi and Eburu sites.

Site	a_1 (mm s ⁻¹)	a_2 (W m ⁻²)	a_3 (°C)	a_4 (hPa ⁻¹)	a_5 (cm)
Ndabibi	13.2	3.5	28	0.017	-2500
Eburu	28.4	6.5	28	0.007	-2011

Figure 6.1 shows schematically how the *PM* and *JS* models will be used to estimate E . For Day 1, on a clear day, E could be assessed from a satellite overpass and routine weather data. The surface resistance r_s is obtained by inversion of the *PM* model. The $F_4(h_{rw})$ function in the *JS* model is then inverted to get the soil water pressure head, h_{rw} (Eq 6.4). The value of h_{rw} obtained is then used in the subsequent cloudy days (days 2,3,4,5) in which E measurements are not available but standard weather data are available. On these cloudy days the reverse process is followed to determine E . Weather data routinely gathered in days 2, 3, 4 and 5, together with h_{rw} from day 1, are used in the *JS* model to calculate r_s . Finally, E is derived from the *PM* equation for each of the cloudy days separately.

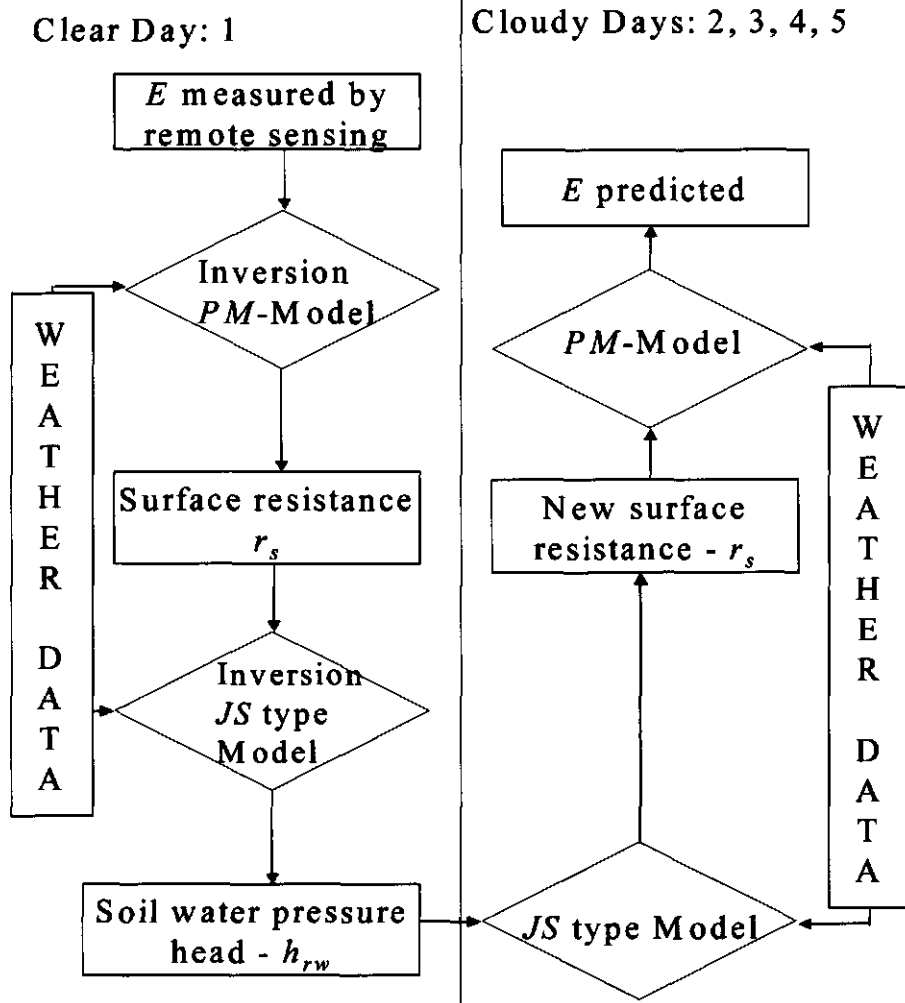


Fig. 6.1. Schematic diagram of the use of the Penman-Monteith (PM) and Jarvis-Stewart type models in predicting evaporation E on cloudy days (2, 3, 4, 5) without satellite data being available.

In this study, h_{rw} has been determined at 20-minute intervals and an average has been taken between 9.00 and 16.00 hrs. This average h_{rw} was used to calculate r_s and hence E every 20 minutes on the days with no E measurements being available. The 20-minute interval E is summed from 9.00 to 16.00 hrs and compared with E obtained from the Bowen ratio method. The period between 9.00 and 16.00 hrs was selected so as to avoid the use of unreliable E measurements, due to the numerical instability of the Bowen ratio method outside the selected period.

Use of the evaporative fraction

The average Λ between 12.00 and 13.00 hrs was calculated for a day with E measurements, here termed as day 1. This was to simulate the Λ obtained from satellite data, which has an overpass time of around midday. The evaporative fraction thus obtained was then used in the subsequent days to determine E , assuming constancy in energy partitioning during these days:

$$E = (R_n - G_0)_{avg.day(n+1)} \Lambda_{day1} \quad (6.6)$$

In this study $(R_n - G_0)_{avg}$ is the average of 20-minute interval measurements between 9.00 and 16.00 hrs and n was not greater than 4. Measured or estimated $R_n - G_0$ is assumed to be available on all days.

Field experiment

The data from the field experiments carried out at the Ndabibi and Eburu sites and described in Chapter 3 and Chapter 5 were used.

Monthly values of LAI for the study area were obtained from remotely sensed vegetation indices (Smith et al., 1997). Due to lack of wind speed measurements and the usual estimation of land surface aerodynamic characteristics, the aerodynamic resistance was retrieved from the sensible heat flux:

$$H = \lambda E \beta = \frac{\rho_a c_p (T_1 - T_2)}{r_{ah}} \quad (6.7)$$

where T_1 and T_2 are the air temperature observed at the levels of 0.3 m and 2 m respectively.

Field data were used to simulate remote sensing data for the experimental sites. This does not hinder the objectives of demonstrating the potential of the *PM* equation and *JS* models in the estimation of E from standard weather data and complemented with r_s .

Three types of analyses were performed. First, the daily data were divided into two, the odd and even numbered dates. It was assumed that E was known on the odd dated days, but unknown on the even dated days. The second and third analyses considered that E was known every third or fifth day only, i.e. cloud-free condition once in 4 or 6 days respectively. For the unknown days, E was estimated by the *PM* and *JS* models and the *A* method, described above. The estimated E values were then compared with measured values from the Bowen ratio surface energy balance method.

6.3 Results and discussion

Diurnal evolution of surface resistance, r_s

Figure 6.2 shows the diurnal variations of r_s obtained from the inversion of the *PM* equation, using E measured by the Bowen ratio method at the Ndabibi and Eburu sites for a typical dry and a typical wet day. During dry periods, the general trend is a rapid increase in r_s from early morning to midday, followed by a decrease in the afternoon. For wet periods, r_s is low and mostly less than 200 s m^{-1} in the morning but it increases in the after noon. The diurnal variation of r_s during the wet day is smaller than that for the dry day. A comparison between the 20-minute interval predicted r_s by the *JS* model and the r_s inverted from measured E by the Bowen ratio method, gave poor results. The predicted and measured r_s were averaged between 9.00 and 16.00 hrs and compared.

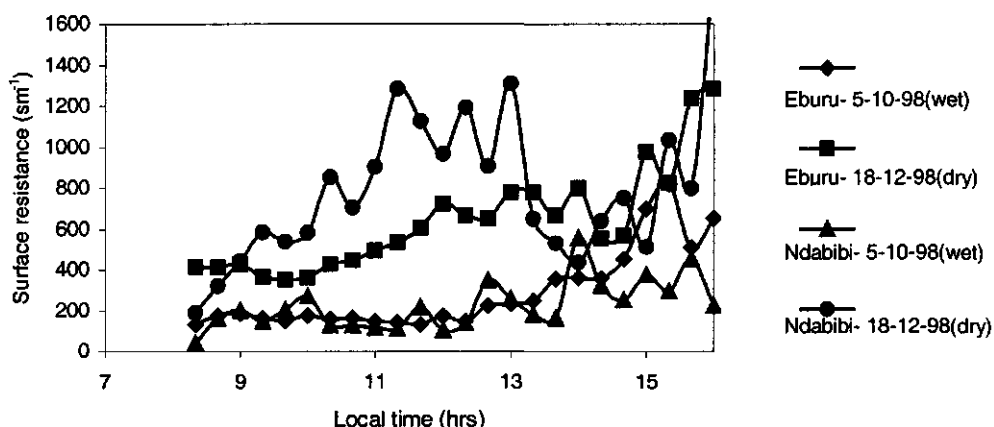


Fig.6.2: Diurnal variations of surface resistance r_s at the Eburu and Ndabibi sites on a wet day (5 October 1998) and a dry day (18 December 1998)

Figures 6.3a and 6.3b show these comparisons for the 1-day extrapolation cases for the Ndabibi and Eburu sites respectively. It can be seen that good agreement is obtained with the regression coefficient r^2 of the line through the origin being 0.51 and 0.54 for Ndabibi and Eburu respectively. This indicates that errors in the 20-minute interval r_s are random rather than systematic as they considerably reduce when r_s is averaged over a longer time period. It can be seen that the divergence between the predicted r_s and the r_s inverted from measured E increases with increasing value of r_s . *This means that prediction of r_s is better during wetter conditions when r_s is relatively small and less than 400 s m^{-1} .* It also demonstrates that the predicted r_s is acceptable and could be used in the PM model to estimate E .

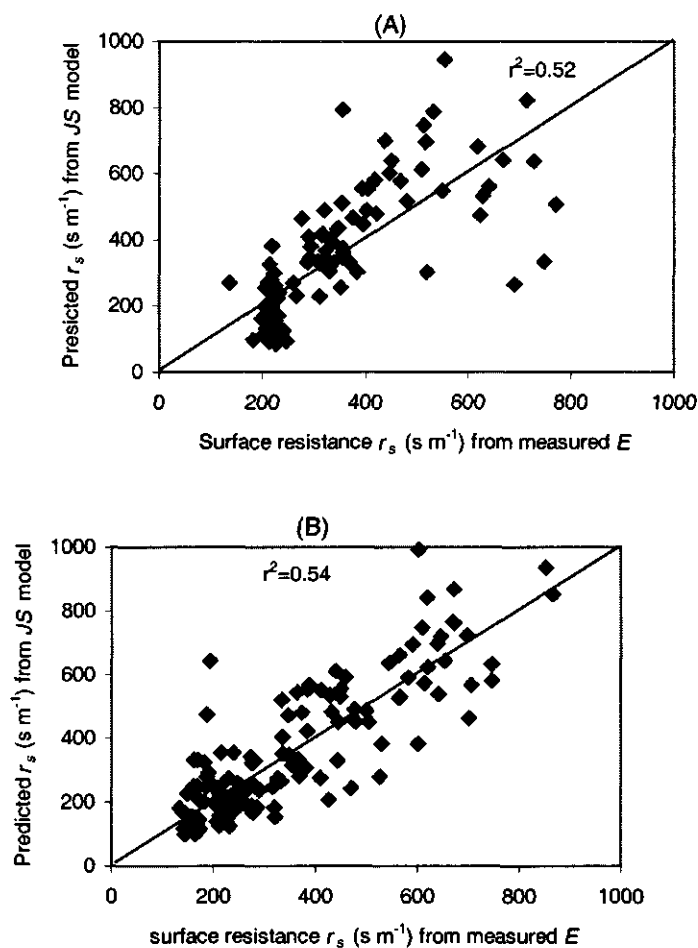


Fig.6.3. Comparison of surface resistance r_s from measured evaporation E and predicted from the Jarvis-Stewart (JS) type of model for the 1-day extrapolation case for the period 27 September 1998 to 24 April 1999: (A) Ndabibi site, (B) Eburu site

Tables 6.2 and 6.3 show the results of the comparison of estimated E , using the predicted r_s and meteorological data, and measured E for the whole study period. The regression coefficient r^2 and the slope of the regression line through the origin are given. The comparisons of average daily values for a monthly period are also given. Good agreement is obtained between the predicted E and measured E for the whole study period at both sites. As expected, the relationship between estimated and measured E is best for the 1-day extrapolation case and worst for the 5-day extrapolation as indicated by r^2 . The Root Mean Square (RMSE) error shows values of less than 0.25 mm in all three extrapolation cases.

Table 6.2: Comparison of daily evaporation rate E measured by the Bowen ratio surface energy balance method and predicted by the Penman-Monteith and Jarvis-Stewart type model and climate data at the *Ndabibi* site. The regression lines are through the origin.

Period	No. of days	r^2	Slope	r^2	Slope	r^2	Slope
		1-day case		3- day case		5-day case	
Sept-Oct	18	0.71	0.93	0.65	0.96	0.27	0.87
Oct-Nov	35	0.72	1.00	0.43	0.96	0.30	0.96
Nov-Dec	26	0.64	1.01	0.65	0.99	0.49	0.93
Dec-Jan	45	0.56	0.96	0.30	0.95	0.23	0.91
Mar-Apr	45	0.69	1.04	0.69	1.04	0.72	1.04
Sept-Apr	169	0.78	1.00	0.73	0.99	0.63	0.98

Table 6.3: Comparison of daily evaporation rate E measured by the Bowen ratio surface energy balance method and predicted by the Penman-Monteith and Jarvis-Stewart type model and climate data at the *Eburu* site. The regression lines are through the origin.

Period	No. of days	r^2	Slope	r^2	Slope	r^2	slope
		1-day case		3- day case		5-day case	
Sept-Oct	18	0.45	1.05	0.40	0.96	0.47	0.87
Oct-Nov	35	0.81	0.90	0.69	0.96	0.46	0.96
Nov-Dec	26	0.65	1.00	0.63	0.99	0.48	0.93
Dec-Jan	45	0.70	0.95	0.31	0.95	0.48	0.91
Mar-Apr	45	0.77	0.97	0.74	1.04	0.70	1.04
Sept-Apr	169	0.79	0.97	0.72	1.00	0.77	0.98

Comparison on a monthly basis shows that at the Ndabibi site, the lowest $r^2 = 0.23$ in the December-January months for the 5-day extrapolation case. At Eburu, the December-January period also gave the worst comparison with an $r^2 = 0.31$ for the 3-day extrapolation case. The reason for this is that January and December are relatively drier and there are periods of rapid changes in soil moisture. In the estimation of r_s it is assumed that soil moisture is constant for 1, 3 or 5 days. It is therefore expected that during rapid changes of soil moisture there will be poorer estimates of E .

The difference, in percentage, between predicted and measured accumulated E for the whole study period is presented in Table 6.4. Very good results are obtained for the all 3 case analyses. The largest difference is 2.9% for the 5-day case at the Eburu site. This shows that this method can be useful to give accurately E totals under all weather conditions for applications which require long-term E totals. The percentage difference between predicted and measured monthly accumulated E are larger (not shown). The largest difference is 9.8% for the period of September-October for the 5-day case at the Eburu site.

Table 6.4: The percentage difference between accumulated evaporation E (mm) measured by the Bowen ratio surface energy balance and predicted from the Penman-Monteith and Jarvis-Stewart models model and weather data. (There were 169 days at both sites).

Site	Total measured E	1 day case		3 day case		5 day case	
		Total predicted E	% difference	Total predicted E	% difference	Total predicted E	% difference
Ndabibi	152.6	150.8	1.1	152.0	0.3	152.2	0.2
Eburu	196.5	192.6	2.0	194.1	1.2	190.8	2.9

Evaporative fraction

The results of the method using evaporative fraction A in estimating E , are shown in Tables 6.5 and 6.6 for the Ndabibi and Eburu sites respectively. The r^2 and RMSE for the whole study period indicate good agreement between estimated E and measured E for all three extrapolation cases. The mean predicted daily E and mean measured daily E are less than 8% for all the extrapolation cases, as indicated by the slope of the regression lines through the origin.

Table 6.5: Comparison of daily evaporation E measured by the Bowen ratio surface energy balance method and predicted by the evaporative fraction method at the *Ndabibi* site. The regression lines are through the origin.

Period	No. of days	r^2	Slope	r^2	Slope	r^2	Slope
		1-day case		3- day case		5-day case	
Sept-Oct	18	0.58	0.92	0.13	0.98	0.12	0.98
Oct-Nov	35	0.59	0.90	0.46	0.92	0.18	0.86
Nov-Dec	26	0.48	0.85	0.10	0.78	0.07	0.83
Dec-Jan	45	0.38	0.65	0.15	0.55	0.35	0.55
Mar-Apr	45	0.75	1.04	0.67	1.04	0.60	1.03
Sept-Apr	169	0.81	0.97	0.75	0.96	0.63	0.98

Table 6.6: Comparison of daily evaporation E measured by the Bowen ratio surface energy balance method and predicted by the evaporative fraction method at the *Eburu* site. The regression lines are through the origin.

Period	No. of days	r^2	Slope	r^2	Slope	r^2	Slope
		1-day case		3- day case		5-day case	
Sept-Oct	18	0.42	1.03	0.31	1.00	0.54	1.08
Oct-Nov	35	0.82	1.07	0.82	1.06	0.90	1.03
Nov-Dec	26	0.50	1.09	0.15	1.10	0.12	1.02
Dec-Jan	45	0.51	1.14	0.42	1.17	0.48	0.16
Mar-Apr	45	0.54	1.00	0.60	1.08	0.50	0.95
Sept-Apr	169	0.71	1.06	0.64	1.08	0.70	1.04

Considering monthly periods, the RMSE varies from 0.14 mm to 0.41 mm. However the r^2 are low for the 3 and 5-day extrapolation cases, especially at Ndabibi, for the months of November, December and January. This is illustrated in Fig. 6.4 where there is a lot of scatter in the plot of measured and estimated E for the 5-day extrapolation case at Ndabibi for the December-January period. The differences between the

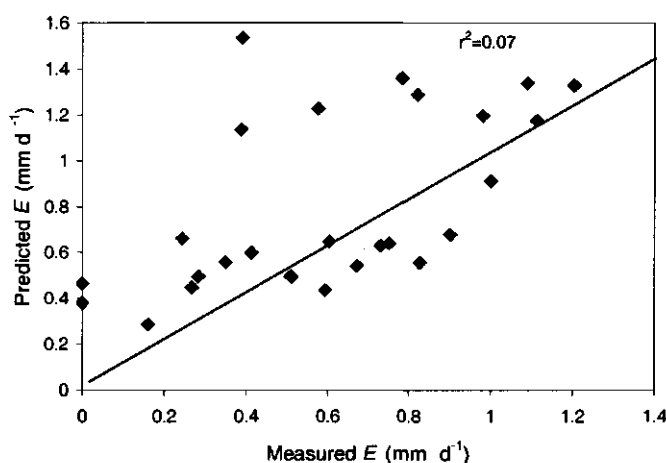


Fig.6.4. Comparison of measured daily evaporation E and predicted from the evaporative fraction method for the 5-day extrapolation case at the Ndabibi site for the period November-December 1998

estimated and measured E for individual days can be more than 100 %. This indicates that the evaporative fraction method may not be suitable for the 3 and 5 day extrapolation when daily E values are required.

The daily E values were summed over a week to test whether better comparison could be obtained for the 3 and 5-day extrapolation cases. Figure 6.5 shows the comparison of 7-day totals of E at the Ndabibi site. It is clear that very good estimates of E can be obtained if E is summed over a week. Similar results were obtained for the Eburu site.

The difference between predicted and measured accumulated E for the whole study period is shown in Table 6.7. The best agreement is 1.1% for the 5-day extrapolation case at the Ndabibi site, while the largest difference is 8.8% for the 3-day extrapolation case at Eburu. This implies that long-term E totals can be accurately obtained under all conditions by the evaporative fraction method.

Discussions

The extrapolation of E values by the PM equation and JS type of models, depends on how much the soil moisture varies from day to day. Figure 6.6 demonstrates that changes in h_{rw} are mostly gradual. However there are a few periods when temporal changes are significant. For example in response to rainfall events, h_{rw} changes from -2300 cm to -1000 cm between 29 and 30 January. Large errors would be expected if the value of h_{rw} on 29 January is used in the calculation of r_s on the following days. Such errors due to step changes in moisture availability could be diminished if daily rainfall was available and, together with estimated E , a simple soil moisture balance could be made to give an approximate idea of the soil water moisture dynamics over a year and hence the times of expected large-step changes.

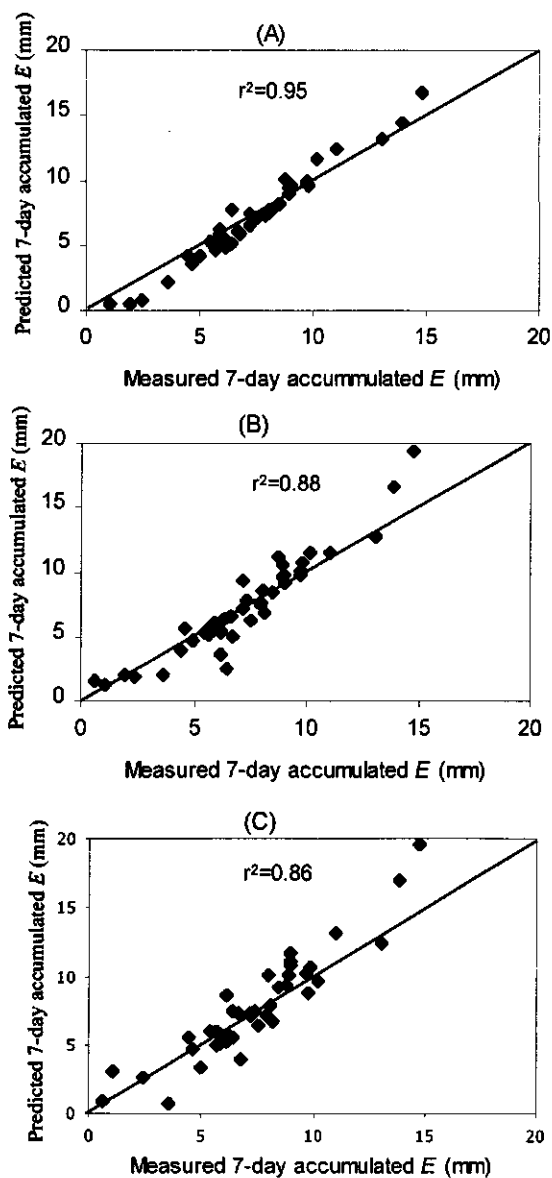


Fig.6.5. Comparison of 7-day accumulated evaporation E , predicted by the evaporative fraction method and 7-day E measured by the Bowen ratio method: (A) 1-day extrapolation case, (B) 3-day extrapolation case and (C) 5-day extrapolation case

Table 6.7: The percentage difference between accumulated evaporation E (mm) measured by the Bowen ratio surface energy balance and predicted from the evaporative fraction method. (There were 164 days at both sites).

Site	Total measured E	1 day case		3 day case		5 day case	
		Total predicted E	% difference	Total predicted E	% difference	Total predicted	% difference
Ndabibi	152.6	144.8	5.1	145.6	4.6	150.9	1.1
Eburu	196.5	213.0	8.4	213.8	8.8	206.5	5.1

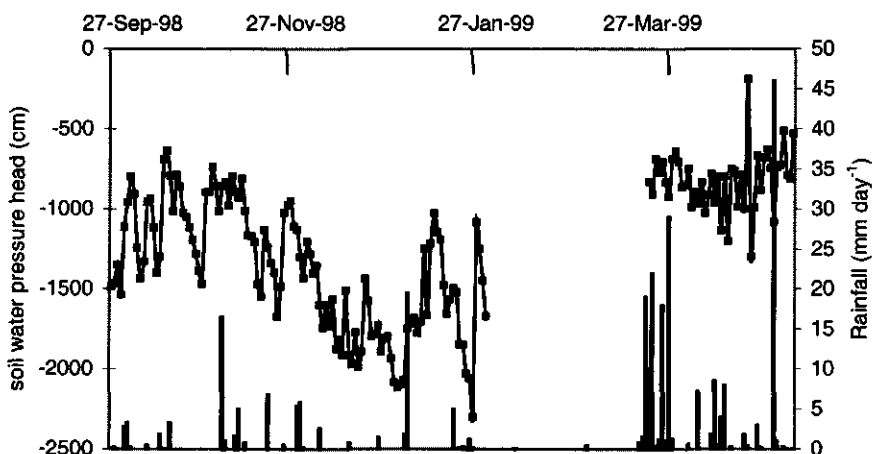


Fig.6.6. Seasonal evolution of average daily soil water pressure head h_{rw} and daily rainfall (bars) from 27th September 1998 to 24th April 1999 at the Ndabibi site

The Jarvis–Stewart surface resistance models implicitly account for soil evaporation if the coefficients are optimized using measured total evaporation. In this study r_s is obtained from the inversion of the *PM* equation by using total evaporation measured over the canopy, hence soil evaporation is accounted for. However, theoretically the r_s models are limited to periods when canopies are dry. In the present study, all days were considered irrespective of canopy wetness conditions. It appears this did not affect the extrapolation of E very much, possibly due to the low interception of rain by the grass and bushes found in the study sites. The other reason could be the limitation of the analyzed data to between 9.00 and 16.00 hrs, during which time dry canopies are prevalent. Most of the rainfall occurs in the late afternoon. Other researchers have also obtained good results for E by using r_s models with general data having no distinction in canopy wetness conditions (e.g. Dolman et al., 1991; De Rooy and Holtslag, 1999). However, in the forested areas interception losses may be significant. Wet canopies are expected more frequently due to higher rainfall and dew formation on the high grounds. This has to be accounted for if reliable E estimates for the forested areas on high grounds are to be obtained.

The basis of using λ in the extrapolation of E depends on how much it varies from day to day over a season. Hall et al., (1992), in an extensive study of the evaporative fraction in a grassland area under the FIFE project, suggest that due to the gradual changes of λ in as season, it can be monitored once every 5 to 10 days. Farah et al. (2000) demonstrated that the seasonal evolution of λ at the Ndabibi and Eburu sites is gradual and that the daily average fluctuations are larger during dry periods than during wet periods. This is clearly shown in Tables 6.2 and 6.3 where the dry months of December and January give an r^2 of 0.15 and 0.42 at Ndabibi and Eburu respectively for the 3-day extrapolation case. It can also be seen that there is an underestimation of E of 45% at Ndabibi (slope of regression line is 0.55) and an overestimation at Eburu of 16% (slope of regression line is 1.16). However, this may not have a serious effect on the accuracy of E estimation on a seasonal basis because during most of this period E is very low and close to zero. Farah et al. (2000) also observed that the seasonal variations of λ are more stable in woodland areas than in grassland areas because the deeper rooted vegetation in the woodlands continues to transpire during the dry down period of the upper soil layers. *This suggests that the evaporative fraction method could be used in the extrapolation of E in the forested areas where the r_s model may not produce satisfying results, as noted earlier.*

With regard to cloud cover, given the conditions in the study area in Kenya and the requirement of a satellite scene with less than 20% cloud cover for a study area, 5-day extrapolation may be required if daily E values are needed. Although the daily values of E obtained from the 3 and 5-day extrapolation of λ do not give reliable results especially at Ndabibi, it is encouraging that good results of 7-day accumulated E can be obtained by merely assuming that λ is constant for up to 5 days. This has important implications for applications that require 7 day or longer E values. The simplicity and suitability of applying the λ in remote sensing methods are appealing for operational regional monitoring of E . Spatially distributed λ can be obtained from cloud-free satellite images. Between 2 consecutive cloud-free images, λ can be interpolated and used to determine E assuming that daily R_n is available. Furthermore, Farah et al. (2000) showed that routine weather data could be used to estimate 10-day or monthly average λ over a season. Many applications in hydrology can benefit from these methods. While the present method can be used to predict accumulated E on shorter term (7 days), the method described by Farah et al (2000) could be used to predict accumulated E over longer seasonal periods.

The practical implementation of the procedures presented above for extrapolating E at a catchment or river basin will require the following strategies. The catchments should be first divided into homogeneous units. The delineation of a catchment into hydrologically similar units can be done with the aid of high resolution satellite data such as Landsat TM (e.g. Farah and Bastiaanssen, 2000). In each of the units, the JS model should be calibrated so as to obtain suitable coefficients for the functions in Eq. 6.2. Standard weather data (air temperature, humidity and wind speed) will have to be collected on a daily basis at each unit. The A method requires daily net available energy for each unit but this quantity can be estimated from the meteorological data (e.g. Holtslag and van Ulden, 1983).

6.4 Conclusions

The objectives of this chapter was to investigate suitable methods of determining E during periods of non-availability of satellite data, ranging from a single day to a maximum of 5 days, in regional E monitoring studies. The following conclusions can be drawn from the present study.

The JS models can provide reliable estimates of daily values of E when used for up to 5 continuous days with cloud cover, assuming constant soil water pressure head h_{rw} . A simple correction for rainy periods is possible. The PM equation and JS models are therefore suitable for filling in missing daily E data in long-term monitoring of E .

When the whole study period is considered, the A method of extrapolating E predicts average daily E to be within 8% of measured E . However, on individual days the predicted E may differ from measured E by more than 100% for the 3 and 5-day extrapolation cases. This indicates that during continuous cloud cover of up to five days the evaporative fraction method may not give reliable daily E values. Good results are obtained if E is summed over 7-day periods. For applications that require 7-day E , the simple evaporative fraction method is recommended.

Chapter 7

The temporal evolution of daily actual evaporation with NOAA AVHRR satellite and ground data in the Naivasha basin*

7.1 Introduction

Knowledge of evaporation is required for several purposes in the Naivasha study basin and in Kenya in general. A number of river basin authorities have been set up in Kenya in the last decade which are now at different stages of making basin plans and water resources allocation. The planning and allocation of water resources require knowledge of water users in the basin and the setting up of hydrological models of the basin. Evaporation E is required over large areas with different land use and cover. Hydrological models need information on E at daily, monthly or annual time scales depending on the purpose of the modeling. Rainfall-runoff and groundwater modeling require daily estimates of E as input to the models. Evaporation estimates may also be required for the verification of the models. Monthly values of E are needed for water balance studies, while annual estimates of E are needed for water scarcity studies. In irrigation management, information about crop water requirements is required in advance for water schedule planning. Daily monitoring of crop stress through evaporation mapping can provide irrigation managers with water requirement information.

The operational use of remote sensing for monitoring daily actual evaporation requires the temporal integration of E over a season or year. Satellite spectral measurements provide suitable estimates at the regional scale, but they are obstructed by clouds and hence not available on daily basis. Therefore a method is required to estimate E on cloudy days between intermittent clear days with satellite images. In this Chapter the Penman-Monteith and Jarvis-Stewart models will be tested with actual remote sensing data. The simplified method of evaporative fraction λ to predict E will also be tested with remote sensing data to circumvent the need to solve the surface resistance r_s and aerodynamic resistance r_{ah} . The

* Based on: H.O. Farah and R.A. Feddes. 2000. The temporal evolution of daily actual evaporation with NOAA AVHRR satellite and ground data (*in preparation*).

objective is to demonstrate the mapping from NOAA AVHRR satellite data of spatial variations and temporal evolution of E in a heterogeneous landscape and under all weather conditions.

7.2 Material and methods

Satellite data

Five satellite images of NOAA AVHRR on clear days were acquired from a public domain site on the internet (<http://www.saa.noaa.gov>). The characteristics of NOAA AVHRR data are shown in Appendix A. The dates of the images, which cover the entire Naivasha catchment, are 20, 25, 27, 30 January and 3 February 1999. This period coincides with the *in situ* field data collection period.

Radiometric calibration and geometric corrections were performed according to the NOAA AVHRR reference guide (Kidwell, 1998). A program developed at the International Institute for Aerospace Survey and Earth Sciences in the Netherlands was used for this purpose (Gieske, personal communication). The images were checked for cloud contaminated-pixels by using cloud detection algorithms (Saunders and Kriebel, 1988). The pixels with cloud contamination were not used for the calculation of E . Atmospheric correction of the planetary broad band albedo was performed using a simple linear relationship between broad surface and planetary albedo (see Eq. 4.1). The split windows procedure was used to correct the thermal bands for atmospheric effects (Varlor and Caselles, 1996). The temperature contrast between the thermal bands 4 and 5 is proportional to the amount of water vapour and this information is used to atmospherically correct the thermal bands. Thermal infrared remote sensing algorithms ascribe differences in surface temperature to variations in sensible heat flux. However, in mountainous areas differences in temperature are also due to differences in elevation. The thermal bands were therefore corrected for the influence of elevation by using a digital elevation model of the area and a lapse rate of $6.5^{\circ}\text{C km}^{-1}$.

The Surface Energy Balance for Land (SEBAL) algorithm was selected to estimate E from the remote sensing images (Bastiaanssen et al., 1998a; Farah and Bastiaanssen, 2000). SEBAL is a one-layer resistance scheme which uses surface albedo r_0 , $NDVI$ and surface temperature T_0 to determine E . This algorithm meets the requirement of accounting for the spatial variability of the main input

parameters elaborated in Chapter 4 and is required to determine E in a heterogeneous landscape. The steps followed in Chapter 4 in retrieving E from remotely sensed data were used with the NOAA AVHRR images and will not be repeated here.

Determination of surface resistance and soil water pressure head

The surface resistance, r_s was obtained for each pixel in the image from inversion of the Penman-Monteith (PM) equation (see Fig. 6.1).

$$r_s = \left[\left(\frac{s(R_n - G_o) + \rho c_p \Delta e / r_a}{\lambda E} - s \right) / \gamma - 1 \right] * r_{ah} \quad (7.1)$$

The output of the SEBAL algorithm is instantaneous values of E , r_{ah} , R_n , H and G_o for each NOAA AVHRR pixel. The inversion of the $P-M$ equation requires information on the saturation vapour pressure deficit Δe and the slope of the saturation vapour pressure curve, s . This information was available only at the Ndabibi and Eburu field stations. Air temperature T_a and relative humidity RH from which Δe and s are calculated, vary with elevation. A digital elevation model of the Naivasha catchment was prepared from topographic maps of the area. The T_a and RH values from the two experimental stations were used to establish linear relationships between elevation and T_a and RH . These simplified relationships were used to estimate the T_a and RH for each NOAA AVHRR pixel, depending on its elevation. Thereafter Δe and s were calculated using standard expressions such as provided by Allen et al., 1998.

The soil water pressure head h_{rw} , was obtained by inversion of the Hanan-Prince model Eq. 6.1:

$$F_4(h_{rw}) = \frac{r_{s \min}}{r_s LAI F_2(T_a) F_3(\Delta e)} \quad (7.2)$$

and Eq. 6.4:

$$h_{rw} = (F_4(h) - 1)(h_{\max} - a_5) + h_{\max} \quad (7.3)$$

The Hanan-Prince model is a Jarvis-Stewart type of model and was found to be valid for the grassland and bushland experimental sites, which had similar conditions as the area for which it was originally calibrated during the HAPEX-Sahel experiment in Niger. Since the objective here is to show the practical application of the Jarvis-Stewart type of models to satellite data, the Hanan-Prince model was applied to the whole catchment although other land use classes occur. Furthermore, it should be noted that the Hanan-Prince model was used twice, i.e. in the inverse and forward modes, and therefore errors in h_{rw} and E prediction due to empirical coefficients are expected to be minimized. The surface resistance and the meteorological parameters as obtained above were used to calculate h_{rw} for every pixel in the image. LAI is derived from NDVI obtained from the satellite images.

Estimation of surface resistance under cloud covered conditions

On cloudy days the surface resistance r_s was determined from the Hanan-Prince model using h_{rw} calculated from the previous satellite image on a clear day and from Δe and T_a calculated for each pixel from the measurements at the Ndabibi and Eburu stations extrapolated across the basin using the digital elevation model. In this case however, daily average meteorological parameters were used. The net daily shortwave radiation flux density was obtained from r_0 of the last image and the measured incoming shortwave radiation flux density $K\downarrow$ integrated over 24 hours.

Due to similarity in cloud duration conditions of areas with similar elevation, $K\downarrow$ at Eburu was assigned to pixels above an altitude of 2000 m and values at Ndabibi were used for pixels below 2000 m. The net longwave radiation flux density was evaluated from T_a and RH , using empirical functions (e.g. Allen et al., 1998). The aerodynamic resistance r_{ah} , depends on local wind speed and momentum fluxes and can be determined from wind speed measurements and land surface characteristics. Due to the absence of this information in the basin the r_{ah} values from the Ndabibi site were used for pixels with an elevation of less than 2000 m and the r_{ah} values from the Eburu site were used for pixels with an elevation of more than 2000 m.

For comparison with alternative solutions for the time integration of E , evaporation was also predicted by the Λ method. To obtain daily evaporation E_{24} , the Λ of each pixel from the last NOAA AVHRR image was multiplied by the estimated daily net radiation R_{n24} , for each pixel during cloudy periods without satellite data ($E_{24} = \Lambda_{inst} R_{n24}$). This simplified and pragmatic approach is worth testing for use in operational applications.

7.3 Results and discussion

Evaporation for four land units during clear days with the satellite images

On the basis of a land cover map obtained from high resolution Landsat image, the NOAA AVHRR images were classified into four broad units. Unit 1 coincides with forests on the high grounds with characteristically high NDVI, low r_0 and low T_0 . Unit 2 represents open water bodies such as Lake Naivasha. The low-lying plains inside the rift valley mainly covered by grassland and bushlands are grouped into Unit 3. Cropland and woodland on the escarpments and plateaus on the eastern and western sides of the study area appear to be in Unit 4.

Figure 7.1 shows the spatial variations of E on 27 January, 1999 in the Naivasha catchment and demonstrates the heterogeneity of the Naivasha catchment with large contrast in E . To gain more insight into the temporal evolution of E , the daily E at sample sites in the four units was monitored. The values of E at the four land cover units over the five clear days are presented in Fig. 7.2. The pattern of the variations of E is as expected. On all days, E from Unit 2 (open water) is highest, followed by Unit 1 (forests). The lowest E on these days occurs at Unit 3 (grassland). The high evaporation from Units 1 and 4 was not expected during the month of January, which coincides with the beginning of the dry season. The reason for this may be attributed to the extended rooting depth of the vegetation here, which enables root water uptake from deeper soil layers. The average total catchment E_A during this period of the year is about $5.3 \times 10^3 \text{ m}^3 \text{ d}^{-1}$.

The validation of remotely sensed E , especially from low-resolution satellite data such as NOAA AVHRR, with field measurements is not a straightforward matter. The upper and lower limits of E as indicated by Unit 2 (open water) and Unit 3 (grassland) are compared with E as calculated by the energy balance method at Lake Naivasha and field measured E at the Ndabibi site respectively (see Table

7.1). The Ndabibi site is located in an extensive flat homogeneous grassland (see Fig. 3.1) and is therefore suitable for validation purposes. The satellite pixels at the position of the Eburu station were composed of mixed woodland, cropland and forestland covers. It was technically difficult to install towers over the forest and moreover permission was not granted from the concerned authorities to work in the forest. The field measurements at the Eburu site could not therefore be used for comparison with the satellite measurements of heterogeneous pixels of 100 ha.

The average of 4 pixels in the images of the area surrounding the position of Ndabibi station, was calculated. The average difference between measured and remotely sensed E is 27%. This percentage may appear to be large but the absolute difference is 0.58 mm and such order of deviations are within the uncertainties in E measured by the Bowen ratio. On most of the days, the E derived from NOAA AVHRR is higher than the field measured values of E . It should be noted that the values of E from the field measurements based on the Bowen ratio method are totals obtained between 9.00 and 16.00 hours while the satellite derived E are 24 hour totals. Evaporation E from Lake Naivasha by remote sensing and E estimated from the energy balance method (Ashfaq, 1999) compare well, the average difference being 8%. However on all days, the remotely sensed E is slightly higher than the values of E calculated by the energy balance method. There appears to be a slight bias towards over-estimation of E by the SEBAL algorithm. Note that SEBAL application on cloud free days is based on a temporal constancy of Λ . A possible explanation for this is that some images were taken later than 15.30 hrs. At this time, the evaporative fraction Λ is usually higher than the average for the day and therefore its use to integrate the daily E may lead to an overestimation of E values.

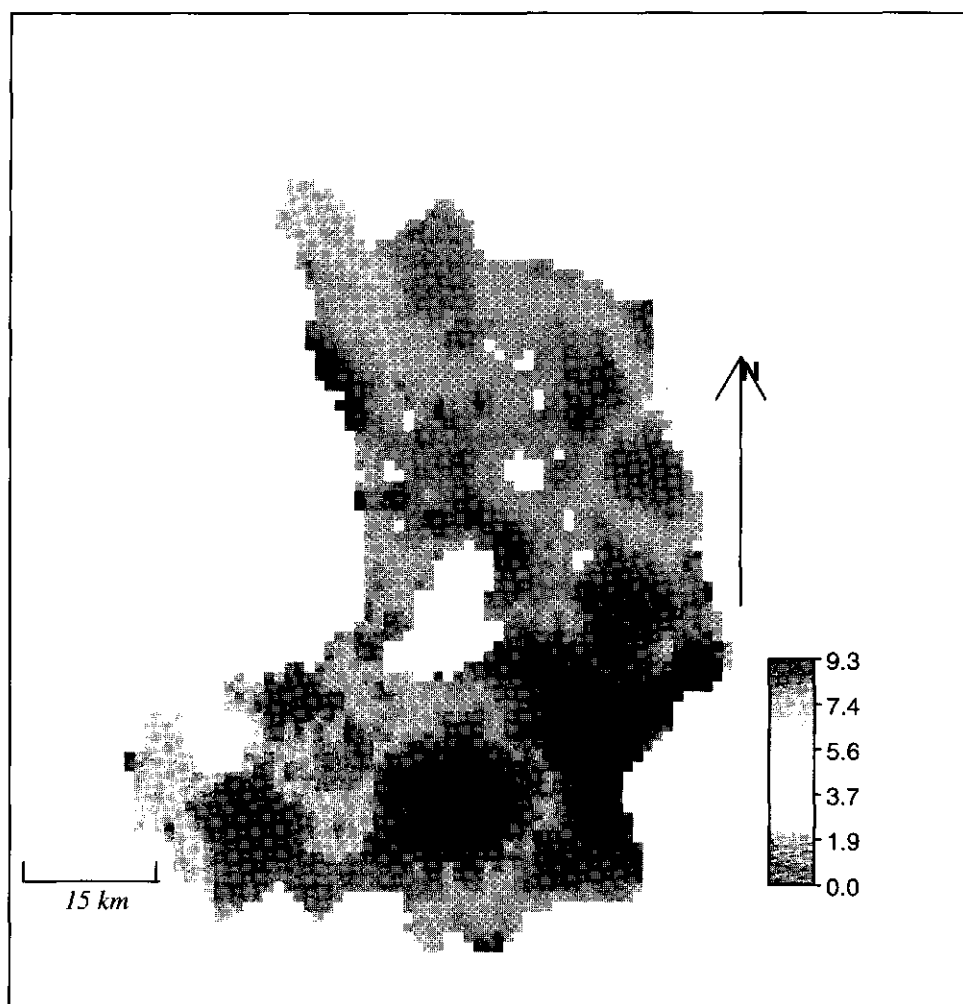


Fig.7.1 The spatial patterns of evaporation E (mm d^{-1}) in the Naivasha catchment on 27 January 1999. The white patches in the image are clouds (color version in Appendix B)

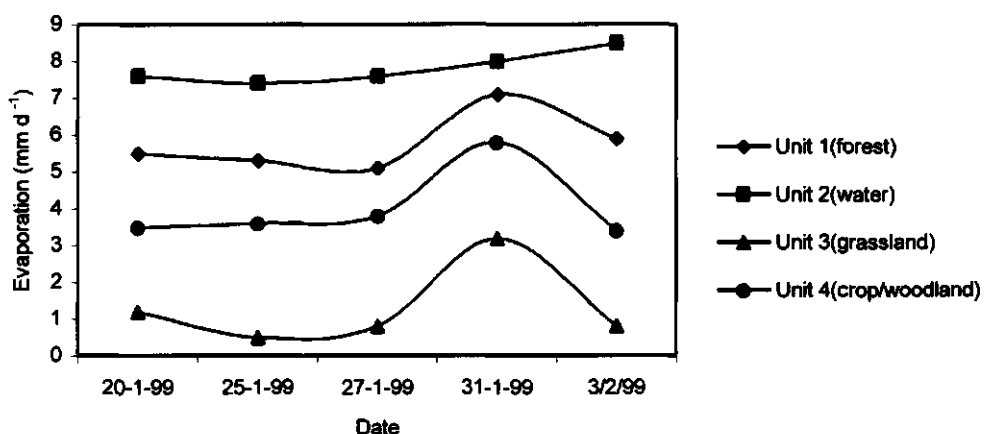


Fig.7.2: The temporal variations of evaporation E at four land units obtained during five clear days from NOAA AVHRR satellite images

Table 7.1: Validation of evaporation (mm d^{-1}) derived from NOAA AVHRR at Unit 3 (grassland) and Unit 2 (water body) with evaporation from field measurements at Ndabibi station and calculated with energy balance method.

Date/Unit measurement	Unit 3	Field measurement	Unit 2	Field
20-1-99	1.2	0.93	7.6	6.3
25-1-99	0.5	0.86	7.4	7.4
27-1-99	0.8	0.00	7.6	7.5
31-1-99	3.2	1.20	8.0	7.4
3-2-99	0.8	0.60	8.5	7.2

Surface resistance and soil water pressure head for clear days with satellite images

Figure 7.3 illustrates the spatial variations of r_s and h_{rw} on 27 January 1999. Table 7.2 shows the values of r_s and h_{rw} for Units 1, 3 and 4 for the days with available images. The values of r_s were compared with those reported in the literature. Kabat et al. (1997) reported r_s values obtained during the HAPEX-Sahel experiment which was carried out in the rainy season. They reported r_s to be between 40 and 200 s m⁻¹ for woodland areas. The values of 143 s m⁻¹ obtained at Unit 4 after a rainfall event appear to be within the reported range. For grassland, Kabat et al. (1997) reported r_s values of between 100 and 500 s m⁻¹. At Unit 3, a value of 202 s m⁻¹ similarly occurring after rainfall seems to be reasonable. The average r_s during the two-week period at Unit 1 is 140 s m⁻¹, which compares with an average value of 166 s m⁻¹ as reported by Dolman et al. (1993) for a tropical forest. The values of h_{rw} appear reasonable as the lowest values coincide with Unit 3 and the highest with Unit 1.

Table 7.2: Surface resistance r_s and soil water pressure head h_{rw} obtained from the inversion of the Penman-Monteith and Jarvis-Stewart type models respectively at Unit 1(forest), Unit 3 (grassland) and Unit 4 (crop/woodland) on clear days with NOAA AVHRR images available.

Date	r_s (s m ⁻¹)			h_{rw} (cm)		
	Unit 1	Unit3	Unit 4	Unit 1	Unit 3	Unit 4
20-1-99	120	260	142	-357	-1500	-367
25-1-99	171	975	690	-459	-1548	-1136
27-1-99	252	1340	691	-628	-1651	-1203
31-1-99	57	202	143	-301	-865	-447
3-2-99	120	848	736	-342	-1690	-1100

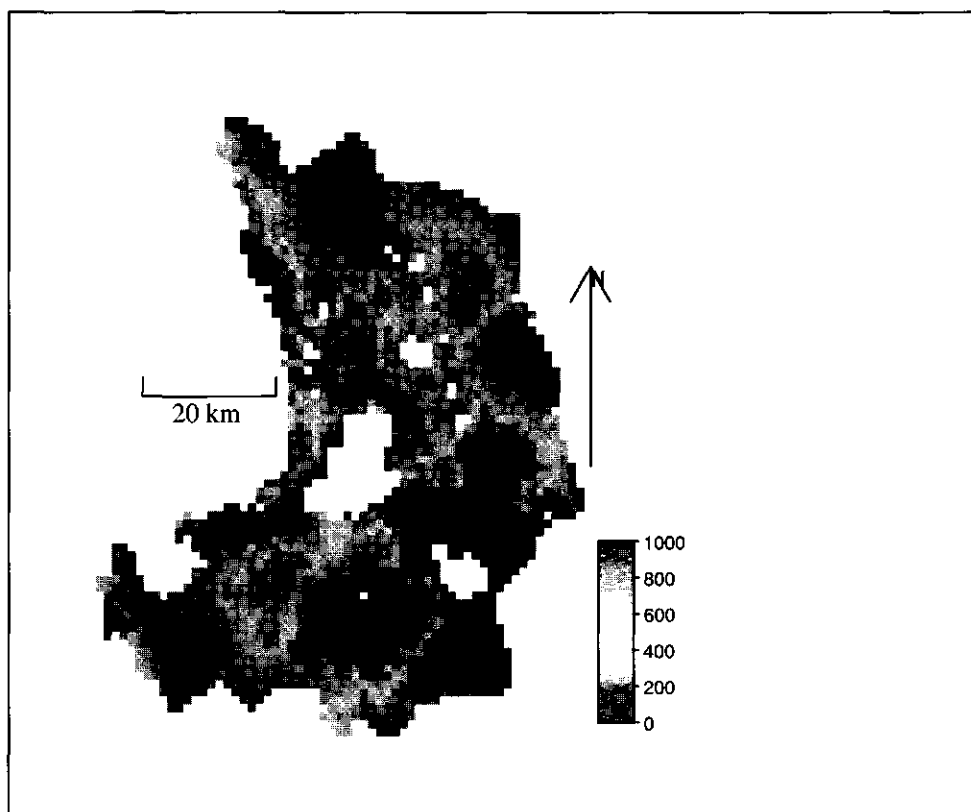


Fig. 7.3a. The spatial patterns of surface resistance r_s ($s\ m^{-1}$) in the Naivasha catchment on 27 January 1999 (see color version in Appendix B)

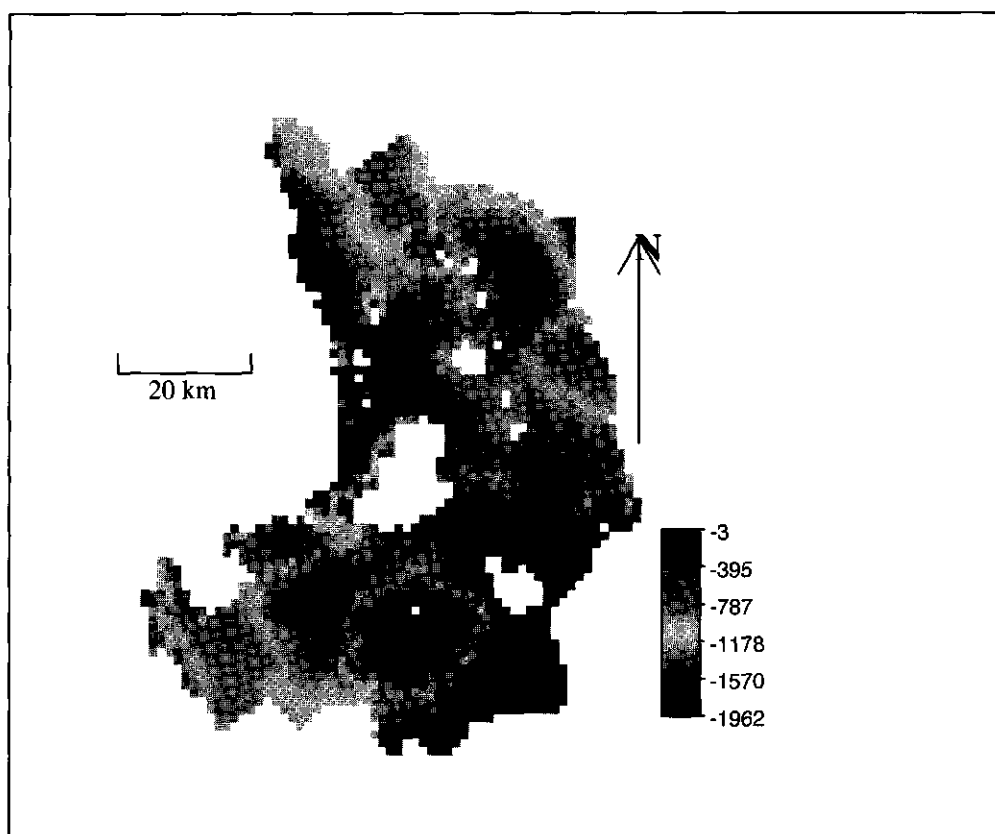


Fig. 7.3b. The spatial patterns of soil water potential head h_{rw} (cm) in the Naivasha catchment on 27 January

Evaporation is controlled by atmospheric and land surface conditions. These environmental conditions are expressed by means of the functions $F_2(T_a)$, $F_3(\Delta e)$ and $F_4(h_{rw})$ and the influence of r_{smin} by solar radiation. The influence of these functions on E in the Naivasha catchment was described by delineating areas being controlled by soil moisture θ , Δe and T_a . Such delineated maps reveal the types of stresses in the different parts of the catchment. Table 7.3 presents the values of the reduction functions, $F_2(T_a)$, $F_3(\Delta e)$ and $F_4(h_{rw})$ in the Hanan-Prince model for the forest and grassland units.

The values of the functions indicate that at Unit 3 (grassland), θ is the limiting factor for evaporation, whereas T_a is the most limiting at Unit 1 (forest). It appears that the effect of soil moisture in the forest areas was important on 27 January. The value of $F_4(h_{rw})$ is 0.59, indicating that this function needs to be considered for all the units. There is little temporal variation in the T_a function at Unit 3. This shows that during this period the day-to-day variations of T_a at Unit 3 were small.

Table 7.3: The values of the reduction functions $F_1(T_a)$, $F_2(\Delta e)$ and $F_3(h_{rw})$ at Unit 3 and Unit 1 during the clear days when satellite images were available

Date (h_{rw})	Unit 3 (grassland)			Unit 1 (forest)		
	$F_1(T_a)$	$F_2(\Delta e)$	$F_3(h_{rw})$	$F_1(T_a)$	$F_2(\Delta e)$	$F_3(h_{rw})$
20-1-99	0.82	0.69	0.15	0.61	0.76	0.92
25-1-99	0.85	0.62	0.08	0.72	0.78	0.76
27-1-99	0.83	0.59	0.10	0.52	0.73	0.59
31-1-99	0.84	0.62	0.49	0.72	0.74	1.00
3-2-99	0.83	0.65	0.14	0.65	0.88	0.92

Evaporation from the Penman-Monteith equation and Jarvis-Stewart type model on cloudy days without satellite images

Evaporation maps were produced for the entire Naivasha catchment at the NOAA AVHRR pixel scale for all the days in between the dates that satellite images were available. The temporal evolution of E for Units 1, 3 and 4 for the two weeks, from 20 January to 3 February 1999 is presented in Fig. 7.4. This figure demonstrates the large variations of E both in space and in time in the Naivasha basin. The highest E of 8.5 mm d^{-1} occurred on 31 January at Lake Naivasha and the lowest was 0.40 mm on 30 January at the grassland areas (Unit 3). The largest difference in E within a given unit during the 2-week period is 3.7 mm at the cropland/woodland areas (Unit 4). The highest E in all the units occurred on 31 January in response to a rainfall event recorded at the two field stations.

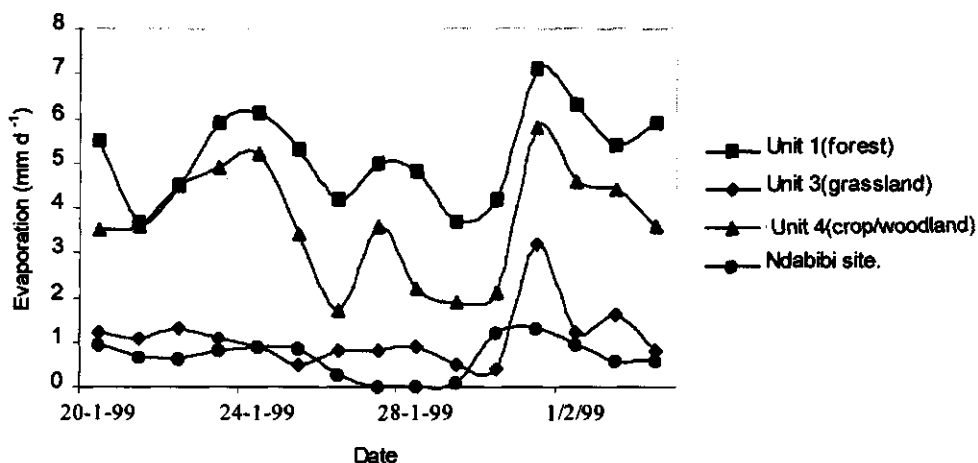


Fig.7.4: The temporal evolution of evaporation E estimated from NOAA AVHRR images on *clear* days and the Penman-Monteith equation and Jarvis-Stewart type models for 3 land units in the Naivasha catchment on *cloudy* days

It was observed that at all the Units, E on clear days with satellite images was generally higher than on the other days. For example, the average E for Unit 1 for the five days with satellite images was 5.8 mm, whereas the average E for the other 10 days was 4.7 mm. This may be attributed to the fact that the days on which images are acquired are clearer, with a resulting higher net available energy for evaporation. *This implies that basing the time integration of E or the calculation of average daily E from few available satellite images may give erroneous results as only relatively high E are sampled.*

Evaporation from the evaporative fraction method

Figure 7.5 illustrates the spatial variations of λ in the Naivasha catchment on 27 January 1999. The evaporative fraction λ , varies from 0 to 1, indicating large differences in soil moisture conditions in the catchment. In the parameterization of the SEBAL algorithm, λ of lake Naivasha was set to 1. On 27 January more than 70% of the catchment had a value of $\lambda > 0.5$.

Figure 7.6 shows the average values of λ for Units 1, 3 and 4 as derived from the 5 satellite images. The day-to-day variations of λ for Unit 1 is small compared with those for the other units, demonstrating little temporal changes in soil moisture in the forested high grounds. The evaporative fraction changes from 0.11 to 0.42 at Unit 3 during the two-week period, however, the evolution of λ is gradual.

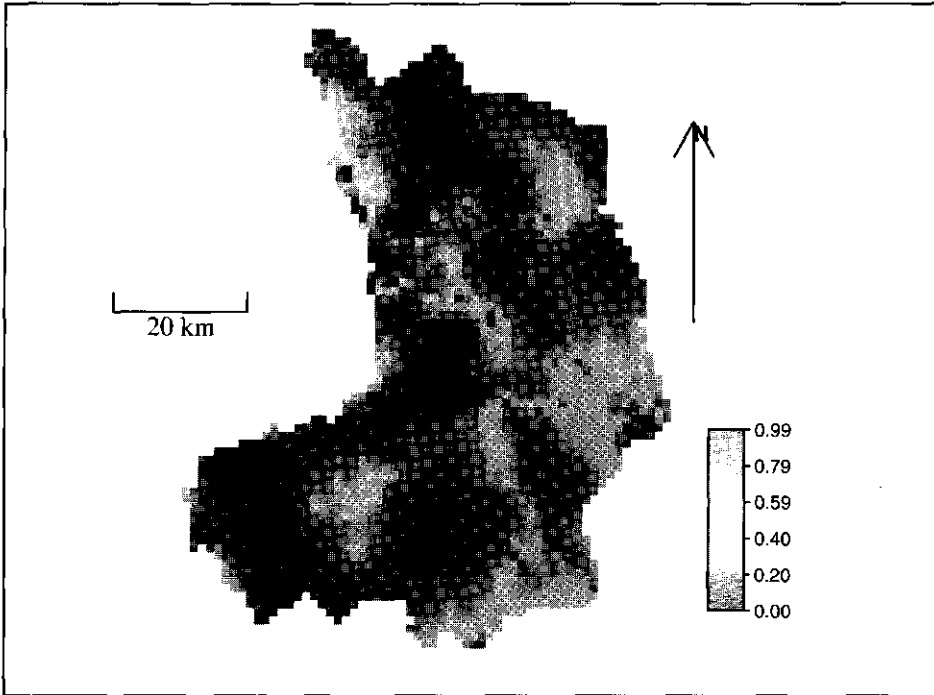


Fig. 7.5. The spatial patterns of the evaporative fraction A in the Naivasha catchment on 27 January 1999 (see color version in Appendix B)

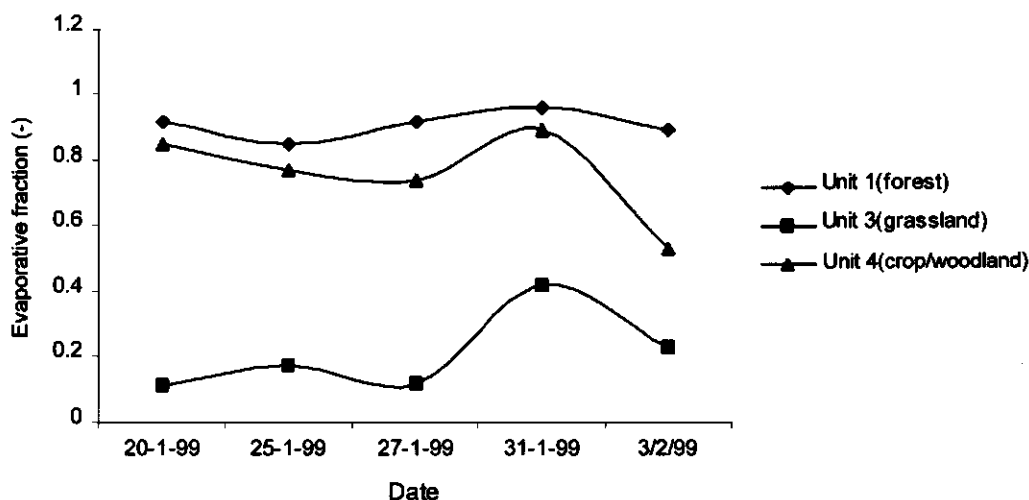


Fig.7.6: The temporal changes of evaporative fraction Λ derived from the 5 NOAA AVHRR images on *clear* days for three land units

The prediction of E by the Λ method for cloudy days without satellite data is presented in Fig. 7.7. Comparison of predicted E at Unit 3 with the measured E at the Ndabibi site reveals that the predicted values of E are mostly higher than the measured values, particularly after 31 January. The average daily difference was 0.67 mm. Although the measured value of E is the total between 9.00 and 16.00 hrs, whereas the predicted E is the 24-hour total, the overestimation of E cannot be attributed to this difference only. It has already been observed that on most dates the NOAA-AVHRR overpass time was later than 15.30 hrs. The evaporative fraction in the late afternoon is usually higher than the average day Λ , as shown experimentally in Chapter 5. *The use of Λ from the images to estimate E on other days will therefore over-estimate E .* The other reason for the overestimation of E especially in Unit 1, is the use of $K\downarrow$ at the Ndabibi and Eburu stations for the entire catchment. It is expected that the forest on the high ground will have smaller $K\downarrow$ due to more frequent cloud conditions. This means that the R_{n24} used in the prediction of E will result in a higher value of E .

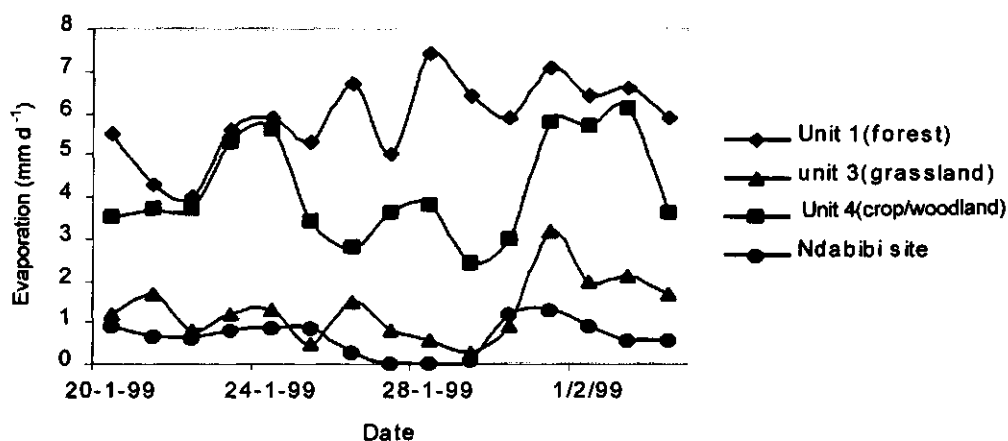


Fig7.7: The temporal evolution of evaporation E estimated from NOAA AVHRR images on *clear* days and the evaporative fraction method on *cloudy* days for the period of 20 January 1999 to 3 February 1999

There is a satisfactory agreement between predicted E by the A method and the use of the PM/JS models. The deviation in daily E is between these two methods is 4%, 10% and 12% for units 3, 1 and 4 respectively. Figure 7.8 shows the cumulative E obtained by the two methods at units 1, 3 and 4. The divergence between the two values begins on 27 January and increases especially, after 31 January. However, the percentage difference between accumulated E during the 15 days is only 11%, 12% and 13% at the Units 4, 1 and 3 respectively.

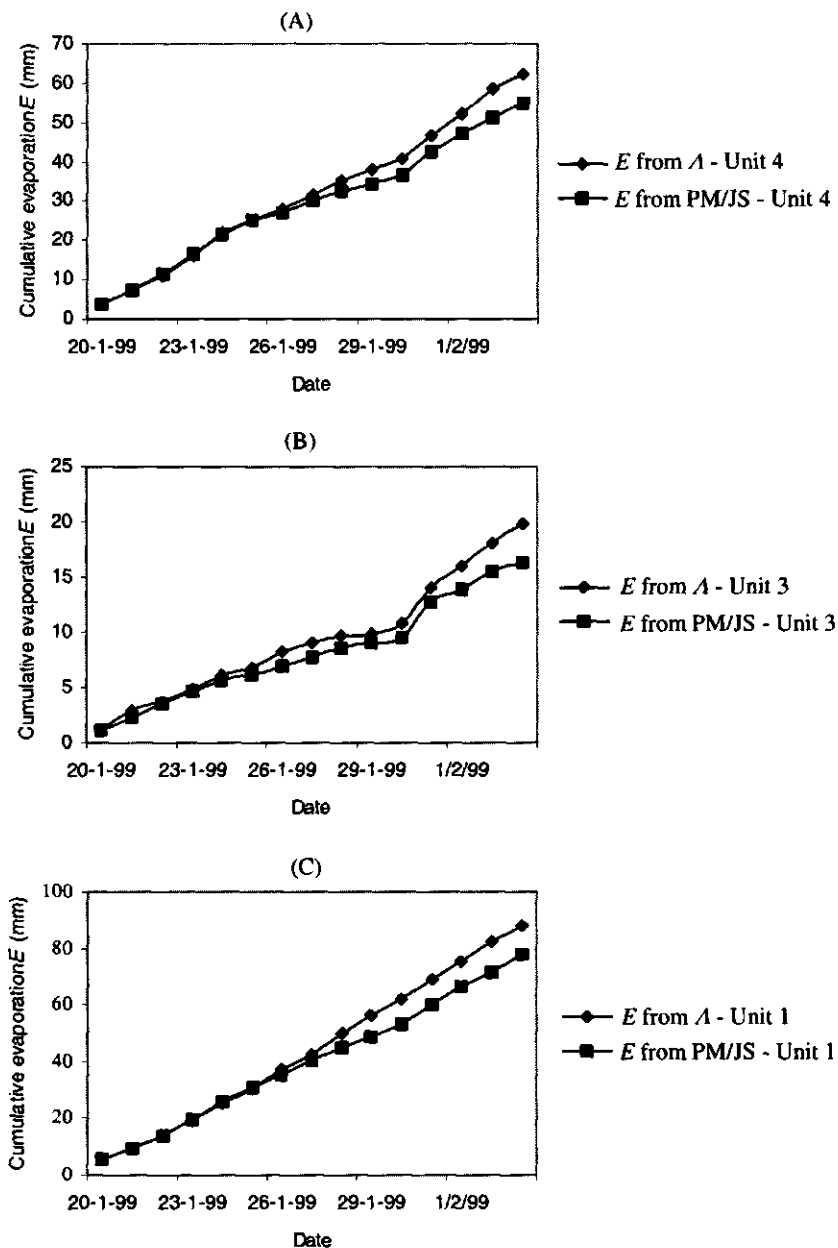


Fig.7.8. Comparison of cumulative evaporation E obtained from the evaporative fraction Λ method and the Penman-Monteith equation and Jarvis-Stewart type model, (A) Unit 3 (B) Unit 1 (C) Unit 4

7.4 Conclusions

The objective of this chapter was to demonstrate the practical application of the methodology developed in Chapter 6 to estimate the temporal evolution of E from NOAA AVHRR satellite images taken on clear days. Evaporation was determined continuously for 15 days. The results show that it is possible to use the *PM* and *JS* type models and Λ in combination with remote sensing data to predict the temporal evolution of E on clear and cloudy days in a heterogeneous catchment. A land cover classification of the catchment and measured standard weather data for the major land cover types are necessary. *The simplified method of Λ requires that Λ be obtained from satellite data acquired during the central hours of the day, otherwise E will be overestimated.*

The new procedure (*PM* equation and *JS* type models) allows the role of environmental parameters related to atmospheric and surface conditions to be described explicitly. Areas in the catchment in which E is controlled by soil moisture, vapour pressure deficit and air temperature could be delineated. *The remote sensing estimates of E on days with satellite data agree with the Bowen ratio in-situ measurements. The procedure developed to predict E on cloudy days gave comparable results with ground measurements (average percent difference of 11%). The simple procedure of Λ is easier to implement in an operational environment and appears to give results comparable to those of the more complex procedure involving the *PM* and *JS* type models. The Λ method is therefore recommended for operational use especially for applications requiring 7-day average or longer E values.*

Chapter 8

Summary and Conclusions

Evaporation E is required for various applications of E in hydrology, agriculture and meteorology. Evaporation E in heterogeneous catchments displays large variations both spatially and temporally. Satellite remote sensing is a powerful tool to estimate E at a wide range of spatial scales ranging from an individual pixel to a raster image of an entire river basin. However, the practical use of optical satellite measurements has been limited by cloud cover and the availability of field data to support the remote sensing techniques. Satellite data are only available when cloud free conditions coincide with the time of satellite overpass. In many regions of the world, cloud cover is a predominant feature and the chances of getting cloud free satellite images are limited. The focus of this thesis is the development of methods to monitor E under a variety of cloud conditions in heterogeneous catchments.

The Naivasha basin in Kenya is used as a case study. The elevation of the basin varies from about 1 900 m to 3 200 m above mean sea level. The elevation differences induce a variation in the areal patterns of precipitation. The basin has a diverse landscape ranging from forests in the mountains to dry rangelands in the valley. Rainfed crops, swamps and barren land composed of rock outcrops and non-vegetated lava flows are present. Extensive irrigation is practiced on flowers and vegetables in the vicinity of Lake Naivasha, while pastures are also irrigated for cattle grazing. There are two national wildlife reserves that attract numerous tourists. Lake Naivasha is considered a wetland of international importance, as it was declared a Ramsar site in 1995. There has been an increasingly large demand for water in the basin during the last 30 years due to the high population increase of up to 70%. The fast population increase is attributed to immigration of people from other parts of the country to settle in what was formerly called the white highlands.

In Chapter 2, the theoretical basis of the evaporation process and the parameterization of remote sensing algorithms are presented. The physical laws of water vapour, heat and momentum are incorporated in the Penman-Monteith equation. The Jarvis-Stewart surface resistance models are highlighted to describe the effects of the humidity of the Soil-Vegetation-Atmospheric-Transfer (SVAT) on the evaporation process. The characteristics of different groups of remote sensing

algorithms and their suitability for practical monitoring of surface fluxes are discussed.

Segmentation of landscapes in partial area hydrology has traditionally been done by using land use/cover maps, topographic maps, soil maps and the like. A quick method of delineating a catchment into hydrological units is presented. The surface parameters Normalized Vegetation Index $NDVI$, surface albedo r_0 and surface temperature T_0 derived from Landsat images have been related to fractional vegetation cover, soil water content and surface resistance. Qualitative interpretation of the hydrological and vegetation status of different areas in a catchment can therefore be made from a three-dimensional plot of $NDVI$, r_0 and T_0 (Fig. 4.2). A cluster analysis based on $NDVI$, r_0 and T_0 was performed to divide the study area into 15 hydrological sub-units (Fig 4.3). The surface flux densities were calculated for each unit. This method of subdividing a catchment into hydrological sub-units simplifies the computation of E considerably. Comparison with field data and data from literature showed a satisfactory agreement.

By absence of input data, remote sensing algorithms use various spatially constant input variables in the calculation of E . The impact on E of the handling of spatial variability of input parameters by remote sensing algorithms has been studied. Results of the analysis of the effect of spatial variability of input parameters on E and sensible heat flux density H showed that the near surface air temperatures ΔT_a is the most sensitive parameter. A mean root square fractional difference of 148% in E occurs if ΔT_a is assumed to be spatially constant. The surface roughness length of heat transport z_{0h} appears to be the second most sensitive parameter in the estimation of the areal patterns of the surface fluxes (root mean square fractional difference 44%). The impact of spatial variations of z_{0h} was solved by choosing other integration limits for the eddy diffusivity of heat transport (see Eq 2.44). It was also observed that frictional velocity u_* , stability correction for heat transport ψ_h and surface albedo r_0 considerably affect the calculation of distributed surface fluxes. The implication of these results is that the existing remote sensing algorithms based on energy balance should be re-examined on their characteristics to parameterise the spatial variability of input parameters. Apparently, most published algorithms in the literature appear not to be suitable for the calculation of distributed surface fluxes (Table 4.1). Future work may focus on the development of a simple solution to solve regional scale frictional velocities and related momentum fluxes.

Chapter 5 describes the temporal variability of the evaporative fraction Λ of a grassland and a woodland site in the Naivasha basin. The validity of using instantaneous values of Λ to estimate average day Λ is tested. The diurnal stability of Λ varied significantly during the study period. A correlation analysis between routinely available meteorological variables and the diurnal stability of Λ showed that air temperature T_a , relative humidity RH and cloudiness τ could not adequately explain the diurnal fluctuations of Λ . This demonstrated that the diurnal variation of Λ is a complex phenomenon and other factors influencing Λ , such as demonstrated in Eqs. 5.4 and 5.7, need to be considered.

A good relationship between Λ_{mid} values at midday (12.00 to 13.00 hrs) and the average day Λ was obtained with r^2 of 0.74 at the two experimental sites. Lower r^2 values were obtained in the relationship between morning Λ_{mor} (9.00 to 10.00 hrs) and the average day Λ . The estimated daytime E obtained from Λ_{mid} compared very well with measured daytime E using the Bowen ratio energy balance technique at both experimental sites (RMSE = 0.17 mm, $r^2 = 0.88$ at the Ndabibi site and RMSE = 0.14 mm, $r^2 = 0.93$ at the Eburu site). When the whole study period was considered the average difference between measured daytime E and estimated E from Λ_{mid} was less than 10%. The differences reduce even further if 10-day average E is considered. The main conclusion from Chapter 5 is that *the application of the hypothesis of quasi-constant Λ to estimate daily average E is valid under general weather conditions provided Λ_{mid} is used*. Less satisfactory results were obtained with the use of Λ_{mor} . This showed that the use of data from satellites with morning overpasses between 8.30 to 10.30 hours local time (e.g. Landsat and Terra) will give less accurate daily E values. Designers of satellite systems should be aware of these shortfalls.

The temporal changes in daily average Λ over a year are apparently gradual (Fig. 5.6). This implies that, *in order to capture the seasonal evolution of Λ , it would be sufficient to measure Λ approximately every 10 days*. Multiple regression between 10-day average Λ and 10-day average T_a , RH and τ indicated that these 3 meteorological variables could explain 87% of the variations of the 10-day average Λ . This has important implications for hydrological applications in data-scarce regions. Standard weather data, which are routinely available, could be used to estimate Λ once the empirical relationships between weather data and Λ from available satellite data acquired during cloud free conditions are established.

In Chapter 6, a framework is presented in which continuous daily E under all sky conditions can be obtained from a combination of satellite and standard weather data. Two methods were assessed. In the first method, the Penman-Monteith (PM) equation, in-conjunction with the Jarvis-Stewart (JS) type of model, is used to predict E on cloudy days when satellite data are not available (Fig.6.1). Three analyses were performed assuming that E is known from satellite images on clear days only every other day, every third day or every fifth day. Good comparison was found between predicted E values and measured E for all three analyses when a period of 169 days is considered. Comparison on monthly time scale revealed that the December-January period gave the poorest comparison with r^2 of 0.23 and 0.31 at the Ndabibi and Eburu sites respectively. This was attributed to rapid changes in soil moisture during this period (Fig. 6.6) which induces a dynamic behaviour of the evaporation resistance. The conclusion from the analysis of the presented framework is that for up to 5 continuous days with cloud cover and hence no satellite data available, daily E can be predicted fairly well.

The second method is a simplified alternative based on Λ . The evaporative fraction Λ has been shown to be a good indicator of soil moisture with a gradual seasonal evolution (Fig.5.6). These characteristics of Λ make it amenable for use in the prediction of E during cloudy periods when satellite data are not available. This method also avoids the need to use the complex surface resistance r_s and aerodynamic resistance r_{ah} . When the whole study period of 169 days was considered satisfactory agreement between predicted E and measured E was obtained. The mean predicted daily E and the mean measured daily E were less than 8.8% for all the three analyses of 1, 3 and 5-days with continuous cloud cover. For the November, December and January months, comparison of daily predicted E and measured E showed deviations of more than 100% in the 3-day and 5-day analyses cases especially at the Ndabibi site. *This implies that when daily values of E are required, the Λ method is not suitable for the prediction of E .* However, when daily E values based on Λ were summed over a week, satisfactory comparison was obtained with measured weekly totals of E . The simplicity and suitability of the use of Λ in remote sensing methods are appealing for operational monitoring of E . It is therefore recommended for use in applications that require 7-day totals or longer periods of E .

In Chapter 7 the methods developed in Chapter 6 are applied to actual remote sensing data. Five NOAA AVHRR images were acquired from a public domain site on the internet. Evaporation E was calculated on a daily time scale, for the entire

Naivasha catchment at the NOAA AVHRR pixel scale between 20 January to 3 February 1999. After radiometric calibration and geometric correction of the images, the SEBAL algorithm was used to derive E under clear sky conditions. The evaporation values derived from satellite images agree with the E obtained from the Bowen ratio method at the Ndabibi station and the E values calculated for Lake Naivasha using the energy balance residual method. It was noticed that satellite derived E was mostly higher than field measured E . A possible reason for this may be attributed to the fact the images were taken later than 15.30 hrs. At this time, Λ is usually higher than the average day Λ which may lead to overestimation of E .

Daily E was also predicted for the Naivasha catchment for the two-week period by using the simplified Λ -method. Although predicted and measured E had similar trends in temporal evolution, predicted E was found to be mostly larger than measured E for reasons similar to PM/JS model results. Evaporation predicted by the Λ method and the PM and JS type models was found with an average percentage difference of 12%.

The main conclusion from Chapter 7 is that *it is possible to use the PM and JS type models and Λ to predict the temporal evolution and spatial patterns of E under all weather conditions in a heterogeneous catchment.* The implementation of the PM/JS method requires a land cover classification of the catchment to assign land cover dependent coefficients in the JS model. At each land cover type standard weather data has to be measured. The minimum requirement is a field weather station, which can collect daily average T_a , RH and $K\downarrow$ (or sunshine duration).

Table 8.1 summarizes the methods developed to predict E under cloudy conditions. The table provides an overview of the time scale at which E can be predicted for cloud-free intervals with different lengths. It can be seen that the method of using the PM equation and the JS type model is the best for predicting daily E values. The accumulated E for periods of 7 days and longer can be predicted fairly well by the Λ method. It should also be noted that 10-day average E could be predicted from empirical relationships between Λ and standard weather data.

Table 8.1: The time scales at which evaporation E can be predicted for cloudy periods by applying the constant evaporation fraction A method and the Penman-Monteith equation complemented with the Jarvis-Stewart model

	A_{mid}	PM/JS
Cloud free period	E prediction	E prediction
2 days	1 day total	1 day total
6 days	7 day total	1 day total
>10 days	10 day total	n.a.

Samenvatting en conclusies

Verdamping is noodzakelijk voor verschillende toepassingen in de hydrologie, landbouw en meteorologie. De verdamping E van heterogene stroomgebieden vertoont een grote ruimtelijke en temporele variatie. Satelliet remote sensing is een goed hulpmiddel om E te schatten voor ruimtelijk schalen variërend tussen een individueel beeldelement en een rasterbeeld van een compleet rivier systeem. Het praktisch gebruik van optische satellietmetingen is echter beperkt door wolkenbedekking en de beschikbaarheid van veldgegevens om de remote sensing rekentechnieken te ondersteunen. Satellietgegevens zijn alleen bruikbaar als de satelliet bij onbewolkte condities overkomt. Wolkenbedekking is een dominant verschijnsel in verscheidene delen van de wereld, en de mogelijkheden voor het verkrijgen van wolkeloze satellietbeelden is daarom beperkt. Het accent van dit proefschrift ligt op het ontwikkelen van methodes om het monitoren van E onder variabele bewolgingscondities in heterogene stroomgebieden mogelijk te maken.

Het riviersysteem van Naivasha in Kenia is gekozen als studiegebied. De hoogteligging van het terrein varieert van 1900 m tot 3200 m boven gemiddeld zeeniveau. De verschillen in terreinhoogte veroorzaken ruimtelijke patronen in neerslag. Het stroomgebied herbergt een divers landschap variërend van bossen in de bergen tot droge graslandgebieden in de valleien. Er wordt regenafhankelijke landbouw bedreven en er komen moerassen, kale grond, rotsen en niet-begroeide lavastromen voor. In de nabijheid van het Naivasha meer worden bloemen en groente op grote schaal geïrrigeerd. Tevens worden er weidegebieden voor begrazing geïrrigeerd. Er zijn een tweetal nationale wildparken aanwezig wat veel toeristen aantrekt. Het Naivasha meer wordt als een internationaal belangrijke wetland beschouwt en het is in 1995 tot een Ramsar gebied uitgeroepen. Tengevolge van bevolkingsgroei, is de waterbehoefte van het stroomgebied gedurende de afgelopen 30 jaar met 70% toegenomen. De snelle bevolkingstoename kan aan de immigratie van bewoners uit andere gedeeltes van het land worden toegeschreven, die zich vestigen in wat voorheen de 'white highlands' werd genoemd.

De theoretische achtergrond over verdampingsprocessen en de remote sensing parameterizatie daarvan staat beschreven in hoofdstuk 2. De wetmatigheden van waterdamp, warmte en impuls zijn geïntegreerd in de Penman-Monteith vergelijking. Het Jarvis-Stewart model voor de verdampingsweerstand wordt gebruikt om de vochtigheid van het bodem-atmosfeer systeem op het verdampingsproces weer te geven. De eigenschappen van verschillende remote sensing rekenmodellen en hun geschiktheid voor het praktisch monitoren van oppervlakte-fluxdichtheden wordt besproken.

Het segmenteren van landschappen in sub-stroomgebieden wordt traditioneel gedaan op basis van landgebruik, topografische kaarten, bodemkaarten etc. Een

snelle methode om een stroomgebied in hydrologische eenheden te verdelen is gepresenteerd. De oppervlakte parameters Normalized Difference Vegetation Index $NDVI$, oppervlakte albedo r_0 en oppervlakte temperatuur T_0 afgeleid uit Landsat beelden zijn gerelateerd aan vegetatiebedekking, bodemvochtgehalte en de verdampingsweerstand. Het kwalitatief interpreteren van de hydrologische condities en de status van de vegetatie voor sub-eenheden binnen een stroomgebied kan worden verkregen door het vervaardigen van een 3D-plot van $NDVI$, r_0 en T_0 (zie Fig. 4.2). Een cluster analyse gebaseerd op $NDVI$, r_0 en T_0 is uitgevoerd om het studiegebied in 15 hydrologische sub-eenheden op te delen (Fig. 4.3). De oppervlakte fluxdichtheden zijn uitgerekend voor elke klasse. Deze methode voor het opdelen van een stroomgebied in hydrologische sub-eenheden, vereenvoudigt het uitrekenen van de ruimtelijke variatie van E aanzienlijk. Een vergelijking van de resultaten met veldgegevens en gegevens verschenen in de literatuur, geeft een goede overeenkomst weer.

Bij afwezigheid van invoergegevens gebruiken remote sensing rekenmodellen verschillende ruimtelijk constante invoervariabelen. Het effect van het beschouwen van de ruimtelijke variabiliteit van de invoervariabelen is bestudeerd. Het resultaat geeft aan dat het verticaal verschil in luchttemperatuur nabij het landoppervlak ΔT_a de meest essentiële parameter is om de ruimtelijke variatie in fluxdichtheden goed te beschrijven. Een fractioneel *root mean square* verschil van 148% op de verdamping komt voor als ΔT_a ruimtelijk constant wordt verondersteld. De ruwheidslengte voor warmte transport z_{0h} bleek de tweede meest gevoelige parameter voor het schatten van de ruimtelijke patronen van de oppervlakte-fluxdichtheden te zijn (het fractionele *root mean square* verschil is 44%). De invloed van de ruimtelijke variatie van z_{0h} is opgelost door een andere integratie grens voor de eddie diffusiviteit voor warmtetransport te kiezen (zie vergl. 2.44). Het blijkt ook dat de wrijvingsnelheid u_* , de stabiliteit correctie voor warmte transport ψ_h en de oppervlakte albedo r_0 een aanzienlijk effect op de berekening van de ruimtelijke verdeling van de oppervlakte fluxdichtheden kan hebben. Het gevolg van deze resultaten is dat bestaande remote sensing rekenmodellen gebaseerd op de energiebalans moeten worden bekeken op hun kenmerken voor het beschrijven van de ruimtelijke variabiliteit van de invoervariabelen. Het is gebleken dat de meeste in de literatuur gepubliceerde remote sensing rekenmodellen niet aan deze voorwaarde voldoen (Tabel 4.1). Toekomstig remote sensing onderzoek zou zich kunnen richten op de ontwikkeling van een eenvoudige manier om wrijvingsnelheden en de daaraan gekoppelde impulsflux op regionale schaal te schatten.

Hoofdstuk 5 beschrijft de temporele variabiliteit van de verdampingsfractie Λ van een grasland- en een bosgebied in Naivasha. De geldigheid van het gebruik van de moment opname van Λ als maat voor de dagwaarde van Λ is getest. Het dagelijks verloop van Λ varieerde aanzienlijk gedurende de studieperiode. Een correlatieanalyse tussen routinematig beschikbare meteorologische variabelen en het dagelijks verloop van Λ laat zien dat luchttemperatuur, relatieve luchtvochtigheid en bewolking niet het dagelijkse verloop van Λ kunnen verklaren.

Dit toont aan dat de dagelijkse variatie van Λ een complex verschijnsel is en dat andere factoren zoals weergegeven in vergl. 5.4 en 5.7 moeten worden meegenomen.

Er is een goed verband gelegd tussen Λ_{mid} waarden (opgenomen tijdens 12.00 tot 13.00 uur) en de dagelijks waarde van Λ voor de twee proefgebieden ($r^2=0.74$). Lagere r^2 waarden zijn vastgesteld voor de relatie tussen de ochtend waarde van Λ_{mor} (9.00 tot 10.00 uur) en de gemiddelde dagwaarde van Λ . De gemiddelde dagverdamping E geschat uit Λ_{mid} vertoont voor beide proefgebieden een goede overeenkomst met de gemeten dagverdamping E volgens de Bowen verhouding energie balans methode (RMSE=0.17 mm d⁻¹, $r^2=0.88$ op het grasland van Ndabibi en RMSE=0.14 mm d⁻¹, $r^2=0.93$ in het bos van Eburu). Over de gehele studieperiode is het gemiddelde verschil tussen gemeten en geschatte dagwaarde van E minder dan 10%. De verschillen voor 10-daagse gesommeerde waarden van E zijn zelfs kleiner. De belangrijkste conclusie van hoofdstuk 5 is dat de toepassing van het uitgangspunt van een quasi-constante verdampingsfractie voor de schatting van de dagelijkse verdamping correct is, mits er van Λ_{mid} gebruik gemaakt wordt. De resultaten door het gebruik van Λ_{mor} zijn minder gunstig. Dit betekent dat het gebruik van satellietmetingen in banen met een overkomsttijd tussen 8.30 en 10.30 uur locale tijd (b.v. Landsat en Terra) minder nauwkeurige dagwaardes van verdamping opleveren, als opnames gemaakt tijdens het middaguur. De ontwerpers van satellietssystemen dienen van deze bevinding op de hoogte te zijn.

Het temporele gedrag van de dagelijkse gemiddelde Λ gedurende het jaar verloopt geleidelijk (Fig. 5.6). Dit impliceert dat voor de beschrijving van Λ gedurende het seizoen kan worden volstaan met het meten van Λ eenmaal per 10 dagen of langere periodes. Een meervoudige regressie tussen 10-daagse gemiddelde waarden van Λ en 10-daagse gemiddelden van luchttemperatuur, relatieve luchtvochtigheid en transmissiviteit toont aan dat deze 3 meteorologische variabelen 87% van de variatie in de 10-daagse gemiddelde Λ waarde kunnen verklaren. Dit heeft belangrijke gevolgen voor hydrologische toepassingen voor gebieden met weinig meetgegevens. Routinematig beschikbare weersgegevens kunnen worden gebruikt om Λ te schatten als het empirisch verband tussen weersgegevens en Λ is vastgesteld voor een aantal satelliet opnames onder onbewolkte condities in het groeiseizoen.

Hoofdstuk 6 bevat een beschrijving hoe een continue serie van dagelijkse E kan worden verkregen onder omstandigheden met wisselende bewolking uit een combinatie van satelliet- en meteorologische data. Twee verschillende methodes zijn getest. De eerste methode is de Penman-Monteith (PM) vergelijking in combinatie met het Jarvis-Stewart (JS) model om E op bewolkte dagen te schatten als er geen satellietbeelden voorhanden zijn (Figuur 6.1). Drie analyses zijn gemaakt onder de aanname dat E uit satelliet beelden bekend is voor elke andere onbewolkte dag, elke derde dag en elke vijfde dag. Voor een totale periode van 169 dagen is er een goede overeenkomst geconstateerd tussen geschatte en gemeten

dagwaardes van E voor alle drie analyses. Een vergelijking voor de proefgebieden Ndabibi en Eburu op een maandelijkse tijdschaal geeft aan dat de periode december t/m januari met $r^2=0.23$ en 0.31 de laagste correlatie oplevert. Dit kan worden toegeschreven aan de snelle veranderingen in het bodemvocht gedurende deze periode (figuur 6.6) waardoor de verdampingsweerstand zich sterk dynamisch gedraagt. De conclusie is dat de dagelijkse verdamping voor een periode van 5 doorlopende dagen met bewolking zonder satellietgegevens met het PM/JS model in het algemeen redelijk goed kan worden voorspeld.

De tweede methode is een versimpeling en gebaseerd op de verdampingsfractie Λ . De verdampingsfractie blijkt een goede indicator van geleidelijke seizoensveranderingen van bodemvocht te zijn (Fig. 5.6). Deze eigenschap maakt Λ ook toepasbaar voor de voorspelling van korte termijn E variaties gedurende bewolkte periodes als satellietgegevens niet beschikbaar zijn. Deze methode vermijdt het gebruik van de soms lastige verdamping- en aërodynamische weerstanden in de PM vergelijking. De overeenkomst tussen voorspelde en gemeten E was goed voor de gehele studieperiode van 169 dagen. Het verschil tussen de gemiddelde geschatte waarde van E en de gemiddelde gemeten E was minder dan 8.8 % voor alle drie analyses met 1, 3 en 5 dagen continue wolkenbedekking. De vergelijking tussen dagelijks voorspelde E en gemeten E vertoont afwijkingen van meer dan 100% voor de 3 en 5 dagen analyses. Dit geldt vooral voor de Ndabibi meetplaats. Dit betekent dat de Λ -methode niet geschikt is om dagelijkse waardes van E te voorspellen. Een goede overeenkomst wordt echter bereikt als de dagelijkse E waardes worden gesommeerd voor een periode van een week. De eenvoud en geschiktheid van het gebruik van Λ in remote sensing methodes is aantrekkelijk voor het operationeel monitoren van E . De verdampingsfractie is daarom aanbevolen voor toepassingen van E gesommeerd over 7 dagen en langer.

Hoofdstuk 7 past de theoretische methodes die in hoofdstuk 6 ontwikkeld zijn toe met actuele remote sensing data. Vijf NOAA AVHRR beelden zijn ontleend aan een publieke databestand op internet. De verdamping E is voor het gehele Naivasha stroomgebied uitgerekend op dagbasis tussen 20 januari en 3 februari 1999. Het SEBAL rekenmodel voor E is toegepast op onbewolkte dagen na radiometrische- en geometrische correcties van de beelden. De verdampingcijfers verkregen uit satellietbeelden vertonen een goede overeenkomst met E verkregen uit de Bowen verhouding methode (Ndabibi) en met de energie balans residu methode (Naivasha meer), maar is wel hoger dan de veldmetingen van E . Een mogelijke reden is het late opnametijdstip na 15.30 uur. De verdampingsfractie Λ is normaliter op dit tijdstip hoger dan het gemiddelde van de dag, hetgeen tot een overschatting van E leidt.

De dagelijkse E is ook voorspeld voor het gehele Naivasha stroomgebied voor de 2-wekelijkse periode door gebruik te maken van de simpele Λ methode. Ofschoon de voorspelde en gemeten E dezelfde temporele trend vertonen, is de geschatte E hoger

dan de gemeten E om dezelfde redenen als weergegeven voor het PM/JS model. De Λ methode en de PM/JS modellen vertonen een onderlinge afwijking van 12 %.

De belangrijkste conclusie van hoofdstuk 7 is dat het PM/JS model en de Λ -methode beiden het temporele en ruimtelijke gedrag van E onder alle weersomstandigheden in een heterogeen stroomgebied kunnen beschrijven. De implementatie van de PM/JS methode vereist een landgebruikclassificatie van het stroomgebied omdat de JS coëfficiënten landgebruikafhankelijk zijn. Elk vorm van landgebruik dient uitgerust te zijn met standaard meteorologische waarnemingen. De minimum vereiste parameters zijn de dagelijks gemiddelde waarden van luchttemperatuur, relatieve luchtvochtigheid en globale straling (of zonneshijnduur).

Tabel 8.1 bevat een samenvatting van de ontwikkelde methodes om E te schatten onder bewolkte condities. De tabel geeft een overzicht van de tijdschaal waarop E kan worden geschat voor periodes met wisselende bewolking. De methode voor het gebruik van de PM vergelijking en het JS model is het meest geschikt voor dagelijkse waarden van E met een wolkeloze periode van 6 dagen. The gesommeerde E voor periodes van 7 dagen en langer kan redelijk worden voorspeld met de Λ methode. Het dient te worden opgemerkt dat de gemiddelde E over 10 dagen kan worden geschat uit een empirische relatie tussen Λ en routinematig verkregen weersgegevens.

Tabel 8.1: De tijdschalen waarop E kan worden geschat voor bewolkte condities door het gebruik maken van de constante verdampingsfractie Λ -methode en de Penman-Monteith vergelijking aangevuld met het Jarvis/Stewart model.

Bewolkte periode	Λ_{mid}	PM/JS
	E voorspelling	E voorspelling
2 dagen	1 dag	1 dag
6 dagen	7 gesommeerde dagen	1 dag
>10 dagen	10 gesommeerde dagen	n.a.

References

- Abdellaoui, A., F. Becker and E. Olory-Hechninger, 1986. Use of Meteosat for mapping thermal inertia and evapotranspiration over a limited region of Mali. *J. Applied Meteor.*, 25:1489-1506
- Allen, R.G., L.S. Preira, D. Raes and M. Smith., 1998. Crop evapotranspiration: Guidelines for computing crop water requirements. FAO irrigation and Drainage Paper 56
- Ase, L.E., K. Sernbo and P. Syren. 1986. Studies of Lake Navaisha, Kenya, and its drainage area, Stockholm University, Inst. of Nat. Geography, Sweden, ISSN 0346-7406, STOU-NG 63: 79 pp.
- Ashfaque, A. 1999. Estimating lake evaporation using meteorological data and remote sensing, M.Sc. Thesis, International Institute of Aerospace Survey and Earth Sciences - ITC, Enschede, The Netherlands: 93 pp.
- Baret, F. and G. Guyot. 1991. Potentials and limits of vegetation indices for LAI and APAR assessment, *Rem. Sens. of Env.*, 35: 161-173
- Bastiaanssen, W.G.M. 1995. Regionalization of surface flux densities and moisture indicators in composite terrain: A remote sensing approach under clear skies in Mediterranean climates. PhD thesis, University of Wageningen, The Netherlands. 273pp
- Bastiaanssen, W.G.M. 2000. SEBAL-based sensible and latent heat fluxes in the irrigated Gediz Basin, Turkey. *J. of Hydrol.* 229:87-100
- Bastiaanssen, W.G.M. and R.A. Roebeling. 1993. Analysis of land surface exchange processes in two agricultural regions in Spain using Thematic Mapper Simulator data, in (eds.) Bolle, Feddes and Kalma, Exchange processes at the land surface for a range of space and time scales, *IAHS Publ.*, 212: 407-416
- Bastiaanssen, W.G.M., M. Menenti, A.J. Dolman, R.A. Feddes and H. Pelgrum. 1996. Remote sensing parameterization of meso-scale land surface evaporation, in *Radiation and water in climate system: Remote measurements.* (ed.) E. Rascheke, NATO ASI series 1 vol.45: 401-429. Berlin. Springer-Verlag.
- Bastiaanssen, W.G.M., H. Pelgrum, J. Wang, Y. Ma, J.F. Moreno, G.J. Roerink and T. van der Wal. 1998a. A remote sensing surface energy balance algorithm for land (SEBAL), part 2 Validation, *J. of Hydr.*, 212-213, 213-229
- Bastiaanssen, W.G.M., M. Menenti, R.A. Feddes and A.A.M. Holtslag. 1998b. A remote sensing surface energy balance algorithm for land (SEBAL), part 1: Formulation, *J. of Hydr.*, 212-213, 198-212

Beljaars A.C.M. and A.A.M. Holtslag, 1991. Flux parameterization over land surfaces for atmospheric models. *J. Appl. Meteor.* 30:327-341

Blyth, E.M. 1994. The effect of small scale heterogeneity on surface heat and moisture fluxes, Ph.D. Thesis University of Reading, Department of Meteorology UK: 152 pp.

Bougllet, B., P. Bret, P. Lacarrera and J. Noilhan. 1991. An example of spatial integration of a land-surface parameterization in a meso-beta-scale model in Eds. T.J. Schmugge and J.C. Andre, Land surface evaporation, Springer Verlag: 383-414

Bowen, I.S. 1926. The ratio of heat losses by conduction and by evaporation from any water surface. *Phys. Rev.* 27:779-798

Bruin, de, H.A.R. and J. Q. Keijman. 1979. The Priestley-Taylor evaporation model applied to a large, shallow lake in the Netherlands, *J. Applied Meteor.*, 18: 893-903

Bruin, H.A.R de, and A.A. Holtslag., 1982. A simple parameterization of the surface fluxes of sensible and latent heat during daytime compared to Penman-Monteith concept. *J. of Applied Met.* Vol 21:1610-1621

Brutsaert, W. 1975. On a derivable formula for long-wave radiation from clear skies *Water Resour. Res.*, 11:742-744

Brutsaert, W. 1982. Evaporation into the atmosphere, theory, history and applications, Reidel, Dordrecht: 299 pp.

Brutsaert, W. and M. Sugita., 1992. Application of self preservation in the diurnal evolution of the surface energy budget to determine daily evaporation. *J. Geophys. Res.*, 97(D17):18377-18382

Brutsaert, W., A.Y. Hsu and T.J. Schmugge. 1993. Parametrization of surface heat fluxes above forest with satellite thermal and boundary layer soundings. *J. Applied Meteor.*, 32: 909-917

Bussieres, N. and K. Goita. 1997. Evaluation of strategies to deal with cloudy situations in satellite evapotranspiration algorithms. *Proc. 3rd Int. workshop. NHRI symp. 17.* NASA, Goddard space flight centre, Maryland U.S.A. 33-43

Carlson, T.N. and M.J. Buffum. 1989. On estimating total daily evapotranspiration from remote surface temperature measurements, *Rem.Sens. Env.*, 29:197-207

Carlson, T.N., O. Taconet, A. Vidal, R.R. Gillies, A. Olioso and K. Humes. 1995. An overview of the workshop on thermal remote sensing held at La Londe les Maures, France, September 20-24, 1993, *Agr. and Forest Met.*, 77:141-151

Chehbouni, A., D. Lo Seen, E.G. Njoku, J.P. Lhomme, B. Monteny and Y.H. Kerr. 1997. Estimation of sensible heat flux over sparsely vegetated surfaces. *J. of Hydrol.* 188-189: 855-868

Chen, D., E.T. Engman and W. Brutsaert. 1997. Spatial distribution and pattern persistence of surface soil moisture and temperature over prairie from remote sensing, *Rem. Sens. of Env.*, 6: 347-360

Choudhury, B.J. and J.L. Monteith. 1988. A four-layer model for the heat budget for homogeneous land surfaces, *Q.J.R.Met. Soc.* 114:373-398

Choudhury, B.J. 1989. Estimating evaporation and carbon assimilation using infrared temperature data: Vistas in modeling, ed. G. Asrar. *Theory and applications in optical remote sensing*, John Wiley, New York: 628-690

Choudhury, B.J. and S.B. Idso. 1985. An empirical model for stomatal resistance of field-grown wheat. *Agric. And Forest Met.* 36:55-82

Choudhury, B.J., 1991. Multispectral satellite data in the context of land surface heat balance. *Rev. of Geophy.*, 29:217-236

Choudhury, B.J., N.U. Ahmed, S.B. Idso, R.J. Reginato and C.S.T. Daughtry. 1994. Relations between evaporation coefficients and vegetation indices studied by model simulations, *Rem. Sen. Env.*, 50: 1-17

Choudhury, B.J., R.J. Reginato and S.B. Idso. 1986. An analysis of infrared temperature observations over wheat and calculation of latent heat flux. *Agric. and Forest Met.* 37:75-88

Choudhury, B.J. 1997a. Estimating land surface evaporation using multispectral satellite and ancillary data. In Eds. Kite, G.W, Pietroniro, A, Pultz, T. *Applications of Remote sensing in Hydrology. Proc. Symp. No. 17 NHRI, Saskatoon, Canada*

Choudhury, B.J. 1997b. Global patterns of potential evaporation calculated from the Penman-Monteith equation using satellite and assimilated data. *Remote. Sens. Environ.* 61:64-81

Clark, B.P. 1986. New look-up tables. EOSAT, Landsat Technical Notes No. 1. 8 pp.

Cosgrove, W.J. and F.R. Rijsberman, 2000. *World Water Vision, making water everybody's business*, world Water Council, Earthscan Publ. Ltd., London UK: 180pp

Courault, D., Lagouarde J.P. and Aloui, B., 1996. Evaporation for maritime catchment containing a meteorological model with vegetation information and airborne surface temperature. *Agric and Forest Met.* 82:93-117

Crago, R.D. and W. Brutsaert., 1996. Daytime evaporation and the self-preservation of the evaporative fraction and the Bowen ratio. *J.Hydrol.*, 178:241-255

Crago, R.D., 1996a. Comparison of the evaporative fraction and Priestly-Taylor α for parameterizing daytime evaporation. *Water Resour. Res.*, Vol 32(5) : 1403-1409

Crago, R.D., 1996b. Conservation and variability of the evaporative fraction during the daytime. *J.Hydrol.* 180:173-194

Daughtry, C.S.T., W.P. Kustas, M.S. Moran, P.J. Pinter, R.D. Jackson, P.W. Brown, W.D. Nichols and L.W. Gay. 1990. Spectral estimates of net radiation and soil heat flux, *Rem. Sens. Env.*, 39:141-152

De Rooy, W.C. and A.A.M. Holtslag. 1999. Estimation of surface radiation and energy flux densities from single-level weather data. *J. Appl. Meteor.* 38:526-540

Decurtins, S. 1992. Hydrogeographical investigations into the Mount Kenya subcatchment of the Ewaso Ngiro river. University of Bern Switzerland. African Studies Series No. A10

Diak, G. and M.S. Whipple. 1993. Improvements to models and methods for evaluating the land-surface energy balance and effective roughness using radiosonde reports and satellite measured skin temperature data, *Agr. and Forest Meteor.* 65:21-45

Dolman, A.J., J.H.C. Gash, J. Roberts and W.J. Shuttleworth. 1991. Stomatal and surface conductance of tropical rainforest. *Agric and Forest Met.*, 54:303-318

Dolman, A.J. 1993. A multiple-source land surface energy balance model for use in general circulation models. *Agric. and Forest Met.*, 65:21-35

Dolman, A.J., Stewart, J.B. and Cooper, J.D., 1988. Predicting forest transpiration from climatological data. *Agric and Forest Met.* 42:339-353

Donia, N.S. 1998. Integration of GIS and computer modelling to study the water quality of Lake Navaisha, Central Rift Valley, Kenya, M.Sc. Thesis, International Institute of Aerospace Survey and Earth Sciences - ITC, Enschede, The Netherlands: 116 pp.

Dyer, A. J. and B.B. Hicks. 1970. Flux-gradient relationships in the constant flux layer. *Q.R.R. Met. Soc.* 96:715-721

Farah, H.O. and W.G.M. Bastiaanssen. 2000. The impact of spatial variations of land surface parameters on regional evaporation: A case study with remote sensing data. *Hydrol. Processes* (in press)

Farah, H.O., W.G.M. Bastiaanssen and R.A. Feddes. 2000. Evaluation of the temporal variability of the evaporative fraction in a tropical watershed. *Hydrol. Earth System Sciences*. (Submitted)

Franks, S.W. and K.J. Beven. 1997. Estimation of evapotranspiration at the landscape scale: a fuzzy disaggregation approach, *Water Resources Research*, 33:2929-2938

Gash, J.H.C., J.S. Wallace, C.R Lloyd and A.J.Dolman. 1991. Measurement of evaporation from shallow sahelian savannah at the start of the dry season. *Q.J.R. Meteorol. Soc.* 117:749-760

Granger, R.J. 1997. Comparison of surface and satellite-derived estimates of evapotranspiration using a feedback algorithm. In *Application of remote sensing in hydrology: Proc. Of 3rd Int. workshop*. Oct. 1996, NASA, Goodard Space Flight ceter, Greenbelt, Maryland USA.

Griend, van der, A.A. and M. Owe. 1993. On the relationship between thermal emissivity and the normalized difference vegetation index for natural surfaces, *Int. J. Of Rem. Sens.*, 14(6):1,119-1,131

Hall, F.G., K.F. Huemmrich, S.J. Goetz, P.J. Sellers and J.E. Nickeson., 1992. Satellite remote sensing of the surface energy balance: success, failures and unresolved issues in FIFE. *J. Geophys. Res.*, 97(D17):19061-19089

Hamududu, B.H., 1998. Erosion assessment of large basins using remote sensing and GIS: a case study of lake Naivasha basin Kenya. M.Sc. Thesis, International Institute of Aerospace Survey and Earth Sciences - ITC, Enschede, The Netherlands: 123pp

Hanan, N.P. and S.D. Prince. 1997. Stomatal conductance of west-central supersite vegetation in Hapex-sahel: measurement and empirical models. *J. of Hydrol.* 188-189:536-562

Hatfield, J.L., R.J. Reginato and S.B. Idso. 1984. Evaluation of canopy temperature-evapotranspiration models over various surfaces. *Agric. and Forest Met.*, 46:15-22

Heckbert, P., 1982. Colour image quantization buffer display. *SISGRAPH82 proceedings*. 297-315

Holtstag, A.A.M and A.P. Van Ulden., 1983. A simple scheme for daytime estimates of the surface fluxes from routine weather data. *J. of Applied Met.*, 27:684-704

Hurdato, E., M.M. Artugao, and V. Caselles. 1994. Estimating maize (*Zea mays*) evapotranspiration from NOAA-AVHRR thermal data in Albacete area, Spain. *Int. J. of Rem. Sens.* 15(10):2023-2037

Inoue, E. 1963. On the turbulent structure of airflow within crop canopies. *J. Meteorol. Soc. Japan*. 41:317-326

Iqbal, M., 1983. An introduction to solar radiation. Academic Press, Toronto

Jackson, R.D. 1984. Total reflected solar radiation calculated from multi-band sensor data, *Agric. and Forest Met.*, 33:163-175

Jackson, R.D., J.L. Hatfield, R.J. Reginato, S.B. Idso, and P.J. Pinter Jr., 1983. Estimation of daily evapotranspiration from one time day measurements. *Agric. Water Management*, 7:351-362

Jackson, R.D., R.J. Reginato and S.B. Idso. 1977. Wheat canopy temperature: a practical tool for evaluating water requirements, *Water Resources Research* 13:651-665

Jarvis, P.G., 1976. The interpretation of the variations in leaf water potential and stomatal conductance found in canopies in the field. *Phil. Trans. R. Soc. London* . B273:593-610

Jensen, 1990 *Evapotranspiration and irrigation water requirements*, ASCE Manuals and Reports on Engineering Practice No.70. New York: ASCE

Kabat P., A.J. Dolman and J.A. Elbers. 1997. Evaporation, sensible heat flux and canopy conductance of fallow savannah and patterned woodland in the Sahel. *J. of Hydrol.* 188-189:494-515

Kalma, J.D. and D.L.B. Jupp. 1990. Estimating evaporation from pasture using infrared thermography: evaluation of a one-layer resistance model, *Agr. and Forest Met.*, 51:223-246

Kidwell, G.G., 1998. NOAA Polar Orbiter Data Users' Guide, National Oceanic and Atmospheric Administration, World Weather building, Room 100, D.C.

Koepke, P., K.T. Kriebel and B. Dietrich. 1985. The effect of surface reflection and of atmospheric parameters on the shortwave radiation budget, *Adv. Space Res.*, 5:351-354

Kohler, Th., 1987. Land use in transition. Aspects and problems of small scale farming in a new environment: *Geographica Bernensia* Vol 5, Berne

Kustas, W.P. 1990. Estimates of evapotranspiration with one and two-layer model of heat transfer over partial canopy cover, *J. Appl. Met.* 29:704-815

Kustas, W.P., and J.M. Norman., 1996. Use of remote sensing for evapotranspiration monitoring over land surfaces. *Hydrol. Science J.* 41(4):495-515

Kustas, W.P., M.S. Moran, K.S. Humes, D.I. Stannard, P.J.Pinter, L.E.Hipps, E.Swiatek and D.C. Goodrich. 1994. Surface energy balance at local and regional scales using optical remote sensing from aircraft platform and atmospheric data collected over semiarid rangelands, *Water Resources Research*, 30:1241-1259

Lhomme, J.P., E. Elguero, A. Chehbouni and G. Boulet. 1998. Stomatal transpiration: Examination of Monteith's formulation of canopy resistance. *Water Resources Research*, 34(9):2301-2308

Lhomme, J.P., B. Monteny and M. Amadou. 1994. Estimating sensible heat flux from radiometric temperature over sparse millet, *Agr. and Forest Met.*, 68:77-91

Markham, B.L. and J.L. Barker. 1987. Thematic Mapper bandpass solar exoatmospherical irradiances, *Int. J. of Rem. Sens.*, 8(3):517-523

Mason, P. 1988. The formulation of areally averaged roughness lengths, *Q.J.R. Meteorol. Soc.*, 114:399-420

McNaughton, K.G. 1994. Effective stomatal and boundary layer resistances of heterogeneous surfaces, *Plant, Cell and Env.*, 17, 1061-1068

Menenti, M. 1993. Understanding land surface evapotranspiration with satellite multispectral measurements. *Adv. In Space Reserch COSPAR*. 13(5):89-100

Menenti, M. and Choudhury, B.J. 1994. Synergetic use of thermal infrared and other spectral measurements for land surface studies, *Proc. Workshop on thermal remote sensing, La Londe, september 1993*, 167-176

Menenti, M., 1984. Physical aspect and determination of evaporation from deserts, ICW Report 4, DLO-Winand Staring Centre, Ph.D. Thesis, Wageningen Agricultural University, The Netherlands

Menenti, M., W.G.M. Bastiaanssen and D. Van Eick. 1989a. Determination of hemispherical reflectance with Thematic Mapper data. *Rem. Sens. Environ.* 28: 327-337

Menenti, M., W.G.M. Bastiaanssen, D. Van Eick and M.H. Abd el Karim. 1989b. Linear relationships between surface reflectance and temperature and their application to map actual evaporation of groundwater, *Adv. Space Res.*, 9(1):165-176

Monin, A.S. and A.M. Yaglom. 1971. *Statistical fluid mechanics: mechanics of turbulence*, 2 vol 1.

Monteith, J.L. 1965. Evaporation and the environment. In: *The state and movement of water in living organisms*, XIXth Symposium, Soc for exp. Biol, Swansea, Cambridge Univ. Press:205-234

Moran, M.S., S.J. Maas and P.J. Pinter. 1995. Combining remote sensing and modeling for estimating surface evaporation and biomass production, *Rem. Sens. Rev.*, 12:335-353

Moran, S.M. and R.D. Jackson. 1991. Assessing the spatial distribution of evaporation using remotely sensed inputs. *J. Environ. Qual.* 20:725-737

Nemani, R.R. and S.W. Running. 1989. Estimation of regional surface resistance to evapotranspiration from NDVI and thermal-IR AVHRR data, *J. of Applied Met.*, 28:276-284

Nichols, W.E. and R.H. Cuenca., 1993. Evaluation of the evaporative fraction for the parameterization of the surface energy balance. *Water Resour. Res.*, 29(11):3681-3690

Nieuwenhuis, G.J.A., E.M. Smidt and H.A.M. Thunnissen. 1985. Estimation of regional of evapotranspiration of arable crops from thermal infrared images. *Int. J. of Rem.Sens.*, 6(8): 1319-1334

Noilhan, J., P. Lacarrere, A.J. Dolman and E.M. Blyth. 1997. Defining area-average parameters in meteorological models for land surfaces with meso-scale heterogeneity, *J. of Hydr.*, 190:302-316

Paralange, M.B., 1995. Regional scale evaporation and the atmospheric boundary layer. *Rev. of Geophy.* 33:99-124

Paulson, C.A. 1970. The mathematical representation of wind speed and temperature profiles in unstable atmospheric surface layer. *J. Appl. Meteor.* 9:856-861

Pelgrum, H. and W.G.M. Bastiaanssen. 1996. An intercomparison of techniques to determine the area-averaged latent heat flux from individual in situ observations: A remote sensing approach using the European Field Experiment in a desertification-Threatened Area data. *Water Resour. Res.*, 32(9): 2775-2786

Pelgrum, H. and W.G.M. Bastiaanssen. 1997. The non-linearity between surface fluxes and remotely observable land surface characteristics and its consequences for pixel size selection, 13th Conference on Hydrology, 2-7 February 1997, Longbeach, California, American Meteorological Society, P8.3:342-344

Penman, H.L. 1948. Natural evaporation from open water, bare soil and grass. *Proc. R. SOC. Land ser.a*, 193:120-145

Petehercych, S., B. Goodison, V. Swail and A. Saulesleja, 1983. Clouds: A fundamental limitation to satellite remote sensing in the visible spectral region. *Proceedings of Eighth Canadian Symposium on Remote Sensing*. Sherbrooke, Quebec, Canada, 1983: 223-228

Pinty , B. and Ramond, D. 1987. A method for the estimate of broadband directional surface albedo from a geostationary satellite, *Jou. of Clim. and App. Meteo.*, 26:1,709-1,722

Prihodko, L. and S.N. Goward. 1997. Estimation of air temperature from remotely sensed surface observations, *Rem. Sens. Env.*, 60:335-346

Qualls, R.J., W. Brutsaert and W.P. Kustas, 1993. Near-surface air temperature as substitute for skin temperature in regional surface flux estimation. *J. of Hydrol.* 143: 381-393

Rosema, A. 1990. Comparison of meteosat-based rainfall and evapotranspiration mapping sahel region *Int.J. of Rem.Sens.*, 11(12):2299-2309

Rosema, A., 1993. Using METEOSAT for operational evapotranspiration and biomass monitoring in the sahel region. *Rem. Sens Env.* 46:27-44

Rowntree, P.R., 1991. Atmospheric parametrization schemes for evaporation over land: basic concepts and climate modeling aspects. In: *Land surface evaporation.* Eds. Schumugge, T.J and J.C. Andre. Springer, New York:5-29

Sandholt, I. and H.S. Anderson. 1993. Derivation of actual evapotranspiration in the Senegalese Sahel, using NOAA-AVHRR data during the 1987 growing season. *Rem. Sens Env.* 46:164-172

Saunders, R.W. and K.T. Kriebel. 1988. An improved method for detecting clear sky and cloudy radiances from AVHRR data. *Int. J. Rem.Sens.* 9(1):123-150

Schmugge, T., S.J. Hook and C. Coll. 1998. Recovering surface temperature and emissivity from thermal infrared multispectral data, *Rem. Sens. Env.*, 65:121-131

Seguin, B. and B. Itier. 1983. Using midday surface temperature to estimate daily evaporation from satellite thermal IR data, *Int. J. of Rem. Sens.*, 4:371-383

Sellers, P.J., M.D. Heiser and F.G. Hall. 1992. Relationship between surface conductance and spectral vegetation indices at intermediate (100 m^2 - 15 km^2) length scales. *J. Geophys. Res.* 97(D17): 19033-19059

Sellers, P.J., B.W. Meeson, F.G. Hall, G. Asrar, R.E. Murphy, R.A. Schiffer, F.P. Bretherton, R.E. Dickinson, R.G. Ellingson, C.B. Field, K.F. Huemmrich, C.O. Justice, J.M. Melack, N.T. Roulet, D.S. Schimel and P.D. Try. 1995. Remote sensing of the land surface for studies of global change: Models-algorithms-experiments. *Rem. Sens. Environ.* 51:3-26

Shuttleworth, W.J. and J. S. Wallace. 1985. Evaporation from sparse crops an energy combination theory. *Q.J.R.Met Soc.*, 111:839-855

Shuttleworth, W.J., R.J. Gurney, A.Y. Hsu and J.P. Ormsby., 1989. FIFE: The variation in energy partition at surface flux sites. *IAHS Publ.*, 186:67-74

Shuttleworth, W.J., Z.L. Yang and M.A. Arain. 1998. Aggregation rules for surface parameters in global models, *Hydrology and Earth System Sciences*, 2:217-226

Smith, P.M., S.N.V. Kalluri, S.D.Prince and R. DeFries. 1997. The NOAA/NASA Pathfinder AVHRR 8-km Land data set. *Photog. Eng. Remot.Sen*, 63(1):12-32

Stewart, J.B. and L.W. Gay. 1989. Preliminary modelling of transpiration from the FIFE site in Kansas. *Agric. and Forest Met.*, 48:305-315

Stewart, J.B., 1988. Modeling surface conductance of pine forest. *Agric. and Forest Met.*, 43:339-353

Stewart, J.B., W.P. Kustas, K.S. Humes, W.D. Nichols, M.S. Moran and H.A.R. de Bruin, 1994. Sensible heat flux-radiometric surface temperature relationship for 8 semi-arid areas, in *Proc. Workshop on thermal remote sensing of the energy and water balances*, La Londe les Maures, 20-23 Sept. France:27-30

Sugita, M. and W. Brutsaert. 1990. Regional surface fluxes from remotely sensed skin temperature and lower boundary layer measurements, *Water Resources Research*, 26:2,937-2,944

Sugita, M and W.Brutsaert., 1991. Daily evaporation over a region from lower boundary layer profiles measured with radiosondes. *Water Resour. Res.*, 27(5):747-752

Taconet, O., R. Benard and O. Vidal-Madjar. 1986. Evapotranspiration over an agriculture region using surface flux temperature model based on NOAA-AVHRR data. *J. of Climate and Appl. Met.* 25:284-307

Tan, C.S. and T.A. Black. 1976. Factors affecting the canopy resistance of a Douglas-fir forest. *Boundary-Layer Meteorol.* 10:475-488

Tanre, D., C. Deroo, P. Duhaut, M. Herman, J.J. Morcette, J. Perbos and P.Y. Deschamps. 1990. Description of a computer code to simulate the satellite signal in the solar spectrum: the 5S code, *Int. J. of Rem. Sens.*, 11:659-668

Taylor, C.M., R.J. Harding, A.J. Thorpe and P. Bessemoulin. 1997. A mesoscale simulation of land surface heterogeneity from HAPEX-Sahel, *J. of Hydr.*, 188-189:1040-1066

Troufleau, D., J.P. Lhomme, B. Monteny and A. Vidal. 1997. Sensible heat flux and radiometric surface temperature over sparse Sahelian vegetation. I, An experimental analysis of the kb^{-1} parameter, *J. of Hydr.*, 188-189:815-838

Tucker, C.J. 1979. Red and photographic infrared linear combination for monitoring vegetation, *Rem. Sens. of Env.*, 8:127-150

Valor, E. and V. Caselles. 1996. Mapping land surface emissivity from NDVI: application to European, African and South American areas, *Rem. Sens. of Env.*, 57:167-184

Verhoef, A., De Bruin, H.A.R. and Van Den Hurk, B.J.J.M. 1997. Some practical Notes on the Parameter kB^{-1} for sparse vegetation. *J. Appl. Meteor.* 36:560-572

Wang, J., Y. Ma, M. Menenti, W.G.M. Bastiaanssen and Y. Mitsuta. 1995. The scaling up of processes in the heterogeneous landscape of HEIFE with the aid of satellite remote sensing, *J. of Met. Soc. of Japan*, 73(6): 1,2235-1,244

Wang, J., W.G.M. Bastiaanssen, Y. Ma and H. Pelgrum. 1998. Aggregation of land surface parameters in the oasis-desert systems of Northwest China, *Hydr. Processes*, 12:2133-2147

Zhang, L. and R. Lemeur, 1995. Evaluation of daily evapotranspiration estimates from instantaneous measurements. *Agric. And Forest Met.*, 74:139-154

Zhong, Q. and Y.H. Li. 1988. Satellite observation of surface albedo over the Qinghai-Xizang plateau region, *Adv. in Atm., Sciences* 5:57-65

Appendix A

Appendix A.1: Specifications of the seven Landsat TM bands

Band	Wavelength interval (μm)
1	0.45 – 0.52
2	0.52 – 0.62
3	0.63 – 0.69
4	0.76 – 0.90
5	1.55 – 1.75
6	10.4 – 12.5
7	2.08 – 2.35
Geometrical resolution	30 m, band 6: 120m
Temporal resolution	16 days

Appendix A.2: Characteristics of the five NOAA-14 AVHRR bands

Band	Wavelength interval (μm)
1	0.58 – 0.68
2	0.72 – 1.10
3	3.55 – 3.93
4	10.5 – 11.5
5	11.5 – 12.5
Geometric resolution (at nadir)	1.1km
Temporal resolution	$\frac{1}{2}$ day

Appendix B: Color figures

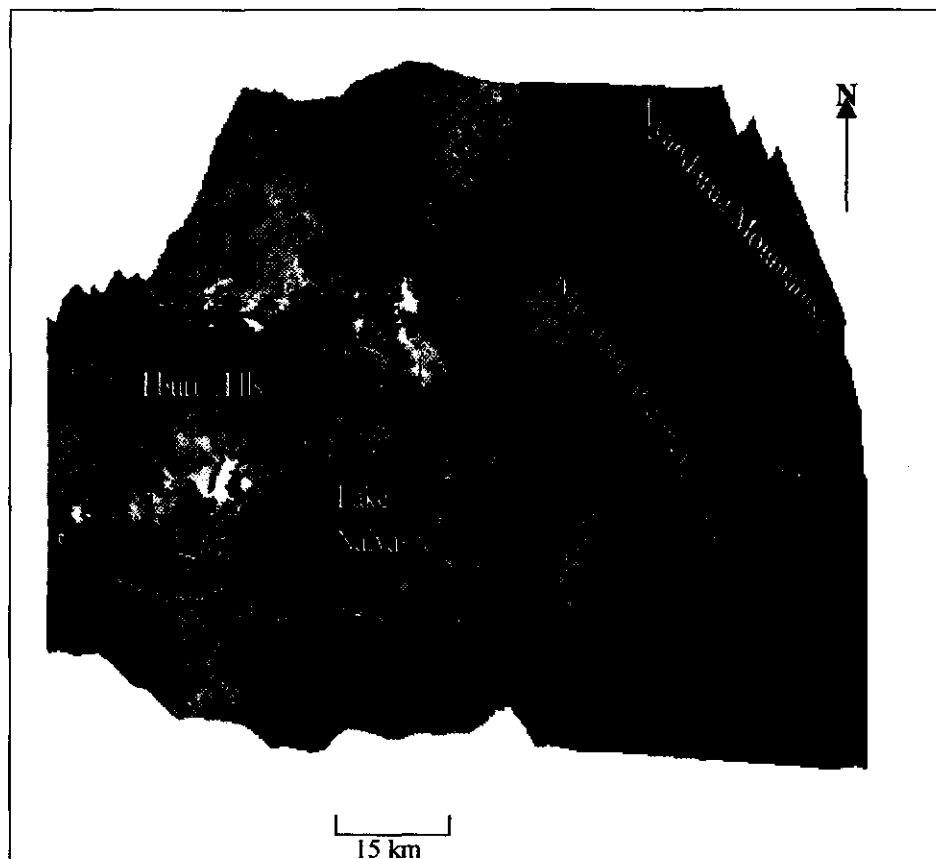


Fig. 3.3. Illustration of the topography and vegetation of the Naivasha catchment prepared from Landsat TM false color composite image overlaid on a digital elevation model of the area. The dark red areas are forests on mountains, light red tones indicate cropland and woodlands on the plateaus. The purple whitish tones represent grassland and bushland in the valley plains.

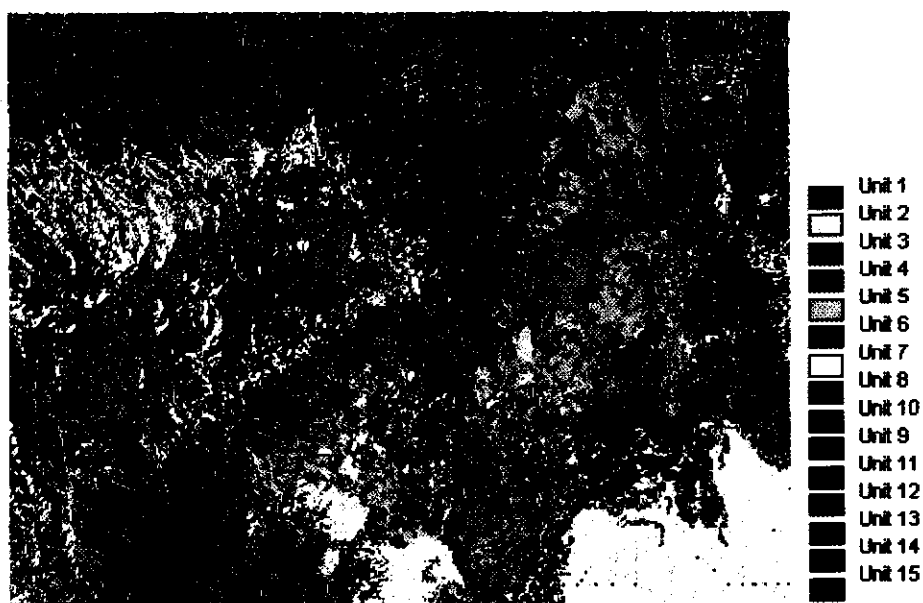


Fig.4.3: Hydrological delineation of a 19 km by 25 km area of Lake Naivasha watershed into 15 hydrological units



Fig. 4.5: Spatial patterns of actual evaporation of a 19 km by 25 km area of Lake Naivasha watershed on 21 January 1995

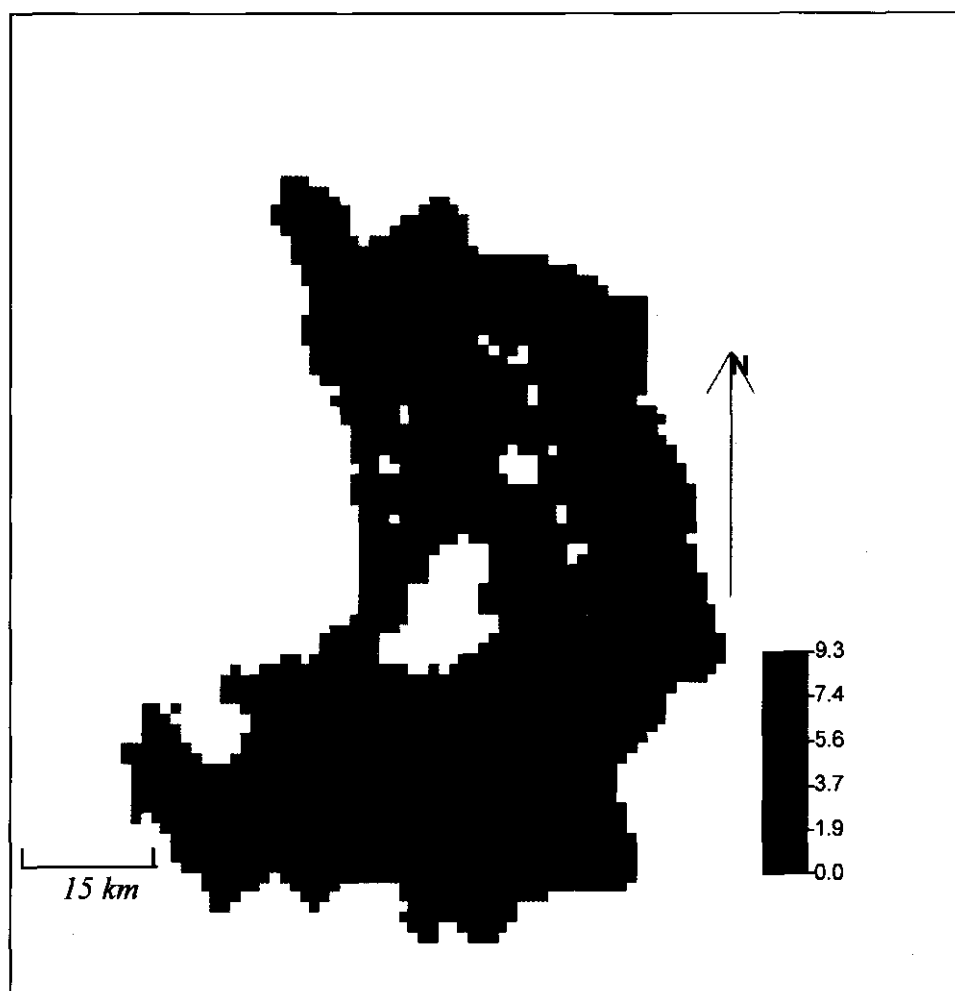


Fig.7.1 The spatial patterns of evaporation E (mm d^{-1}) in the Naivasha catchment on 27 January 1999. The white patches in the image are clouds

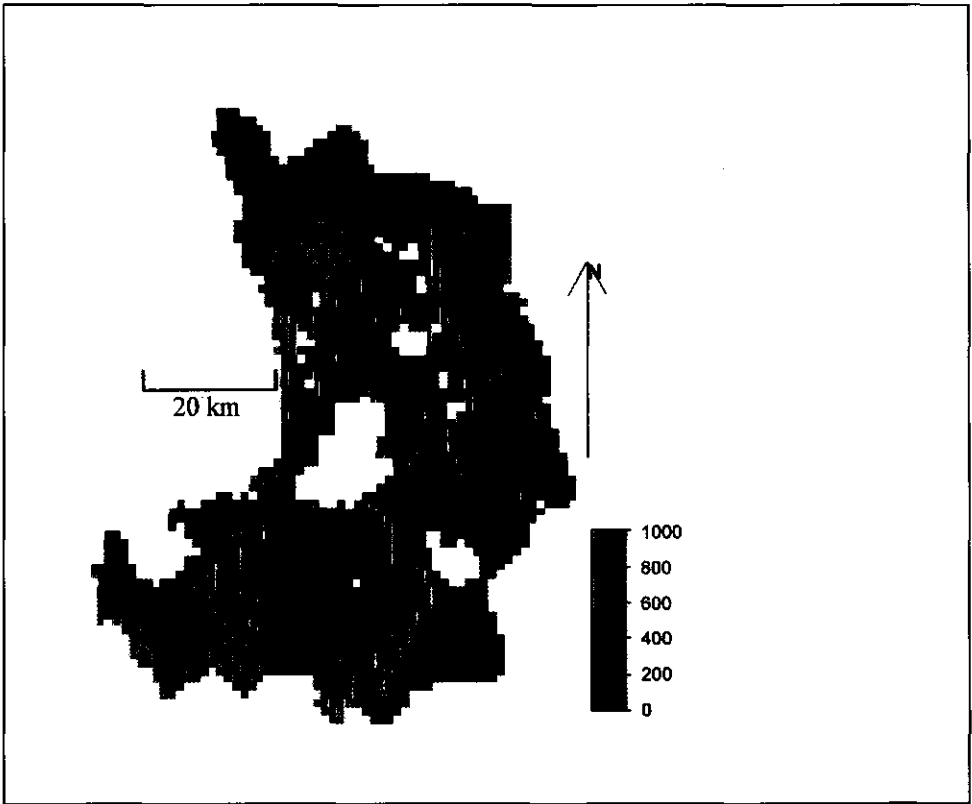


Fig. 7.3a. The spatial patterns of surface resistance r_s (s m^{-1}) in the Naivasha catchment on 27 January 1999

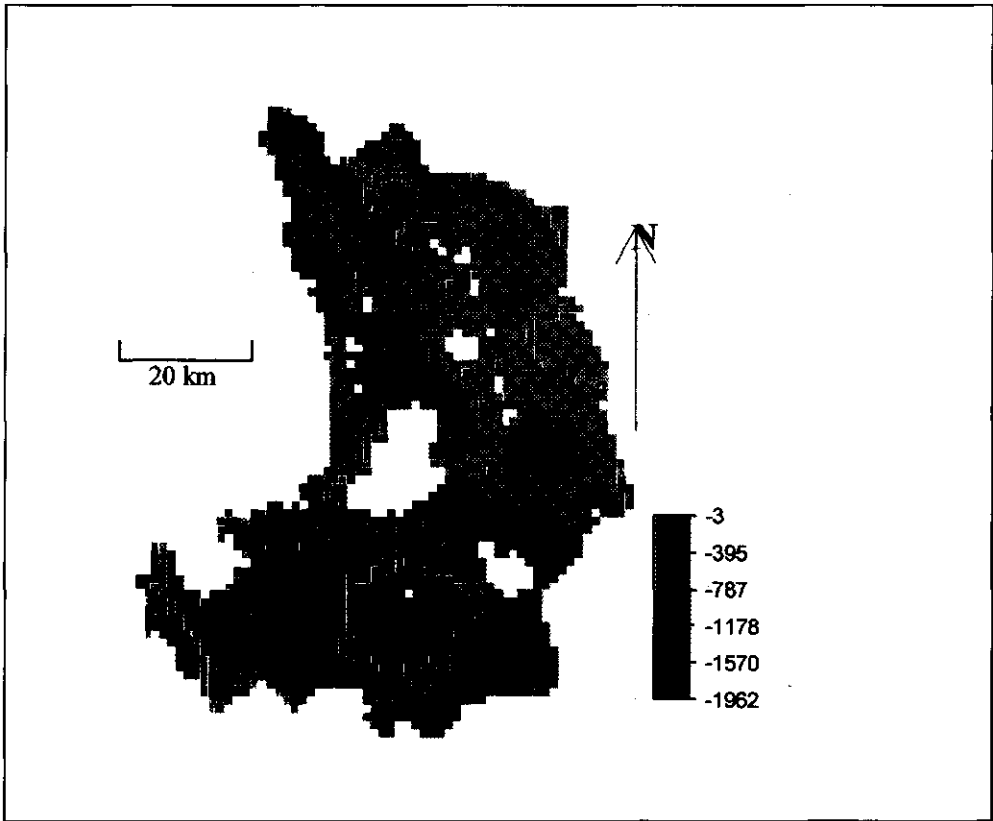


Fig. 7.3b. The spatial patterns of soil water potential head h_{rw} (cm) in the Naivasha catchment on 27 January 1999

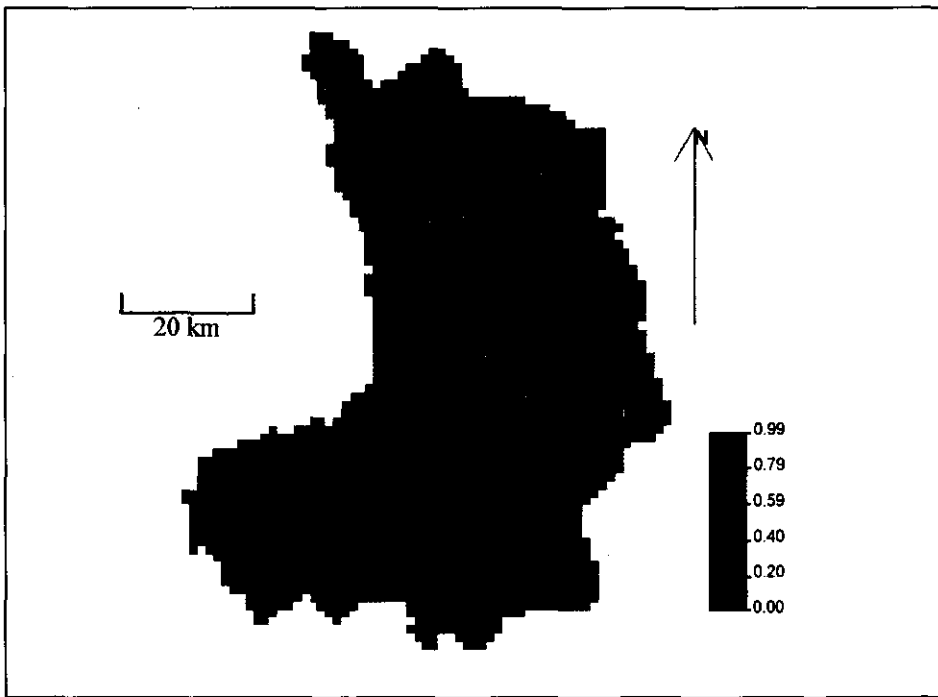


Fig. 7.5. The spatial patterns of the evaporative fraction A in the Naivasha catchment on 27 January 1999

Curriculum Vitae

Hussein Omar Farah was born on 7 July 1960 in Wajir Kenya. After Completing his secondary education at Alliance high school, he joined the University of Nairobi in 1981 and completed in 1985 with a Bachelor of Science degree (with honours) specializing in Land surveying. The same year he was employed in the Ministry of the Lands and Housing where he supervised Land surveys for Natural resources and urban mapping projects. In 1987, he went to the University of Waterloo in Canada to undertake a Masters degree in Geography and specialized in environmental remote sensing. He graduated in 1989 and continued with his position in the Ministry of lands and Housing. Since 1993 he has been a lecturer at the Department of Civil Engineering, Moi University in Kenya teaching engineering surveying and environmental remote sensing.

List of ITC Ph.D. dissertations

1. **Akinyede**, 1990, Highway cost modelling and route selection using a geotechnical information system
2. **Pan He Ping**, 1990, 90-9003757-8, Spatial structure theory in machine vision and applications to structural and textural analysis of remotely sensed images
3. **Bocco Verdinelli, G.**, 1990, Gully erosion analysis using remote sensing and geographic information systems: a case study in Central Mexico
4. **Sharif, M**, 1991, Composite sampling optimization for DTM in the context of GIS
5. **Drummond, J.**, 1991, Determining and processing quality parameters in geographic information systems
6. **Groten, S.**, 1991, Satellite monitoring of agro-ecosystems in the Sahel
7. **Sharifi, A.**, 1991, 90-6164-074-1, Development of an appropriate resource information system to support agricultural management at farm enterprise level
8. **Zee, D. van der**, 1991, 90-6164-075-X, Recreation studied from above: Air photo interpretation as input into land evaluation for recreation
9. **Mannaerts, C.**, 1991, 90-6164-085-7, Assessment of the transferability of laboratory rainfall-runoff and rainfall - soil loss relationships to field and catchment scales: a study in the Cape Verde Islands
10. **Ze Shen Wang**, 1991: 90-393-0333-9, An expert system for cartographic symbol design
11. **Zhou Yunxian**, 1991, 90-6164-081-4, Application of Radon transforms to the processing of airborne geophysical data
12. **Zuviria, M. de**, 1992, 90-6164-077-6, Mapping agro-topoclimates by integrating topographic, meteorological and land ecological data in a geographic information system: a case study of the Lom Sak area, North Central Thailand
13. **Westen, C. van**, 1993, 90-6164-078-4, Application of Geographic Information Systems to landslide hazard zonation
14. **Shi Wenzhong**, 1994, 90-6164-099-7, Modelling positional and thematic uncertainties in integration of remote sensing and geographic information systems
15. **Javelosa, R.**, 1994, 90-6164-086-5, Active Quaternary environments in the Philippine mobile belt
16. **Lo King-Chang**, 1994, 90-9006526-1, High Quality Automatic DEM, Digital Elevation Model Generation from Multiple Imagery
17. **Wokabi, S.**, 1994, 90-6164-102-0, Quantified land evaluation for maize yield gap analysis at three sites on the eastern slope of Mt. Kenya
18. **Rodriguez, O.**, 1995, Land Use conflicts and planning strategies in urban fringes: a case study of Western Caracas, Venezuela
19. **Meer, F. van der**, 1995, 90-5485-385-9, Imaging spectrometry & the Ronda peridotites
20. **Kufoniyi, O.**, 1995, 90-6164-105-5, Spatial coincidence: automated database updating and data consistency in vector GIS

21. **Zambezi, P.**, 1995, Geochemistry of the Nkombwa Hill carbonatite complex of Isoka District, north-east Zambia, with special emphasis on economic minerals
22. **Woldai, T.**, 1995, The application of remote sensing to the study of the geology and structure of the Carboniferous in the Calañas area, pyrite belt, SW Spain
23. **Verweij, P.**, 1995, 90-6164-109-8, Spatial and temporal modelling of vegetation patterns: burning and grazing in the Paramo of Los Nevados National Park, Colombia
24. **Pohl, C.**, 1996, 90-6164-121-7, Geometric Aspects of Multisensor Image Fusion for Topographic Map Updating in the Humid Tropics
25. **Jiang Bin**, 1996, 90-6266-128-9, Fuzzy overlay analysis and visualization in GIS
26. **Metternicht, G.**, 1996, 90-6164-118-7, Detecting and monitoring land degradation features and processes in the Cochabamba Valleys, Bolivia. A synergistic approach
27. **Hoanh Chu Thai**, 1996, 90-6164-120-9, Development of a Computerized Aid to Integrated Land Use Planning (CAILUP) at regional level in irrigated areas: a case study for the Quan Lo Phung Hiep region in the Mekong Delta, Vietnam
28. **Roshannejad, A.**, 1996, 90-9009284-6 The management of spatio-temporal data in a national geographic information system
29. **Terlien, M.**, 1996, 90-6164-115-2, Modelling Spatial and Temporal Variations in Rainfall-Triggered Landslides: the integration of hydrologic models, slope stability models and GIS for the hazard zonation of rainfall-triggered landslides with examples from Manizales, Colombia
30. **Mahavir, J.**, 1996, 90-6164-117-9, Modelling settlement patterns for metropolitan regions: inputs from remote sensing
31. **Al-Amir, S.**, 1996, 90-6164-116-0, Modern spatial planning practice as supported by the multi-applicable tools of remote sensing and GIS: the Syrian case
32. **Pilouk, M.**, 1996, 90-6164-122-5, Integrated modelling for 3D GIS
33. **Duan Zengshan**, 1996, 90-6164-123-3, Optimization modelling of a river-aquifer system with technical interventions: a case study for the Huangshui river and the coastal aquifer, Shandong, China
34. **Man, W.H. de**, 1996, 90-9009775-9, Surveys: informatie als norm: een verkenning van de institutionalisering van dorp - surveys in Thailand en op de Filipijnen
35. **Vekerdy, Z.**, 1996, 90-6164-119-5, GIS-based hydrological modelling of alluvial regions: using the example of the Kisaföld, Hungary
36. **Pereira, Luisa**, 1996, 90-407-1385-5, A Robust and Adaptive Matching Procedure for Automatic Modelling of Terrain Relief
37. **Fandino Lozano, M.**, 1996, 90-6164-129-2, A Framework of Ecological Evaluation oriented at the Establishment and Management of Protected Areas: a case study of the Santuario de Iguaque, Colombia
38. **Toxopeus, B.**, 1996, 90-6164-126-8, ISM : an Interactive Spatial and temporal Modelling system as a tool in ecosystem management : with two case studies : Cibodas biosphere reserve, West Java Indonesia : Amboseli biosphere reserve, Kajiado district, Central Southern Kenya

39. **Wang Yiman**, 1997, 90-6164-131-4, Satellite SAR imagery for topographic mapping of tidal flat areas in the Dutch Wadden Sea
40. **Asun Saldana-Lopez**, 1997, 90-6164-133-0, Complexity of soils and Soilscape patterns on the southern slopes of the Ayllon Range, central Spain: a GIS assisted modelling approach
41. **Ceccarelli, T.**, 1997, 90-6164-135-7, Towards a planning support system for communal areas in the Zambezi valley, Zimbabwe; a multi-criteria evaluation linking farm household analysis, land evaluation and geographic information systems
42. **Peng Wanning**, 1997, 90-6164-134-9, Automated generalization in GIS
43. **Lawas, C.**, 1997, 90-6164-137-3, The Resource Users' Knowledge, the neglected input in Land resource management: the case of the Kankanaey farmers in Benguet, Philippines
44. **Bijker, W.**, 1997, 90-6164-139-X, Radar for rain forest: A monitoring system for land cover Change in the Colombian Amazon
45. **Farshad, A.**, 1997, 90-6164-142-X, Analysis of integrated land and water management practices within different agricultural systems under semi-arid conditions of Iran and evaluation of their sustainability
46. **Orlic, B.**, 1997, 90-6164-140-3, Predicting subsurface conditions for geotechnical modelling
47. **Bishr, Y.**, 1997, 90-6164-141-1, Semantic Aspects of Interoperable GIS
48. **Zhang Xiangmin**, 1998, 90-6164-144-6, Coal fires in Northwest China: detection, monitoring and prediction using remote sensing data
49. **Gens, R.**, 1998, 90-6164-155-1, Quality assessment of SAR interferometric data
50. **Turkstra, J.**, 1998, 90-6164-147-0, Urban development and geographical information: spatial and temporal patterns of urban development and land values using integrated geo-data, Villaviciencia, Colombia
51. **Cassells, C.**, 1998, Thermal modelling of underground coal fires in northern China
52. **Naseri, M.**, 1998, Monitoring soil salinization, Iran
53. **Gorte B.G.H.**, 1998, 90-6164-157-8, Probabilistic Segmentation of Remotely Sensed Images
54. **Tenalem Ayenew**, 1998, 90-6164-158-6, The hydrological system of the lake district basin, central main Ethiopian rift
55. **Wang Donggen**, 1998, 90-6864-551-7, Conjoint approaches to developing activity-based models
56. **Bastidas de Calderon, M.**, 1998, Environmental fragility and vulnerability of Amazonian landscapes and ecosystems in the middle Orinoco river basin, Venezuela
57. **Moameni, A.**, 1999, Soil quality changes under long-term wheat cultivation in the Marvdasht plain, South-Central Iran
58. **Groenigen, J.W. van**, 1999, 90-6164-156-X, Constrained optimisation of spatial sampling: a geostatistical approach
59. **Cheng Tao**, 1999, 90-6164-164-0, A process-oriented data model for fuzzy spatial objects
60. **Wolski, Piotr**, 1999, 90-6164-165-9, Application of reservoir modelling to hydrotopes identified by remote sensing

61. **Acharya, B.**, 1999, 90-6164-168-3, Forest biodiversity assessment: A spatial analysis of tree species diversity in Nepal
62. **Akbar Abkar, Ali**, 1999, 90-6164-169-1, Likelihood-based segmentation and classification of remotely sensed images
63. **Yanuariadi, T.**, 1999, 90-5808-082-X, Sustainable Land Allocation: GIS-based decision support for industrial forest plantation development in Indonesia
64. **Abu Bakr, Mohamed**, 1999, 90-6164-170-5, An Integrated Agro-Economic and Agro-Ecological Framework for Land Use Planning and Policy Analysis
65. **Eleveld, M.**, 1999, 90-6461-166-7, Exploring coastal morphodynamics of Ameland (The Netherlands) with remote sensing monitoring techniques and dynamic modelling in GIS
66. **Yang Hong**, 1999, 90-6164-172-1, Imaging Spectrometry for Hydrocarbon Microseepage
67. **Mainam, Félix**, 1999, 90-6164-179-9, Modelling soil erodibility in the semiarid zone of Cameroon
68. **Bakr, Mahmoud**, 2000, 90-6164-176-4, A Stochastic Inverse-Management Approach to Groundwater Quality
69. **Zlatanova, Z.**, 2000, 90-6164-178-0, 3D GIS for Urban Development
70. **Ottichilo, Wilber K.**, 2000, 90-5808-197-4, Wildlife Dynamics: An Analysis of Change in the Masai Mara Ecosystem
71. **Kaymakci, Nuri**, 2000, 90-6164-181-0, Tectono-stratigraphical Evolution of the Cankiri Basin (Central Anatolia, Turkey)
72. **Gonzalez, Rhodora**, 2000, 90-5808-246-6, Platforms and Terraces: Bridging participation and GIS in joint-learning for watershed management with the Ifugaos of the Philippines
73. **Schetselaar, Ernst**, 2000, 90-6164-180-2, Integrated analyses of granite-gneiss terrain from field and multisource remotely sensed data. A case study from the Canadian Shield
74. **Mesgari, Saadi**, 2000, 90-3651-511-4, Topological Cell-Tuple Structure for Three-Dimensional Spatial Data
75. **Bie, Cees A.J.M. de**, 2000, 90-5808-253-9, Comparative Performance Analysis of Agro-Ecosystems
76. **Khaemba, Wilson M.**, 2000, 90-5808-280-6, Spatial Statistics for Natural Resource Management
77. **Shrestha, Dhruva**, 2000, Aspects of erosion and sedimentation in the Nepalese Himalaya: highland-lowland relations
78. **Asadi Haroni, Hooshang**, 2000, 90-6164-185-3, The Zarshuran Gold Deposit Model Applied in a Mineral Exploration GIS in Iran